Title of Thesis

IN SITU SPECTROSCOPIC STUDY OF WATER SPECIATION
IN THE DEPOLYMERIZED SILICATE MELTS

March 2015

Nadezda CHERTKOVA

Graduate School of

Natural Science and Technology

(Doctor's Course)

OKAYAMA UNIVERSITY

ABSTRACT

The mechanism of water and silicate melts interaction has been a subject of many petrological studies. Recent development of *in situ* spectroscopic techniques made possible direct measurement of water speciation in hydrous silicate melts at simultaneous high temperatures and high pressures. Though *in situ* spectroscopic measurements on water speciation were performed in the wide temperature and pressure ranges for the polymerized rhyolitic melts, there is a lack of such data for the depolymerized silicate melts. It has been shown by previous studies (e.g., Behrens and Yamashita, 2008) that equilibrium constant for the water speciation reaction can change one order of magnitude at the temperature near the glass transition for the melts of different composition. On the other hand, compositional dependence of the water speciation equilibrium has never been evaluated at magmatic conditions. This study is the first attainment of *in situ* determination of the water speciation in the depolymerized sodium silicate melts at pressure to 1.7 GPa and temperature to 900 °C.

In situ measurements on hydrous silicate melts using hydrothermal diamond anvil cell (HDAC) technique require a thoroughly developed procedure for the determination of pressure during experiments. In the first part of my dissertation I describe the synthesis of ^{13}C diamond pressure sensor. Polycrystalline, cubic ^{13}C diamond was successfully synthesized from amorphous carbon in the Kawai-type multianvil apparatus at 21 GPa and at temperature exceeding 2350 °C. The polycrystalline diamond was homogeneous with small grain size (10-20 µm) and had a sharp Raman peak, and thereby was suitable as a pressure sensor for the experiments in HDAC. I

further examined the precision of pressure determination for this pressure sensor at simultaneous high temperatures and high pressures by cross calibration with the phase transitions of H_2O pressure medium, the pressure- and temperature-dependent fluorescence line of ruby and the Raman shift of α-quartz. Experimental results in the range of pressures to 4.2 GPa and temperatures to 500 °C showed that independent pressure and temperature calibrations of the ^{13}C diamond Raman shift can be used for the determination of pressure with an accuracy better than ± 0.3 GPa inside the sample chamber of HDAC.

The second part of my dissertation is focused on the *in situ* spectroscopic measurements of water speciation in the depolymerized sodium disilicate melts. Sodium disilicate composition was chosen as a structural analog of basaltic melt in terms of the number of non-bridging oxygens per silica tetrahedron (NBO/T ≈ 1.0, anhydrous basis). Water speciation equilibrium in the sodium disilicate melts containing 1.3-8.1 wt.% water was examined at 0.2-1.7 GPa and 800-900 °C in HDAC employing the synthesized ^{13}C diamond pressure sensor. The pressure- and temperature-dependence of water speciation equilibrium was determined *in situ* by monitoring the intensity change of near-infrared absorption bands of structurally bound OH groups and H_2O molecules. The hydrous sodium disilicate melt served both as a sample and as a pressure medium in the experiments, which allowed to keep the total water content of the melt constant and to perform full quantitative evaluation of the changes in the near-infrared absorption band intensities by an iterative approach. The near-infrared absorption spectroscopy showed that water speciation equilibrium in the hydrous sodium disilicate melts is independent of pressure. Simultaneous Raman scattering spectroscopy has

shown a negligible pressure effect on the concentrations of Q^2 and Q^3 species in these melts, consistent with the near-infrared absorption spectroscopy. Pressure-independence of water speciation equilibrium reveals a negligible standard volume change for the reaction between molecular H_2O, oxygens of silicate melt framework and structurally bound OH groups. The temperature dependence of equilibrium constant for this reaction can be expressed by $\ln K_1$ = 4.02 – 3698 / T (K). Thus, compositional dependence of water speciation equilibrium at 800-900 °C was found to be much weaker than that expected from the previously reported data for low-temperature range (200-320 °C).

TABLE OF CONTENTS

CHAPTER 1

INTRODUCTION

1.1. General overview

Silicate melts play an important role in the material and heat transfer within the Earth's interior. Low partitioning coefficients of volatile components between the common upper mantle minerals (olivine, orthopyroxene, clinopyroxene, garnet) and silicate melts ($D_{H_2O}^{mineral/melt}$<0.04, $D_{CO_2}^{mineral/melt}$<0.01, $D_{Cl}^{mineral/melt}$<0.01; Hauri et al., 2006) make silicate melts an excellent reservoir for the volatiles storage and transport along the tectonic plate boundaries and in the hot spot regions.

Compositional analysis of high-temperature volcanic gases has shown that water is the first major volatile component discharging from active volcanoes in the various geological settings including convergent-plate margins, divergent-plate margins and hot spots (Table 1-1).

Volcano	Magma	T (°C)	H_2O	H_2	CO_2	CO	SO_2	H_2S	HCl
Etna, Italy (Gerlach, 1979)	hawaiite	1075	49.14	0.53	23.41	0.49	25.94	0.21	-
Klyuchevskoy, Kamchatka (Taran et al., 1991)	calc-alkaline basalt	1075	94.79	1.15	2.30	-	0.1	-	1.72
Gunung Merapi, Indonesia (LeGuern et al., 1982)	andesite	733	92.5	1.07	5.0	0.08	0.64	0.59	0.04
Usu, Japan (Giggenbach, 1986)	dacite-andesite	690	99.3	0.26	3.85	-	0.23	0.26	0.35
St. Helens, USA (Gerlach et al., 1986)	dacite	725	96.2	0.5	2.91	0.02	0.12	0.2	0.08
Erta' Ale, Ethiopia (Giggenbach, 1976)	tholeiitic basalt	1130	79.4	1.49	10.4	0.46	6.5	-	0.42
Surtsey, Iceland (Gerlach, 1980)	alkali basalt	1125	92.0	1.65	1.94	0.07	3.27	0.12	-
Kilauea, Hawaii (Gerlach, 1993)	tholeiitic basalt	1135	52.30	0.79	30.87	1.00	14.59	0.16	0.14

Table 1-1. Concentrations (in mole %, average values) and temperatures of low-pressure (1 atm) volcanic gases from the subduction zone-related, rift zone-related and ocean island-related volcanoes.

The concentration of water measured in the volcanic groundmass glasses and melt inclusions in phenocrysts rarely exceeds 7 wt.% (Table 1-2). Nevertheless, incorporation of even small amount of water can significantly change physical properties of melts.

	Mid-oceanic ridge basalts	Hawaiian basalts	Mariana arc andesites and basalts	Long Valley Caldera and vicinity, rhyolites
Groundmass glasses	0.1-0.5 [1]	0.1-1.0 [3]	0.3-2.1 [5]	0.1-2.6 [7]
Melt inclusions	0.1-0.6 [2]	<0.1-0.8 [4]	1.4-6.0 [6]	4.4-6.1 [8]
[1] Dixon et al. (1988); [2] Sobolev and Chaussidon (1996); [3] Dixon et al. (1991, 2001); [4] Hauri (2002); [5] Garcia et al. (1979), Newman et al. (2000); [6] Newman et al. (2000), Kelley et al. (2010); [7] Newman et al. (1986); [8] Wallace et al. (1995)				

Table 1-2. Variations of water content in the groundmass glasses and melt inclusions from the different geological settings.

Addition of water has a profound effect on such properties as melt viscosity, density, liquidus temperature and electrical conductivity. With the addition of 5 wt.% water viscosity of rhyolitic melt at 1200 °C and 200 MPa drops from $1.6 \cdot 10^7$ to $4 \cdot 10^2$ Pa s (Persikov, 1991), a decrease of ~10% is expected for its density (Ochs and Lange, 1997; 1999) and its liquidus temperature gains >250 °C depression (Holtz et al., 2001). Electrical conductivity of basaltic melt increases six times upon the dissolution of 4-6 wt.% water at 1500 °C and 2 GPa (Ni et al., 2011).

The mechanism of water and melt interaction was a subject of interest for the number of petrological studies since the latter half of last century and several models that relate the change in physical properties to the change in silicate melt structure have been proposed. Burnham's model (1975) was formulated using experimentally determined effects of water on the volumetric and thermodynamic characteristics of hydrous albite melt. This model described primarily the reaction of water with the bridging oxygens of (Al, Si)O_4 tetrahedra to produce OH groups. It further discussed the exchange reaction of a proton from H_2O with a non-tetrahedrally coordinated cation (Al^{3+}) to balance the net charge on the AlO_4 group.

Later infrared spectroscopic studies have detected the presence of molecular H_2O as a dissolved species in hydrous silicate glasses (e.g., Ernsberger, 1977; Bartholomew et al., 1980; Wu, 1980; Stolper, 1982a). On the basis of this observation Stolper and his coworkers (e.g., Stolper, 1982b; Silver and Stolper, 1985) proposed the model that involves a homogeneous reaction between the molecular water (H_2O_m), the bridging oxygen of silicate network structure (O) and the structurally bound hydroxyl groups (OH) (water speciation reaction):

$$H_2O_m \text{ (melt)} + O \text{ (melt)} = 2OH \text{ (melt)}, \tag{1-1}$$
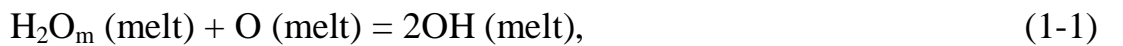
as well as a heterogeneous reaction between the melt and the vapor phases:

$$H_2O \text{ (vapor)} = H_2O_m \text{ (melt)}. \tag{1-2}$$

When ideal mixing between the water species and the bridging oxygens in the melt is assumed, equilibrium constant for the water speciation reaction (1-1) is directly related to the concentrations of these species:

$$K_1 = \frac{(X_{OH})^2}{(X_{H_2Om})(X_O)}, \qquad\qquad (1\text{-}3)$$

where X indicates mole fraction of the species in the melt on a single-oxygen basis (Stolper, 1982b).

Equilibrium constant for the vapor-melt reaction (1-2) can be written as

$$K_2 = \frac{X_{H_2Om}}{f_{H_2O}/f^o_{H_2O}}, \qquad\qquad (1\text{-}4)$$

where f_{H_2O} is the fugacity of water in the vapor and $f^o_{H_2O}$ is the fugacity of water at standard state.

At low water concentrations OH groups formed by the reaction (1-1) are the dominant water species, though H_2O molecules can also be detected. When the total water content exceeds a few weight percent, the concentration of H_2O molecules increases and becomes higher than the concentration of OH groups (Figure 1-1).
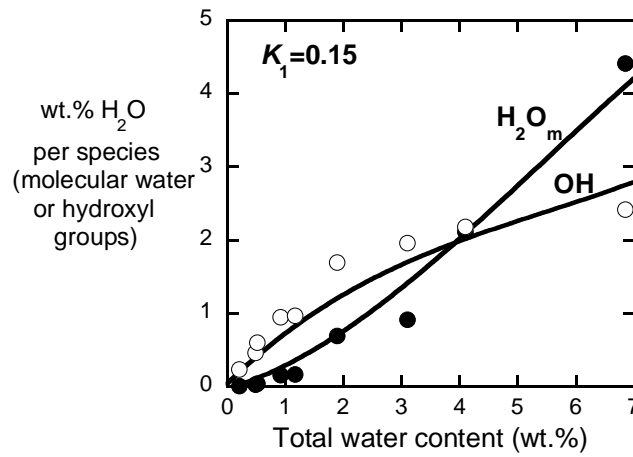

Figure 1-1. Concentrations of water present as molecular H_2O species (filled symbols) and OH groups (open symbols) versus total water content of volcanic rhyolitic and synthetic albite glasses, measured by infrared spectroscopy at room temperature (data points are from Stolper, 1982b). The data points can be fitted using the value of $K_1=0.15$ (solid line).

This model was originally proposed for the felsic silicate melts such as albite, silica and rhyolites, which can be visualized as nearly fully polymerized tetrahedral frameworks with energetically indistinguishable bridging oxygens. Upon interaction of such melts with water, for every two OH groups produced by the reaction (1-1), one bridging oxygen is consumed and the melt becomes less polymerized. Consequently, the viscosity of the melt is expected to decrease with the formation of OH groups (Figure 1-2). On the other hand, incorporation of H_2O molecules does not require any destruction of the silica tetrahedral framework, and decrease in viscosity becomes less and less profound at higher total water contents.

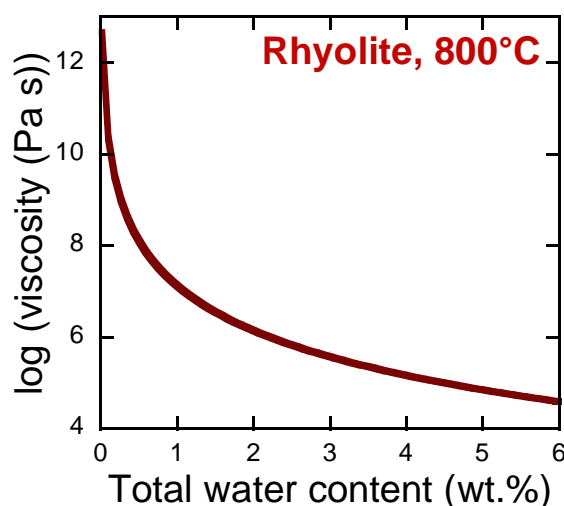**Figure 1-2.** Viscosity of hydrous rhyolitic melt as a function of total water content, calculated at 800 °C using the model of Hess and Dingwell (1996).

The model proposed by Stolper was based on the examination of the quenched glasses. Afterwards, a study of structural relaxation phenomenon by Dingwell and Webb (1990) showed that water speciation in the glass quenched from high temperature is frozen in at the glass transition

temperature, which is a function of the melt viscosity and the quenching rate. Since viscosity of the melt has a strongly negative dependence on total water content (Figure 1-2), glass transition temperature is a total water content-dependent parameter and water speciation in the quenched hydrous glasses does not necessarily represent high-temperature equilibrium.

1.2. Previous *in situ* studies on water speciation

Recent development of *in situ* techniques made possible direct spectroscopic measurement of water speciation in silicate melts at high temperature. *In situ* studies by Nowak and Behrens (1995), Shen and Keppler (1995), Sowerby and Keppler (1999) have shown that OH groups and molecular H_2O are both stable water species in the polymerized rhyolitic melts, and the water speciation equilibrium (1-1) in the melt has a strong temperature dependence. Nowak and Behrens (1995), Shen and Keppler (1995) observed one order of magnitude increase of equilibrium constant of the water speciation reaction (K_1) from the glass state at room temperature to the melt state at 800-850 °C for the simple analogs of granite.

Behrens and Yamashita (2008) raised the question about the compositional dependence of water speciation equilibrium. They performed near-infrared measurements for more depolymerized compositions $Na_2Si_4O_9$ and $Na_2Si_6O_{13}$ (number of non-bridging oxygens per silica tetrahedron, NBO/T, is 0.50 and 0.33 respectively) and found ~3 ln units higher value of K_1 for the $Na_2Si_4O_9$ than those reported for the polymerized aluminosilicate melts (NBO/T ≈ 0) at a given temperature (Figure 1-3). This difference of equilibrium constants was found at the temperature near the glass transition,

but the value of K_1 has never been evaluated for the depolymerized melts at magmatic conditions.
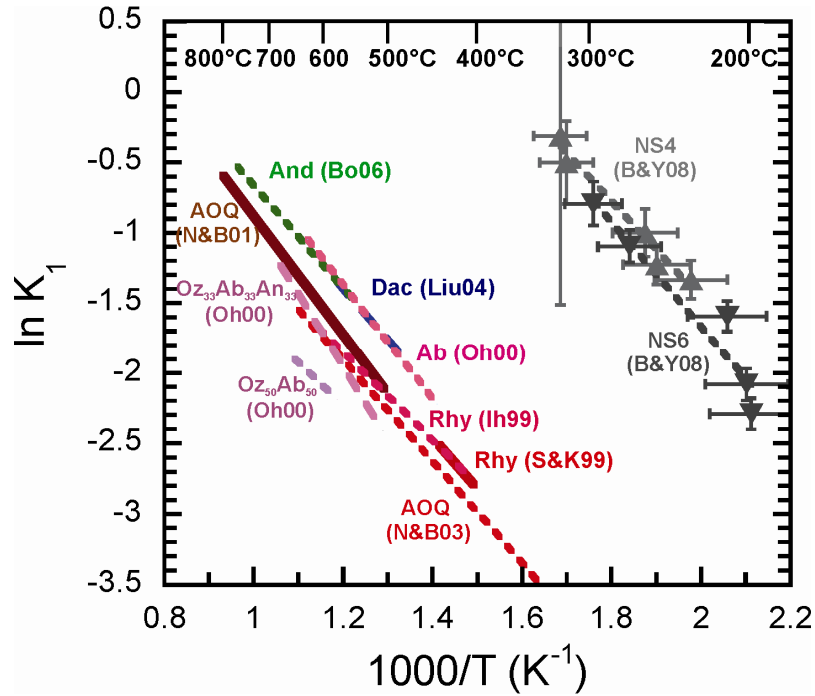

Figure 1-3. Temperature dependence of equilibrium constants for the water speciation reaction (1-1) in melts and glasses (modified after Behrens and Yamashita, 2008). Data sources: $Na_{0.39}K_{0.31}Al_{0.69}Si_{3.31}O_8$ (AOQ) (Nowak and Behrens, 2001; Behrens and Nowak, 2003); andesite (And) (Botcharnikov et al., 2006); $Na_{0.5}Ca_{0.25}AlSi_3O_8$ ($Qz_{33}Ab_{33}An_{33}$), $Ca_{0.5}AlSi_3O_8$ ($Qz_{50}An_{50}$), $NaAlSi_3O_8$ (Ab) (Ohlhorst, 2000); dacite (Dac) (Liu et al., 2004); rhyolite (Rhy) (Ihinger et al., 1999; Sowerby and Keppler, 1999); $Na_2Si_4O_9$ (NS4), $Na_2Si_6O_{13}$ (NS6) (Behrens and Yamashita, 2008).

Quantitative evaluation of the pressure effect on water speciation equilibrium was done for the haplogranitic melt to 250 MPa by Nowak and Behrens (2001) and no pressure dependence of equilibrium constant K_1 was observed. Sowerby and Keppler (1999) found only slight variation (less than 1 ln unit) of the K_1 values in the rhyolitic melt from ambient pressure to 1

GPa at a given temperature, and concluded a negligible pressure effect on water speciation equilibrium. Ideal mixing between molecular water species, bridging oxygens and OH groups seems to be a good approximation for the polymerized aluminosilicate melts, because water speciation equilibrium was shown to be independent of total water content at these conditions. Nevertheless, *in situ* analysis of pressure dependence of K_1 has never been done for the depolymerized silicate melts. The presence of non-bridging oxygens in the depolymerized silicate melts may cause a deviation from the ideal mixing behavior of water species at high pressure and high temperature.

1.3. Challenging hydrothermal diamond anvil cell (HDAC) experiment: advantages and limitations

High-temperature and high-pressure spectroscopic studies on silicate melts can be performed using externally heated hydrothermal diamond anvil cell (HDAC) (Bassett et al., 1993). HDAC consists of two platens with diamond anvils mounted at their centers (Figure 1-4). The two platens are drawn close to each other along guide posts by driving screws, thus applying pressure to a sample held inside a soft metal gasket between the diamond anvils. Each diamond anvil is accommodated in a resistance heater, enabling the sample to be heated to near 1000 °C. Holes through the centers of the platens allow visual observation as well as optical spectroscopic measurements of the sample at experimental conditions. Once a melt phase is observed in the sample chamber, it can be probed by near-infrared and Raman

spectroscopy, and structural information of the melt will be collected *in situ* at high temperature and high pressure.
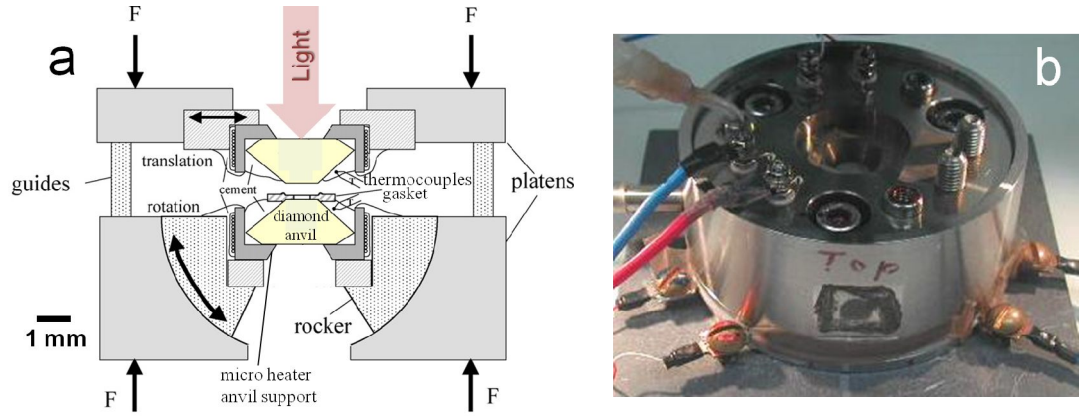
Figure 1-4. Major components and setup of hydrothermal diamond anvil cell (HDAC): (a) general schematic (modified after Smith and Fang, 2009); (b) actual photograph.

One of the main difficulties arising from this design of HDAC is the evaluation of pressure generated inside the sample chamber. Upon heating, sample material starts to expand and metal gasket deforms, which is accompanied by sample volume change. Pressure inside the sample chamber (P) is a function of experimental temperature (T) and volume of the sample (V):

$$P = f(T, V).$$

A relationship between pressure, temperature and volume of the sample (equation of state) is unique for any chosen sample material. Therefore, external force applied along the compression axis of HDAC can not be directly related to the pressure inside the sample chamber and determination of pressure during HDAC experiments is not a simple task.

Most of the experiments involving silicate melts and fluids are performed in HDAC with water as a pressure medium and pressure-temperature-density relationships of pure water are used for the determination of pressure (e.g., Bassett, 2003). However, at relatively high pressures significant deformation of the gasket results in a deviation from the isochoric *P-T* path during experiment and limits the applicability of this method.

During the last several decades a number of spectroscopic standards were considered for pressure determination inside the sample chamber of diamond anvil cell. Ruby, Sm:YAG and SrB_4O_7:Sm^{2+} fluorescent compounds, as well as diamond, quartz and cubic boron nitride Raman sensors were calibrated in the wide pressure and temperature ranges (e.g., Zha *et al*., 2000; Ragan *et al*., 1992; Hess and Exarhos, 1989; Lacam and Chateau, 1989; Schiferl *et al*., 1997; Schmidt and Ziemann, 2000; Datchi and Canny, 2004). Majority of these standards react with silicate melts and incorporate into silicate network structure at high temperatures.

Diamond is one of the most attractive pressure sensors for HDAC experiments because it is chemically inert and does not react either with silicate samples or supercritical aqueous fluids over a large range of experimental conditions (e.g., Mysen and Yamashita, 2010). Below 13 GPa the ^{13}C Raman peak is well separated from that of the ^{12}C diamond anvils and can be used for the monitoring of pressure in the immediate vicinity of the sample.

Despite the advantages of ^{13}C diamond sensor for pressure determination, small ^{13}C diamonds suitable for the experiments in HDAC are not commercially available. Synthesis and calibration of this pressure sensor

is required in order to perform precise spectroscopic measurements on silicate melts at high pressures using HDAC technique.

In situ spectroscopy with HDAC has a limitation of maximum achievable temperature at about 1000 °C. Above this temperature the backside of diamond anvils which is exposed to ambient pressure transforms to graphite and blocks visual access to the sample. For this reason it is difficult to study natural depolymerized silicate melts such as basalts using HDAC technique. This limitation forces to use the analogs of natural depolymerized melts with the lower melting temperature. $Na_2Si_2O_5$ is an analog of basaltic melt in terms of the number of non-bridging oxygens per silica tetrahedron in network structure (NBO/T ≈ 1). The melting temperature of this composition is 874 °C at 0.1 MPa (Levin et al., 1964), which goes down with the addition of water. Hydrous $Na_2Si_2O_5$ glasses have been extensively studied at room temperature by nuclear magnetic resonance (NMR) (e.g., Xue and Kanzaki, 2004; Cody et al., 2005), Raman (Mysen and Cody, 2005) and infrared (Yamashita et al., 2008) techniques. Quantitative information about the change in silicate network structure upon the incorporation of water species, as well as room temperature spectroscopic parameters for the infrared analysis are available for this composition. Though this simple composition does not have direct geological relevance, in situ spectroscopy of $Na_2Si_2O_5$–H_2O system can shed a new light on the understanding of water dissolution mechanism in the depolymerized silicate melts.

1.4. Tasks and outline of this work

The primary task of this work was to determine the effects of pressure and temperature on water speciation equilibrium in the depolymerized silicate melts. These data are necessary for the thermodynamic modeling of the mechanism of water dissolution and calculation of water species abundances in the melts of different composition.

In order to fulfill this task, a method for the precise pressure determination inside the sample chamber of HDAC is required. In Chapter 2 of this dissertation I describe the synthesis of ^{13}C diamond pressure sensor which has the necessary characteristics for the monitoring of pressure in HDAC experiments involving silicate melts. The precision of the synthesized pressure sensor was checked at simultaneous high temperature and high pressure using several independent pressure standards. Experimental results of this Chapter have been published in the paper "High-pressure synthesis and application of ^{13}C diamond pressure sensor for the experiments in a hydrothermal diamond anvil cell" in Mineralogical Magazine journal (the Mineralogical Society of Great Britain and Ireland) (Chertkova et al., 2014).

Chapters 3 describes spectroscopic measurements of hydrous $Na_2Si_2O_5$ melts at high temperature in the wide range of pressures using HDAC. In these measurements water speciation was probed by near-infrared spectroscopy and additional information about Q speciation of silica network structure was obtained by Raman spectroscopy. This chapter gives the details of absorption coefficients calibration and quantitative evaluation of water speciation at experimental conditions. It further examines the pressure- and temperature-dependence of water speciation equilibrium in the melts of

different composition and gives a comparison between the results of this study and previous measurements on fully polymerized silicate melts.

CHAPTER 2

PROCEDURE FOR PRESSURE DETERMINATION INSIDE THE SAMPLE CHAMBER OF HDAC

Despite of numerous advantages, ^{13}C diamonds suitable for diamond anvil cell experiments are not readily available. Shiferl et al. (1997) proposed to use chemical vapor deposition for the synthesis of thin polycrystalline ^{13}C diamond films. Qui et al. (2004) made a deposition of the thin epitaxial ^{13}C layer directly on the ^{12}C diamond anvil. These methods require specific laboratory equipment and precautions about the isotopic purity of the synthesis product.

On the other hand, the synthesis of ^{13}C-enriched diamond pressure sensor can be performed by high-pressure techniques. In this case the product volume should be large enough for the preparation of diamond chips and the grain size should be small enough to fit into the sample chamber of HDAC.

The ^{13}C diamond pressure scale was developed in 1996-1997 (Bassett et al., 1996; Schiferl et al., 1997) by measuring the pressure- and temperature-dependent Raman shift of the ^{13}C diamond film. Schiferl et al. (1997) evaluated dependence of ^{13}C diamond Raman shift on pressure and temperature based on the assumption that there is no cross derivative between the pressure term and the temperature term.

Datchi et al. (2007) examined the ^{13}C diamond Raman shift to 13 GPa at 25 °C, 211 °C and 300 °C, and showed that there is no need to introduce the pressure and temperature cross derivative at these conditions. Mysen and Yamashita (2010) studied the ^{13}C diamond Raman shift at simultaneous high pressures and high temperatures to 1.27 GPa and 800 °C, and did not observe any evidence for the pressure and temperature cross derivative. In the present work I test the precision of independent pressure and temperature calibrations to 500 °C and 4.2 GPa using various pressure references. Changes in pressure and temperature result in very small frequency shifts in Raman spectra of

diamond and special precautions should be taken for the precise determination of position of its Raman peak.

In the first section of this chapter I describe the detailed procedure of high-pressure synthesis of polycrystalline ^{13}C diamond in a multianvil apparatus. In the second section I evaluate the accuracy of the synthesized pressure sensor and check its calibrations for possible cross derivative between the pressure- and temperature terms at simultaneous high pressures and high temperatures using HDAC.

2.1. Synthesis of ^{13}C diamond pressure sensor

2.1.1. Synthesis in a multianvil apparatus

Synthesis of ^{13}C diamond was carried out by direct conversion from fine amorphous ^{13}C powder in the Kawai-type multianvil apparatus (USSA-5000) installed at the Institute for Study of the Earth's Interior, Okayama University (Figure 2-1).
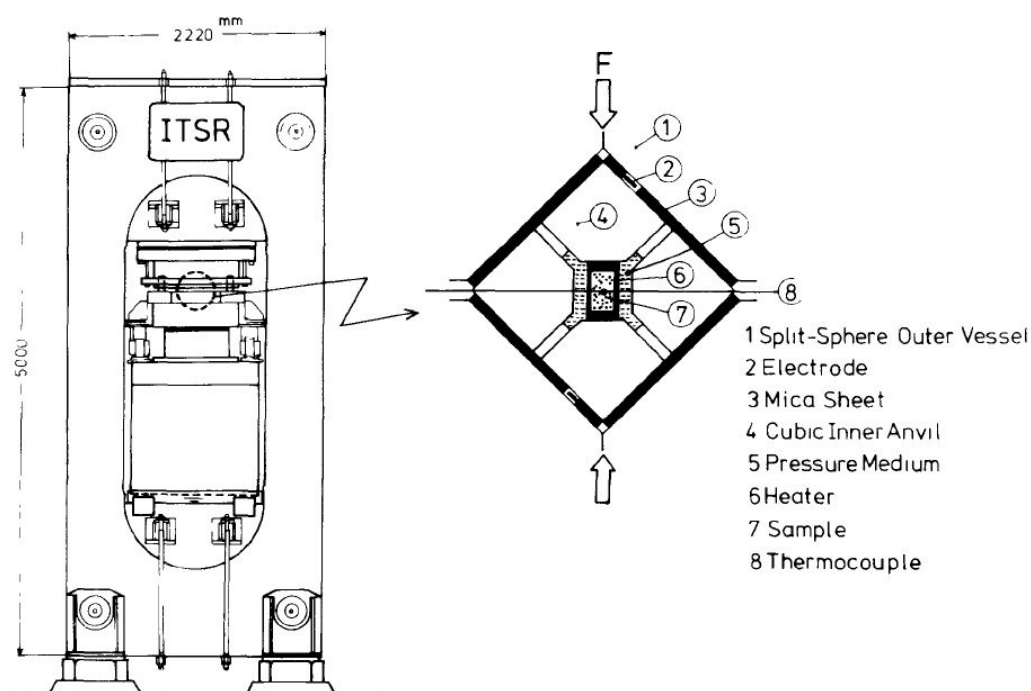
Figure 2-1. A whole plan of the Kawai-type high-pressure apparatus (left) and a schematic cross-section of the split-sphere pressure vessel with the furnace assembly (right) (reprinted after Ito et al., 1984, with the permission from Elsevier).

Starting material was amorphous ^{13}C (99 atom% pure; Cambridge Isotope Laboratories, Inc.), which was loaded directly into a MgO capsule placed in an octahedral pressure medium of 5%Cr_2O_3+MgO (10 mm edge length) together with a cylindrical $LaCrO_3$ heater and a ZrO_2 thermal insulator (Figure 2-2). The cell assembly was compressed by eight tungsten carbide cubic anvils with an edge length of 32 mm and a truncated corner of 4 mm. Experiments were performed employing two types of cell configuration. In the first configuration, the two sample chambers filled with ^{13}C powder were set in MgO capsule at the positions slightly shifted from the center toward the top and the bottom, and a $W_{97}Re_3$–$W_{75}Re_{25}$ thermocouple junction was set at the center (Figure 2-2a). In the second configuration, a one sample chamber

was at the center of MgO capsule and the thermocouple junction was set 0.4 mm below (Figure 2-2b).
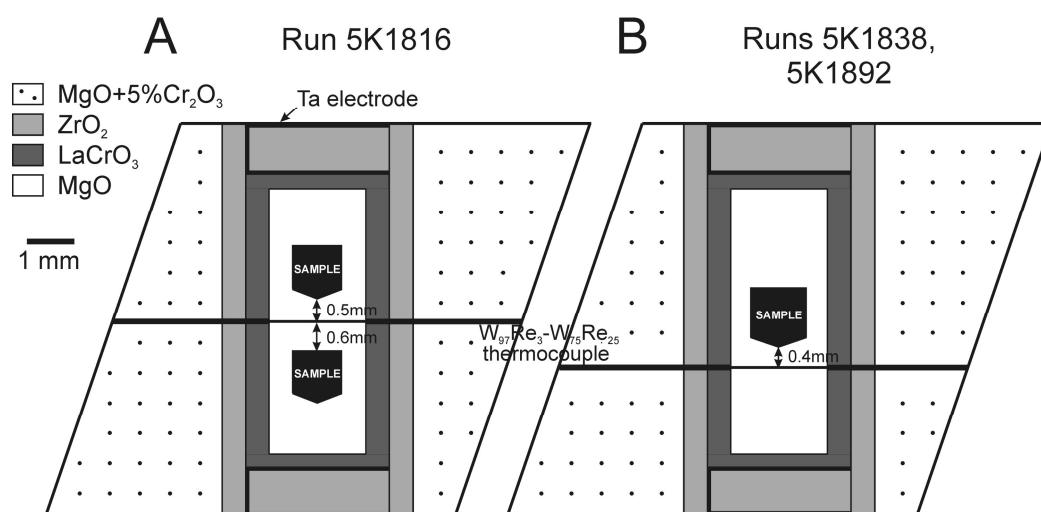

Figure 2-2. Schematic cross sections of the two types of cell assembly used for the synthesis of ^{13}C diamond in the multianvil apparatus. (**a**) MgO capsule contains two chambers filled with ^{13}C powder and a thermocouple junction between these chambers (run 5K1816). (**b**) MgO capsule with one sample chamber at the center and the thermocouple shifted towards the bottom (runs 5K1838, 5K1892). Each cell assembly was compressed by eight tungsten carbide cubic anvils with 4 mm truncation edge. Mineralogical Magazine is acknowledged for the permission to reproduce the figure published in Chertkova et al. (2014).

High synthesis conditions were chosen in order to insure a rapid and complete conversion of amorphous ^{13}C into cubic diamond according to the phase diagram proposed by Irifune et al. (2004). Three experiments (5K1816, 5K1838 and 5K1892) were carried out following the method of Ito and Yamada (1982). Pressure was first increased slowly to 21 GPa, then the sample assembly was heated to 2300 °C within about 90 min, kept for 3–4 min, and quenched by cutting off the electric power supply. After quenching

the pressure was released slowly over about 15 h, and the run product was recovered.

2.1.2. Analysis of the run products

Recovered samples were first examined by micro-focus X-ray diffraction using a Rigaku Rint Rapid II with a 100 μm beam from a rotating copper anode operated at 40 kV and 30 mA.

X-ray diffraction of the product of run 5K1816 with the first configuration revealed that the product was mostly composed of ^{13}C amorphous with small amounts of hexagonal and cubic diamonds. A possible reason for the presence of untransformed material (amorphous carbon) and metastable phase (hexagonal diamond) is a steep temperature gradient from the point of thermocouple junction (the central hot spot) to the end of the heater. According to Irifune et al. (2004), coexistence of cubic and hexagonal diamonds corresponds to the temperatures lower than 2200 °C at 21 GPa, suggesting the temperature gradient larger than 50 °C/mm. This run product was discarded from further investigations, because of the difficulty in picking up only cubic ^{13}C diamond grains from the fine-grained mixture.

The use of second configuration with the sample chamber located in the central hot spot of MgO capsule (Figure 2-2b) helped to avoid the problem caused by the temperature gradient. Provided the same temperature gradient as in the first configuration, an estimated temperature in the center of the sample was higher than 2350 °C for the runs 5K1838 and 5K1892, which ensures that the temperature was well within the stability field of cubic

diamond over the length of the sample. In these runs a complete conversion to cubic ^{13}C diamonds was confirmed by X-ray diffraction (Figure 2-3).
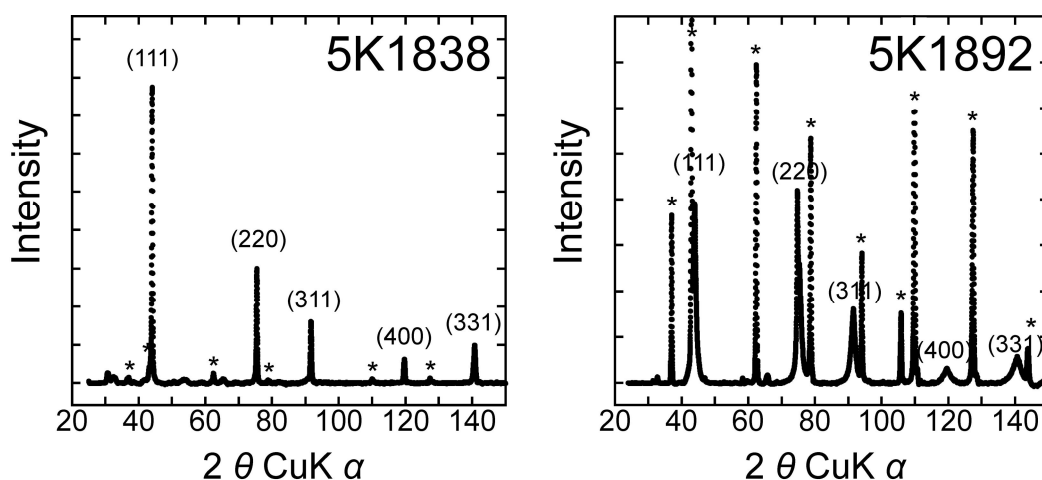
Figure 2-3. X-ray diffraction profiles of the diamond aggregate synthesized in the runs 5K1838 (left) and 5K1892 (right). The profiles correspond to that of cubic diamond, the numbers show Miller indices. The peaks indicated by stars are the diffraction peaks from MgO container.

Run product 5K1838 was further examined by field-emission scanning electron microscope (FE-SEM). FE-SEM images showed that this run product was an aggregate thoroughly consisted of platy diamonds, 10 to 20 μm in size (Figure 2-4). In contrast to the well-sintered structure of polycrystalline diamonds described in the previous works (Irifune et al., 2003; Ohfuji et al., 2012), the recovered samples were very fragile and were easily separated into small (20-60 μm) pieces suitable for the measurements in a diamond anvil cell.

Figure 2-4. FE-SEM images of the run product 5K1838, which was found to consist of diamond plates 10 to 20 μm in size.

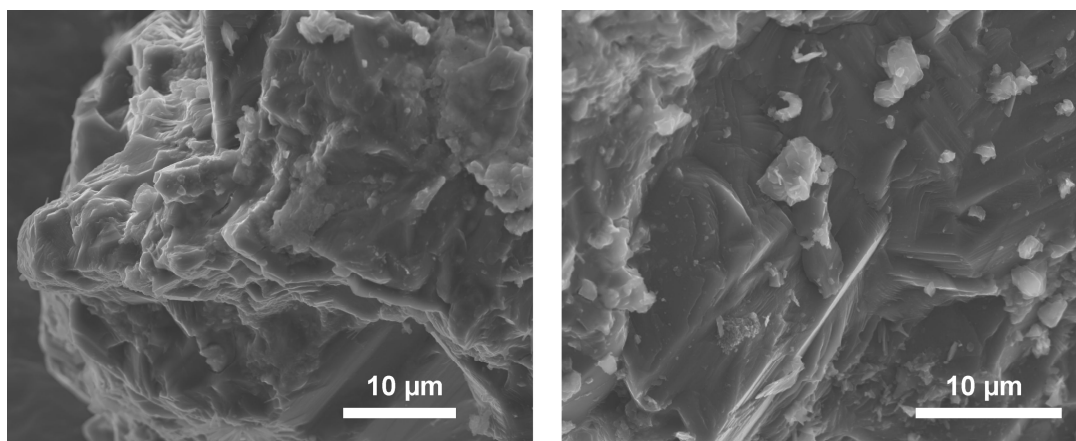Measurement of Raman peak at ambient conditions for the ^{13}C diamonds synthesized in the runs 5K1838 and 5K1992 was performed in water in order to avoid heating by the excitation laser. Both products contained a characteristic first-order Raman peak at 1286.0(0.2) cm^{-1}, which had a small full width at half-maximum (FWHM = 4.4-7.0 cm^{-1}).

It was shown by Ohfuji et al. (2012) that the microtexture of polycrystalline diamond is largely dependent on the crystallinity of the starting material. Intensity of the Raman peak generally decreases with decreasing the grain size of diamond (Namba et al., 1992). Irifune et al. (2004) reported a weak and broad Raman peak (FWHM ~ 10-20cm^{-1}) for the nano-polycrystalline diamond. In the present study synthesis was carried out using amorphous ^{13}C powder as a starting material and the product was fragile, fine-grained diamond aggregate. The grain size of 10-20 μm gave a sharp Raman peak, which made possible a precise measurement of its position. These features of the optical pressure sensor are essential for the monitoring of pressure inside the sample chamber of HDAC.

2.2. Application to HDAC experiments at simultaneous high temperature and high pressure

2.2.1. Cross-calibration experiments with ruby, phase transitions in H_2O system and quartz as independent pressure references

In order to check the precision of the synthesized ^{13}C diamond at simultaneous high pressures and temperatures, two series of cross-calibration experiments were carried out using an externally heated hydrothermal diamond anvil cell (Bassett et al., 1993) with 1 mm culets. Ruby R_1 fluorescence line and H_2O phase transitions were used as pressure references in the first series of cross-calibration experiments, and quartz 464 cm^{-1} Raman shift in the second series of experiments.

In the first series of experiments a small piece of the ^{13}C diamond aggregate (~50 µm in size) was loaded into a 500 µm hole of 125 µm thick rhenium gasket together with a ruby chip (Edmund Optics Inc.) and a drop of deionized H_2O, which served as a pressure medium. H_2O pressure medium provides hydrostatic conditions at least up to 5 GPa (Piermarini et al., 1973). Temperature was monitored by the alumel-chromel thermocouples with the junction attached to near the culet surfaces of the upper and lower anvils. EMF of thermocouple was calibrated by the melting points of NH_4NO_3 (169.6 °C), $NaNO_3$ (306.8 °C) and CsCl (645 °C). During experiments the temperature was controlled to within ± 1 °C.

By tightening nuts on the three posts of HDAC, the pressure in the sample chamber was increased up to the phase transition water–ice VI or ice VI–ice VII, then the sample assembly was heated and cooled in the

temperature range 24-185 °C at a rate of 3 °C/min. Phase transitions of H_2O were detected visually (Figure 2-5) and confirmed by Raman spectroscopy.
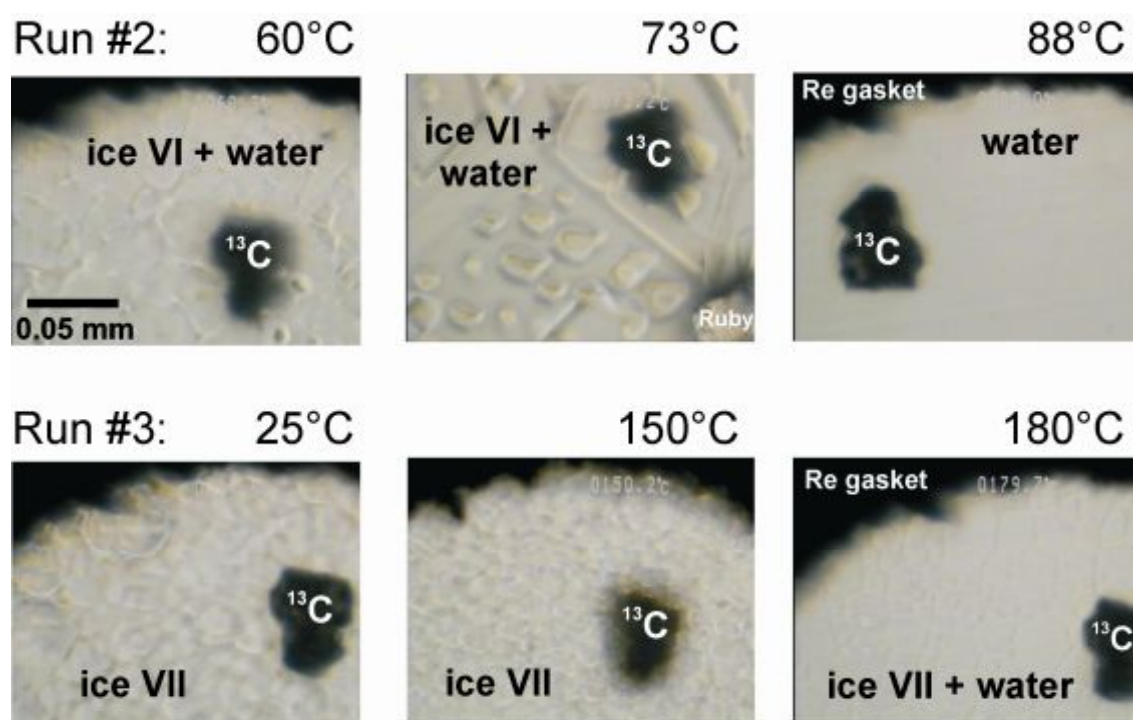
Figure 2-5. H_2O phases observed during cross-calibration experiments in HDAC. Photomicrographs were taken in the run #2 and run #3 (Table 2-1) with the same scale. Mineralogical Magazine is acknowledged for the permission to reproduce the figure published in Chertkova et al. (2014).

The ^{13}C diamond aggregate and H_2O pressure medium were probed *in situ* with a Jasco RMP-330 confocal micro-Raman system equipped with a 532 nm (Nd-YAG double frequency) laser operated at 8.4 mW for excitation, a 2400 gr/mm holographic grating, a 300 mm focal length mirror, and a Peltier cooled CCD array detector (1024 x 256 pixels). This system was outfitted to a Jasco IRT-7000 microscope with an Olympus infinity-corrected

objective (50X/0.35N.A. 41° convergence angle/3.6 mm focal length), an imaging lens (20.0 mm focal length), and confocal optics with a 100 µm pinhole aperture, which yields an excitation volume of 20 µm in diameter and ~50 µm in depth in the 180° scattering geometry. The ruby fluorescence spectra were also acquired with the same system.

Spectrum acquisitions were conducted every 50 °C of heating/cooling and at the temperatures when a phase transition of the H_2O pressure medium was visually observed. The spectrometer was calibrated to the Hg lines (577 and 579 nm, NIST) and the Ne lines (585, 588, 594, 598 and 603 nm, NIST) before experiments. Reproducibility of the measurements was monitored by measuring the Ne 585 nm line at high temperature and high pressure during experiments. The reproducibly was estimated to be ±0.65 cm^{-1}. Obtained spectra were processed for the calculation of pressure inside the sample chamber of HDAC. Both ^{13}C diamond and ruby peaks were fitted with the Voigt function.

A similar approach was used in the second series of experiments. Doubly polished ~50 µm thick transparent quartz piece (Wako Pure Chemical Industries, Ltd.) was loaded into 250 µm or 500 µm gasket hole of 125 µm thick rhenium gasket together with a small piece of ^{13}C diamond aggregate and a small drop of deionized water. The sample assembly was heated up to 500 °C and the Raman spectra of quartz and ^{13}C diamond were taken at 300 °C, 400 °C and 500 °C. Spectrometer was calibrated to the 520.5 cm^{-1} Si Raman peak before heating, and reproducibility of the measurements was monitored by observing the 585 nm Ne line during the experiments.

Figure 2-6 shows typical spectra obtained *in situ* for the ^{13}C diamond pressure sensor and the ruby pressure reference at various *P-T* conditions.

Ruby fluorescence lines broadened rapidly with increasing temperature, and with the chosen optical configuration of Raman spectrometer (holographic grating of 2400 gr/mm) it was difficult to determine their positions at temperatures above 170 °C.
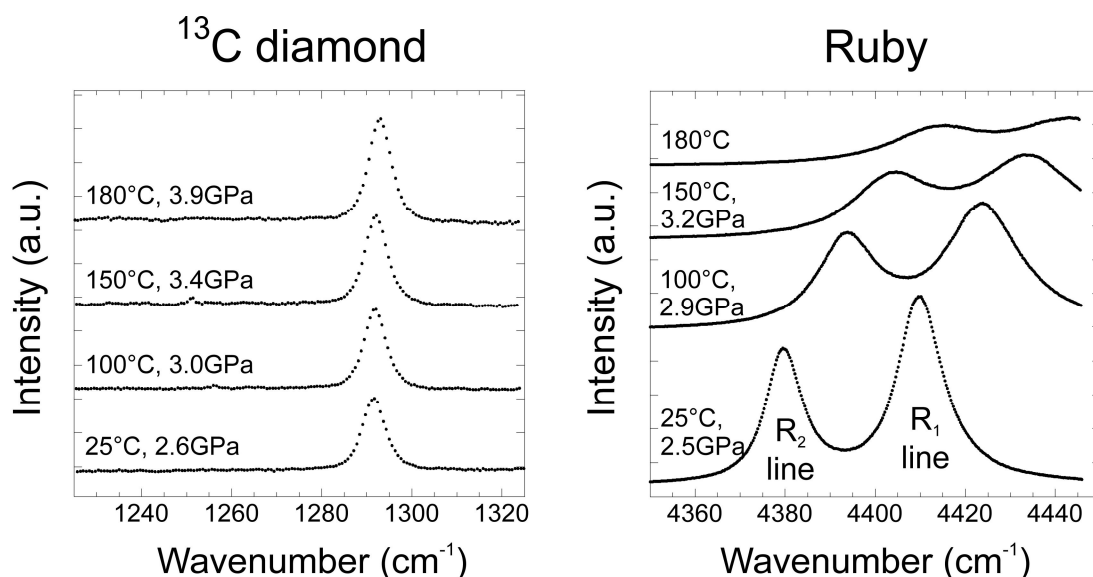
Figure 2-6. The shift of ^{13}C diamond Raman peak (left) and ruby fluorescence lines (right) with pressure and temperature (run #4 in Table 2-1). Mineralogical Magazine is acknowledged for the permission to reproduce the figure published in Chertkova et al. (2014).

Experimental pressures were calculated based on the Raman shift of ^{13}C diamond, ruby R$_1$ fluorescence line and quartz 464 cm^{-1} Raman peak.

Calibration of Schiferl et al. (1997) was applied to the Raman shift of ^{13}C diamond, assuming that the effects of pressure and temperature on the Raman shift are decoupled:

$$\nu_{0.1MPa, T} = \nu_{0.1MPa, 298K} + 0.45 - 0.000736 \, (T \, (K) - 200)^{1.5}, \qquad (2-1)$$

$$P \, (GPa) = (\nu_{P,T} - \nu_{0.1MPa, T}) \, / \, 2.83, \qquad (2-2)$$

where $v_{P,T}$ and $v_{0.1MPa,298K}$ are the ^{13}C diamond shifts (in cm^{-1}) at pressure (P) and temperature (200 K≤T≤1330 K) and at ambient conditions (0.1 MPa, 298 K) respectively.

Calibration of the ^{13}C diamond Raman shift by Mysen and Yamashita (2010) was used for comparison:

$$P(\text{MPa}) = \frac{v_{P,T} - v_{0.1MPa,25°C} + 1.065 \times 10^{-2} T(°C) + 1.769 \times 10^{-5} T^2(°C)}{0.002707} \qquad (2\text{-}3)$$

Calibrations of Ragan et al. (1992) and Zha et al. (2000) were applied to the ruby R$_1$ line for the independent pressure evaluation:

$$R_1 \text{ (cm}^{-1}) = 14423 + 4.49 \times 10^{-2} T \text{ (K)} - 4.81 \times 10^{-4} T \text{ (K)}^2 +$$
$$3.71 \times 10^{-7} T \text{ (K)}^3, \qquad (2\text{-}4)$$

$$P \text{ (GPa)} = (1904 / 7.715) [(\lambda / \lambda_0)^{7.715} - 1]. \qquad (2\text{-}5)$$

Pressure effect on the 464 cm^{-1} quartz Raman shift was used as another independent pressure reference employing the calibration of Schmidt and Ziemann (2000):

$$v_{0.1MPa, T} = v_{0.1MPa,25°C} + 2.50136 \times 10^{-11} T \text{ (°C)}^4 + 1.46454 \times 10^{-8} T \text{ (°C)}^3$$
$$- 1.801 \times 10^{-5} T \text{ (°C)}^2 - 0.01216 T \text{ (°C)} + 0.29, \qquad (2\text{-}6)$$

$$P \text{ (MPa)} = 0.36079 (v_{P,T} - v_{0.1MPa, T})^2 + 110.86 (v_{P,T} - v_{0.1MPa, T}). \qquad (2\text{-}7)$$

Resulting pressure values for the first series of cross-calibration experiments are shown in Table 2-1 and for the second series of experiments in Table 2-2.

	T (°C)	H_2O phase	$\Delta v\_^{13}C$ (cm^{-1})	Δv_ruby (cm^{-1})	$P\_^{13}C$ (GPa)	P_ruby (GPa)
Run #1	25	ice VII	9.63	25.44	3.49	3.39
	50	ice VII	10.12	30.98	3.77	3.77
	100	ice VII	10.98	42.24	4.31	4.24
	150	ice VII	11.79		4.87	
Run #2	24	ice VI	3.19	9.76	1.22	1.35
	50	ice VI	3.43	14.37	1.41	1.55
	60	ice VI+water	3.97	17.66	1.64	1.78
	88	water	4.43	24.31	1.94	2.09
	50	ice VI	4.58	17.46	1.81	1.96
	25	ice VI	4.12	12.04	1.55	1.65
Run #3	25	ice VII	6.10	16.52	2.25	2.19
	50	ice VII	6.01	19.98	2.32	2.29
	100	ice VII	6.81	31.17	2.84	2.76
	150	ice VII	7.58	42.58	3.39	3.21
	180	ice VII+water	8.53		3.90	
Run #4	25	ice VII	7.12	18.64	2.61	2.48
	50	ice VII	7.31	23.04	2.78	2.70
	100	ice VII	7.38	32.58	3.04	2.94
	150	ice VII	7.61	42.79	3.40	3.23
	170	ice VII+water	8.17	49.33	3.71	3.68
	180	ice VII+water	8.49		3.89	
	185	water	7.64		3.62	

Table 2-1. Conditions of the first series of cross-calibration experiments in HDAC: measured temperature (T), observed pressure medium phase, frequency shifts of ^{13}C diamond and ruby ($\Delta v\_^{13}C$ and Δv_ruby = measured frequency at the experimental pressure and temperature minus the frequency at ambient conditions). Also shown calculated pressure values ($P\_^{13}C$, calculated from ^{13}C diamond Raman shift with the calibration of Schiferl et al. (1997); P_ruby, calculated from ruby R_1 fluorescence line with the calibrations of Ragan et al. (1992) and Zha et al. (2000)). Mineralogical Magazine is acknowledged for the permission to reproduce the table published in Chertkova et al. (2014).

	T (°C)	$\Delta v\_^{13}C$ (cm^{-1})	Δv_Qtz (cm^{-1})	$P\_^{13}C$ *Sch 97* (GPa)	$P\_^{13}C$ *M&Ya 10* (GPa)	P_Qtz (GPa)
Run #5	23	0.05	0.35	0.10	0.11	0.04
	300	-2.75	2.45	0.74	0.75	0.76
	400	-4.76	3.24	0.84	0.86	1.01
	500	-6.42	5.43	1.14	1.23	1.37
Run #6	25	0.21	0.97	0.17	0.18	0.11
	300	-3.36	0.86	0.53	0.53	0.58
	400	-5.30	1.47	0.64	0.66	0.82
	500	-7.37	2.06	0.81	0.88	1.00
Run #7	24	0.73	3.34	0.35	0.37	0.37
	300	-1.34	5.41	1.24	1.27	1.09
	400	-3.24	7.45	1.37	1.42	1.48
	500*	-6.16	6.07	1.23	1.33	1.44
Run #8	25	2.17	6.66	0.86	0.90	0.74
	300	-0.34	9.08	1.60	1.64	1.50
	400	-2.37	10.00	1.68	1.74	1.76
	500	-4.30	11.22	1.89	2.01	2.01

Table 2-2. Conditions of the second series of cross-calibration experiments in HDAC: temperature (T), frequency shifts of ^{13}C diamond and quartz ($\Delta v\_^{13}C$ and Δv_Qtz = measured frequency at the experimental pressure and temperature minus the frequency at ambient conditions). Calculated pressure values are shown as $P\_^{13}C$ *Sch 97* (using ^{13}C diamond Raman shift with the calibration of Schiferl et al. (1997)), $P\_^{13}C$ *M&Ya 10* (using ^{13}C diamond Raman shift with the calibration of Mysen and Yamashita (2010)) and P_Qtz (using quartz Raman shift with the calibration of Schmidt and Ziemann (2000)). A star next to the temperature value indicates expansion of the gasket sample chamber during heating prior to the spectroscopic measurements. Mineralogical Magazine is acknowledged for the permission to reproduce the table published in Chertkova et al. (2014).

The pressure–temperature paths calculated in the first series of experiments are compared with the reference H_2O phase boundaries in Figure 2-7. Run #1 ended at 168 °C when the lower diamond anvil was broken at about 5 GPa. In the most cases ice–water transition was accompanied by the deformation of the gasket and H_2O leakage. Fortunately, in the run #2 the deformation of the gasket was not significant and it was possible to test the reproducibility in the phase appearance near the melting curve. While repeatedly heated/cooled at 3 °C/min near the liquidus, ice VI melted at 88 °C and water solidified to ice VI at 79 °C. Assuming that phase equilibration is faster at higher temperatures, a small difference between the temperatures of melting and solidification for ice VI indicates that the heating rate of 3 °C/min is sufficiently slow to achieve equilibrium in this system.
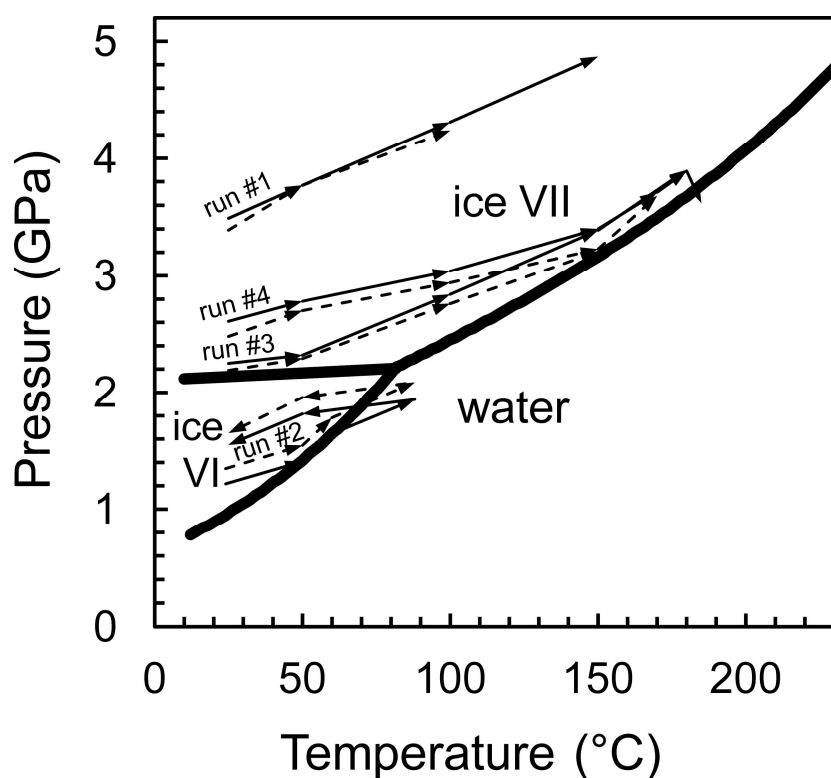
Figure 2-7. The Experimental pressure–temperature paths plotted on the reference phase diagram of H_2O (melting curves from Wagner and Pruss 2002; ice VI–ice VII line from Johari et al. 1974). Solid arrows correspond to the pressure values calculated using the Raman shift of synthesized ^{13}C diamond, dotted arrows – to the pressure values obtained with the ruby R_1 fluorescence line. Mineralogical Magazine is acknowledged for the permission to reproduce the figure published in Chertkova et al. (2014).

Since pressure–temperature conditions of the second series of cross-calibration experiments were in the field of stability of α-quartz, phase transitions were not observed in these experiments.

2.2.2. Precision of pressure determination

Experimental paths of the runs #2, 3 and 4 were very close to the melting curves since coexistence of solid and liquid phase was observed over a range of pressure and temperature conditions. Coexistence of ice VI and water was observed at 58-87 °C in the run #2 (the pressure obtained with ^{13}C diamond is 1.64 GPa at 60 °C), coexistence of ice VII and water was observed at 152-180 °C in the run #3 (obtained pressure is 3.90 GPa at 180 °C) and at 166-184 °C in the run #4 (3.71 GPa at 170 °C and 3.89 GPa at 180 °C) (Table 2-1). The pressure values obtained using ^{13}C diamond pressure sensor are in agreement with the reference phase boundaries of H_2O system within 0.22 GPa: 1.64 GPa at 60 °C for the ice VI melting curve, 3.50 GPa at 170 °C and 3.68 GPa at 180 °C for the ice VII melting curve (Wagner and Pruss, 2002) (Figure 2-7). It is also notable that the average difference in pressure values obtained with the synthesized ^{13}C diamond and the ruby pressure reference is 0.10 GPa, while the maximum difference is 0.18 GPa (Table 2-1). These values lie

within the reported uncertainty of calibrations for ^{13}C diamond of $\pm$ 0.3 GPa (Schiferl et al., 1997) (Figure 2-8).

The pressure values obtained from the ^{13}C diamond Raman shift based on the calibration of Schiferl et al. (1997) were also compared with those calculated from the quartz 464 cm^{-1} Raman shift based on the calibration of Schmidt and Ziemann (2000) (Table 2-2, Figure 2-8). All the data are in agreement within an average difference of 0.12 GPa, which is much smaller than the uncertainty reported by Schiferl et al. (1997). At the same time, the pressure values obtained from the ^{13}C diamond Raman shift with the calibration of Mysen and Yamashita (2010) at pressures up to 2 GPa yield consistent results within an average difference of 0.10 GPa (Table 2-2).
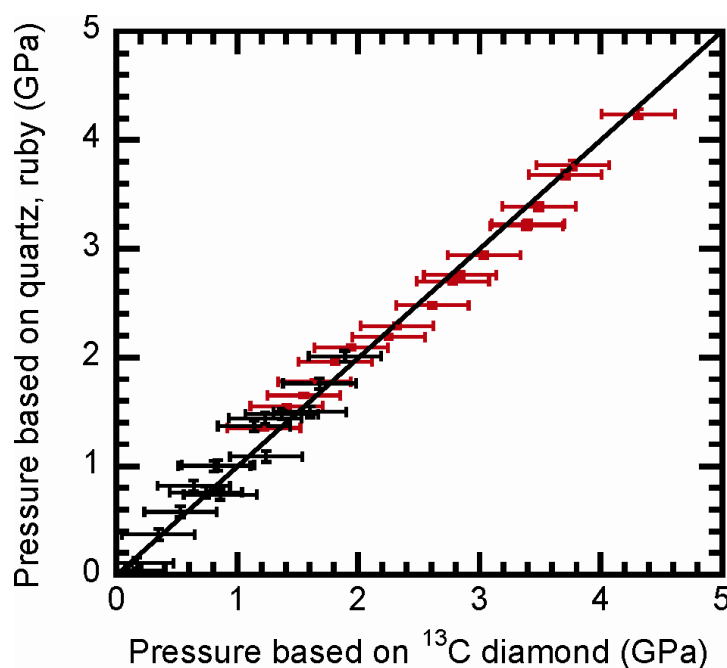

Figure 2-8. Comparison between experimental pressure values calculated based on ^{13}C diamond pressure sensor and quartz (black dots), ruby (red dots) pressure references. Error bars correspond to the reported uncertainty of pressure calculation: $\pm$ 0.3 GPa for ^{13}C

diamond (Schiferl et al., 1997), ± 0.05 GPa for quartz (Schmidt and Ziemann, 2000) and 1% for ruby (Zha et al., 2000). All data fall close to the 1 : 1 line, indicating a good precision of ^{13}C diamond pressure sensor in the studied range of pressure and temperature. Mineralogical Magazine is acknowledged for the permission to reproduce the figure published in Chertkova et al. (2014).

The results of cross-calibration experiments of this study confirm that for the ^{13}C diamond Raman shift, the pressure and temperature effects can be assessed separately to 500 °C and 4.2 GPa. This is consistent with the results of the previous studies (Datchi et al., 2007; Mysen and Yamashita, 2010). Therefore, a combination of the present experimental results and those of the previous studies shows applicability of ^{13}C diamond as a precise pressure sensor, with the accuracy better than ± 0.3 GPa, over a wide range of experimental conditions. The Raman peak of the synthesized ^{13}C diamond broadens only slightly at high temperatures and pressures, e.g., 8.2 cm^{-1} of FWHM at 500 °C and 2 GPa. All these features make the synthesized ^{13}C diamond suitable as a pressure sensor for HDAC experiments at simultaneous high temperature and high pressure. Synthesis by the Kawai-type multianvil apparatus provides enough amount of ^{13}C diamond for more than tens of HDAC experiments.

CHAPTER 3

SPECTROSCOPIC MEASUREMENTS OF HYDROUS SODIUM DISILICATE MELTS USING HDAC

3.1. Experimental methods

After development of the procedure for determination of pressure in HDAC experiments I proceeded to the next task of this work: evaluation of the effects of pressure and temperature on water speciation equilibrium in the depolymerized $Na_2Si_2O_5$ melts. Water speciation equilibrium has never been evaluated for the depolymerized melts at high temperatures and pressures. This task required a precise control of the total water content of the melt and special analytical equipment that allowed simultaneous near-infrared (NIR) and Raman measurements at high temperatures and pressures. Precise control of the total water content was achieved by using a series of hydrous glasses as a starting material for the experiments. At high temperatures these glasses were transformed to melts and served as a pressure medium, thus providing an opportunity to perform full quantitative evaluation of the NIR absorption spectra at constant total water content. Unique analytical equipment applied in this study is described in details in section 3.1.2.

3.1.1. Preparation of starting glasses

Anhydrous sodium disilicate glass was prepared from the mixture of reagent grade SiO_2 and Na_2CO_3 powders in the ratio corresponding to $Na_2O \cdot 2SiO_2$ molar composition after decarbonation. This mixture was melted in a Pt crucible for three hours at 1400 °C and 1 atm in air, quenched to the glass by immersing the crucible in water, then grinded and re-melted for one hour to ensure the homogeneity. Chemical composition of the obtained glass was checked by electron microprobe analysis (JEOL JXA-8800) with the

defocused beam of 50 μm, beam current 1.0 nA, acceleration voltage 15 kV. Reliability of the analysis was tested by measuring the standard reference material SRM 621 (soda-lime silicate container glass provided by National Institute of Standard and Technology, USA) using the same analytical conditions (Table 3-1).

wt.%	NS2		SRM 621	
SiO_2	65.47 (0.33)	[65.97]	70.68 (0.48)	[71.13][a]
Al_2O_3	0.04 (0.05)		3.06 (0.17)	[2.76]
CaO	0.03 (0.04)		11.21 (0.49)	[10.71]
Na_2O	34.09 (0.60)	[34.03]	12.89 (0.50)	[12.74]
K_2O	0.04 (0.06)		2.04 (0.25)	[2.01]
Total	99.68 (0.39)		99.87 (0.51)	
	$n = 9$[b]		$n = 9$	
[a] Concentration of each oxide component for the reference soda-lime container glass certified by NIST (USA). [b] n - number of analyses. 1σ standard deviation is shown in parentheses.				

Table 3-1. Compositions of the synthesized anhydrous glass (NS2) and of the soda-lime container glass (SRM621) measured by the same procedure as a reference. Nominal compositions are shown in the blankets.

Hydrous glasses (1.3 to 8.1 wt.% total water) were synthesized from the anhydrous $Na_2Si_2O_5$ glass grinded to 0.5-1 mm pieces and the appropriate amount of deionized water in the sealed 5mm-diameter Pt capsules. Synthesis was carried out in a Kobelco internally heated pressure vessel (IHPV) (Yamashita, 1999) at 1200 °C and ~200 MPa for 24 h. This technique provides isobaric quenching by letting the capsule fall into the cold bottom of the vessel.
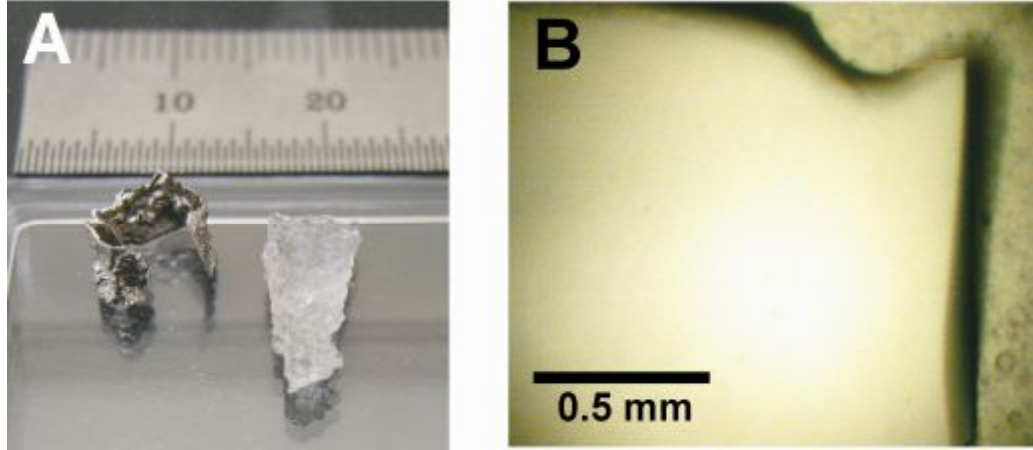
Figure 3-1. Photographs of clear transparent hydrous $Na_2Si_2O_5$ glass synthesized in the IHPV (4wt.% total water): (a) glass recovered intact from the Pt capsule after quenching, (b) doubly polished thin section under the optical microscope with transmission light.

Recovered hydrous glasses (Figure 3-1) were transparent, free from crystals and bubbles. Relatively big pieces (24-180 mg) were selected from the each synthesis product for the determination of glass density using Archimedes' principle. The weight of the selected glass pieces was repeatedly measured in air and in toluene (Table 3-2), then the glass density was calculated with the formula:

$$\rho_{Glass} = \frac{W^{\text{in air}}}{W^{\text{in air}} - W^{\text{in toluene}}} \cdot \rho_{Toluene} \ , \tag{3-1}$$

where W denotes the weight of the glass piece (g) and $\rho_{Toluene}$ is the density of toluene (g l^{-1}) at the temperature of measurement. Density of toluene was determined using the density–temperature relation given by National Institute of Standard and Technology (NIST certification SRM211d).

Loaded amount of water	$W^{in\ air}$ (g)	$W^{in\ toluene}$ (g)	Temperature (°C)	$\rho_{Toluene}$ (g l^{-1})	ρ_{Glass} (g l^{-1})	Average ρ_{Glass} (g l^{-1})
0.9 wt.%	0.14079	0.09196	23.7	863.4	2489	2490
	0.14076	0.09200	23.7	863.4	2492	
	0.14079	0.09195	23.7	863.4	2489	
2.0 wt.%	0.02405	0.01556	21.3	865.6	2452	2469
	0.02378	0.01550	21.8	865.2	2485	
	0.02381	0.01547	22.0	865.0	2469	
4.0 wt.%	0.17853	0.11537	20.6	866.3	2449	2448
	0.17851	0.11543	20.6	866.3	2451	
	0.17873	0.11536	20.6	866.3	2443	
5.9 wt.%	0.13283	0.08524	22.0	865.0	2414	2415
	0.13242	0.08499	22.2	864.8	2414	
	0.13238	0.08501	22.3	864.7	2416	
6.1 wt.%	0.11745	0.07544	23.5	863.6	2414	2415
	0.11737	0.07544	23.5	863.6	2417	
	0.11750	0.07547	23.5	863.6	2414	
7.9 wt.%	0.09358	0.05945	20.7	866.2	2375	2374
	0.09355	0.05944	20.7	866.2	2376	
	0.09357	0.05939	20.7	866.2	2371	

Table 3-2. Parameters for the density determination of the six hydrous $Na_2Si_2O_5$ glasses synthesized in the IHPV.

Several doubly polished thin sections (0.2-0.7 mm thick) were prepared from the each synthesis product for the near-infrared (NIR) and Raman spectroscopic analyses. While the thin sections were polished, only the ethanol-based liquid was used for lubrication (Struers DP-lubricant yellow) to avoid hydration of the sample surface. Their thickness was measured by a Mitsutoyo Litematic digital displacement gauge with the accuracy of ±2 µm.

3.1.2. Experimental setup of NIR and Raman spectroscopy

NIR spectroscopy was carried out using a Jasco FTIR-6200 Fourier-transform spectrometer with a Si-coated CaF_2 beam splitter and a halogen

NIR light source. The NIR light was aimed at 50×50 µm sample spot by a Jasco IRT-7000 microscope with Cassegrain optics (10X/0.45N.A. 54° convergence angle) in the transmission mode. The transmitted light was received by a LN_2-cooled InSb detector, and 100 to 256 scans were accumulated for each spectrum with a spectral resolution of 4 cm^{-1}. The NIR light path was continuously purged with the nitrogen gas to minimize atmospheric background in the spectra.

Raman spectroscopy was carried out using a Jasco RMP-330 confocal micro-Raman system equipped with a 532 nm (Nd-YAG double frequency) laser operated at 8.4 mW for excitation, a 2400 gr/mm holographic grating, a 300 mm focal length mirror, and a Peltier cooled CCD array detector (1024 x 256 pixels). This system was outfitted to IRT-7000 microscope (shared with NIR spectroscopy) with an Olympus infinity-corrected objective (50X/0.35N.A. 41° convergence angle/3.6 mm focal length), an imaging lens (20.0 mm focal length) and confocal optics with a 100 µm pinhole aperture, which yields an excitation volume of 20 µm in diameter and ~50 µm in depth in the 180° scattering geometry. The Raman scattering light was transmitted from the confocal optics to the spectrometer by a 100 µm diameter optical fiber with a 50 µm-wide slit at the exit. The spectra were collected during 2 acquisitions of 60 sec or 120 sec exposure. The spectrometer was calibrated to the Hg lines (577 and 579 nm, NIST) and the Ne lines (585, 588, and 594 nm, NIST), the indene Raman peaks (533.7, 730.4, 861.0, 1018.3, 1067.8, 1154.3, 1205.6, 1225.6, 1361.6, 1393.6, 1457.6, 1552.7, and 1610.2 cm^{-1}, ASTM E1840-96), and the polystyrene Raman peaks (620.9, 795.8, 1001.4, 1031.8, 1155.3, 1583.1, and 1602.3 cm^{-1}, ASTM E1840-96). Accuracy of

measurement was estimated to be better than ± 3 cm^{-1}. Reproducibility was better than ± 0.5 cm^{-1}.

Optical access to the sample position can be switched in the IRT-7000 microscope from the Cassegrain optics to the objective lens – confocal optics at any time, which made it possible to probe the sample by both NIR spectroscopy and Raman spectroscopy *in situ* without interruption.

3.1.3. Spectroscopic characterization of the starting glasses at room temperature

Figure 3-2 shows typical NIR spectra of the hydrous $Na_2Si_2O_5$ glasses at room temperature. At least five different spots (50×50 µm) of each sample were analyzed to test for homogeneity.

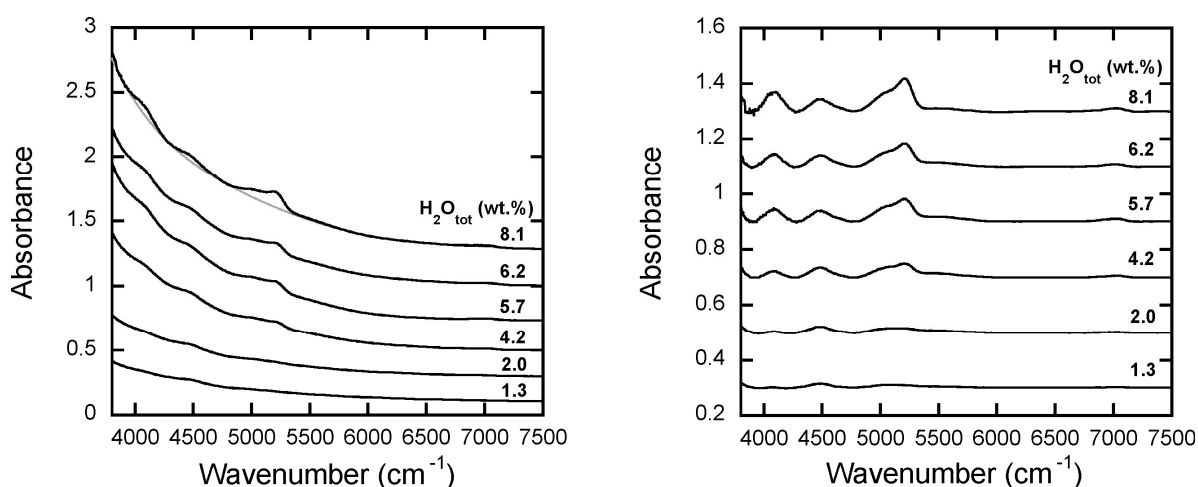**Figure 3-2.** Representative room temperature NIR spectra of the hydrous $Na_2Si_2O_5$ glass thin sections. An example of the baseline is illustrated by the grey curve for the glass containing 8.1 wt.% total water. The baseline-corrected spectra are shown on right hand side. Spectra are scaled to a thickness of 500 µm and offset for clarity. H_2O_{tot} denotes total water as a sum of water as OH groups and water as H_2O molecules.

Two absorption bands due to dissolved water species can be seen in the spectra (Figure 3-2) based on the previously reported bands assignments (e.g., Bartholomew et al., 1980; Wu, 1980; Stolper, 1982a; Zotov and Keppler, 1998). The band at around 4500 cm^{-1} is a combination mode of the fundamental stretching vibrations of structurally bound OH groups and the band near 5200 cm^{-1} is a combination mode of the fundamental stretching and bending vibrations of H_2O molecules. These bands were separated from the background by subtracting a 6th order polynomial, fitted to the minima between the 4000 cm^{-1}, 4500 cm^{-1}, 5200 cm^{-1} and 7100 cm^{-1} bands. The band near 5200 cm^{-1} has a complex shape which can be fitted by the three Gaussian sub-band components, one centered at 5200 cm^{-1}, one at 5100 cm^{-1} and one at 5500 cm^{-1} (Figure 3-3). Yamashita et al. (2008) have shown that in the room temperature spectra of sodium disilicate glasses, intensity of the 5500 cm^{-1} sub-band component is correlated to the total water content rather than to the concentration of molecular H_2O. For the quantitative analysis of molecular H_2O species, the 5500 cm^{-1} sub-band was subtracted from the overall intensity of the 5200 cm^{-1} band as a background component.
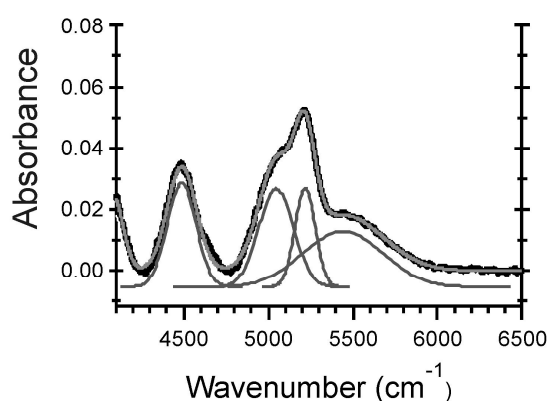
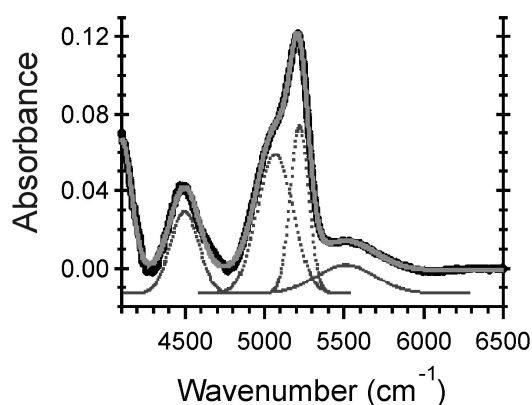A 4.2 wt.% total water   B 8.0 wt.% total water

Figure 3-3. Examples of the NIR absorption spectra deconvolution for the thin sections containing 4.2 wt.% total water (a) and 8.0 wt.% total water (b). The OH group band at ~4500 cm^{-1} is fitted with a single Gaussian peak and the molecular H_2O band at ~5200 cm^{-1} with the three Gaussian sub-components.

The peak heights of NIR bands near 4500 cm^{-1} and 5200 cm^{-1} were used for the determination of OH groups and molecular H_2O abundances respectively. Total water content of the glasses was calculated as a sum of OH groups and molecular H_2O with the molar absorption coefficients $\varepsilon_{4500} = 0.21$ and $\varepsilon_{5200} = 0.36$ L mol^{-1} cm^{-1} (calibration A in Yamashita et al., 2008), then concentrations of water species were recalculated employing the total water content-dependent molar absorption coefficients of NIR bands near 4500 cm^{-1} and 5200 cm^{-1} (calibration B). Obtained total water contents (Table 3-3) were in agreement with the loaded amount of water within 0.2 wt.%, except for the run product with 1.3 wt.% total water (loaded amount was 0.9 wt.% H_2O), probably due to a hydroscopic behavior of the dry $Na_2Si_2O_5$ glass. In order to minimize hydration of the synthesized glasses by atmospheric moisture they were stored in a desiccator with P_2O_5 drying agent and high-temperature experiments were performed right after the preparation of starting thin sections.

Total water content (wt.%)	Density (g l⁻¹)	Thickness (cm)	A_{4500}[a]	A_{5200}	C_{OH} Calib A (wt.%)	C_{H2Om} Calib A (wt.%)	C_{OH} Calib B (wt.%)	C_{H2Om} Calib B (wt.%)
1.34 (0.08)[b]	2490	0.0725	0.0216	0.0113	1.03	0.31	0.99 (0.07)[c]	0.30 (0.03)[c]
1.97 (0.10)	2469	0.0605	0.0266	0.0132	1.53	0.44	1.50 (0.10)	0.42 (0.04)
2.09 (0.12)	2469	0.0478	0.0216	0.0123	1.57	0.52	1.55 (0.11)	0.49 (0.05)
4.04 (0.22)	2448	0.0234	0.0159	0.0190	2.38	1.66	2.54 (0.20)	1.51 (0.11)
4.12 (0.18)	2448	0.0352	0.0245	0.0289	2.44	1.68	2.61 (0.16)	1.53 (0.08)
4.19 (0.16)	2448	0.0581	0.0416	0.0477	2.51	1.68	2.70 (0.14)	1.53 (0.07)
5.69 (0.19)	2415	0.0598	0.0452	0.0865	2.69	3.00	3.07 (0.15)	2.66 (0.11)
6.15 (0.21)	2415	0.0520	0.0433	0.0800	2.96	3.19	3.46 (0.17)	2.81 (0.12)
8.03 (0.25)	2374	0.0540	0.0464	0.1261	3.11	4.92	3.96 (0.18)	4.23 (0.18)
8.07 (0.25)	2374	0.0633	0.0550	0.148	3.14	4.93	4.01 (0.17)	4.23 (0.18)

[a] A_{4500} and A_{5200} denote peak heights of the respective bands, C_{OH} and C_{H2Om} denote water as OH groups and water as H_2O molecules.

[b] Molar absorption coefficients ε_{4500}=0.21(0.01) and ε_{5200}=0.36(0.01) (Calibration A in Yamashita et al., 2008) were used for the calculation of total water content.

[c] Total water content-dependent molar absorption coefficients (Calibration B in Yamashita et al., 2008) were employed for the precise determination of water species abundances.

Estimated uncertainties are: ±50 g l⁻¹ for density, ±0.0002 cm for thickness, ±0.001 for peak heights. Errors shown in parentheses were estimated by propagating these uncertainties into the calculated values.

Table 3-3. NIR data for the hydrous $Na_2Si_2O_5$ glass thin sections.

Figure 3-3 shows the Raman spectra of the $Na_2Si_2O_5$ glasses measured at room temperature. The spectra were collected in the spectral region of Si–O stretching vibrations of Q^n species (in this notation Q corresponds to a SiO_4 tetrahedron and n indicates the number of its bridging oxygens; e.g., Mysen and Richet, 2005). A linear background fitted in the regions 800-810 cm⁻¹ and 1200-1210 cm⁻¹ was subtracted from the spectrum and a temperature-frequency correction for the Raman intensities (Long, 1977; Neuville et al., 2014) was made. Obtained spectra were fitted with the Gaussian functions using Igor software and the portion of each Raman peak was determined as the ratio of its integrated intensity to the sum of integrated intensities of fitted peaks.
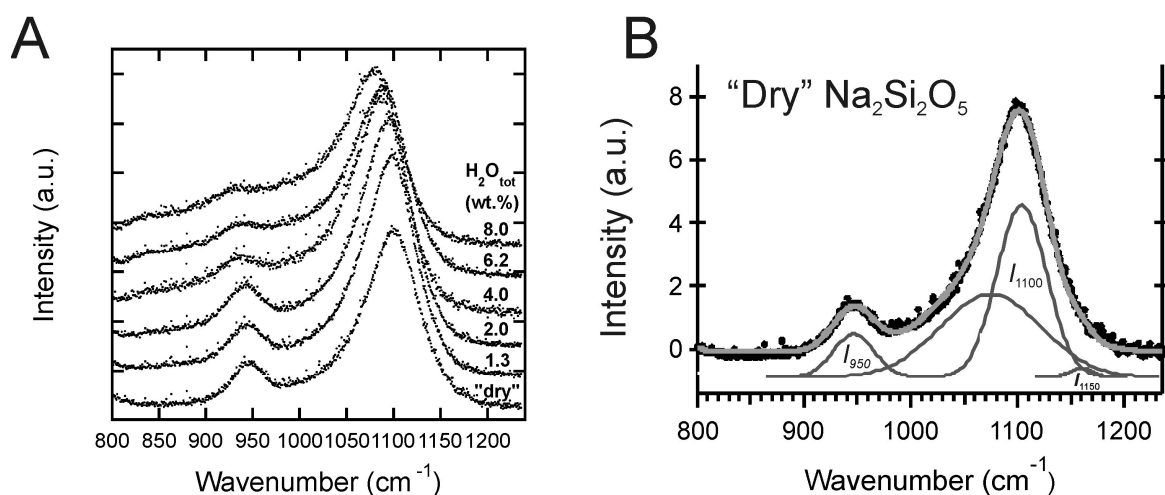
Figure 3-4. (a) Room temperature Raman spectra of the $Na_2Si_2O_5$ glass thin sections containing different water contents. (b) Raman peaks deconvolution for the dry $Na_2Si_2O_5$ glass. The spectrum is scaled to the sum of 950 cm^{-1}, 1100 cm^{-1} and 1150 cm^{-1} integrated peak intensities ($I_{950} + I_{1100} + I_{1150}$) of 400.

In the Raman spectra of $Na_2Si_2O_5$ glasses several peaks were observed in the region between 850 and 1250 cm^{-1} (Figure 3-4). Raman peaks near 950 cm^{-1} and 1100 cm^{-1} were assigned to the stretching vibrations of Q^2 and Q^3 species respectively by a number of authors (e.g., Brawer and White, 1975; Furukawa et al., 1981; McMillan et al., 1992; Mysen and Frantz, 1993). A small peak near 1150 cm^{-1} was assigned to the Si–O stretching in Q^4 units by Mysen and his co-workers (Mysen and Frantz, 1993; Mysen and Cody, 2005). There is no agreement in the literature about the assignment for the broad peak near 1050 cm^{-1}. Fukumi et al. (1990) and McMillan et al. (1992) assigned this peak to the Si–O vibrations in Q^3 species associated with alkali metals or alkaline earths, Mysen and Cody (2005) related it with the Si–O vibrations in any structural unit that contains bridging oxygen, Malfait et al. (2008) discussed this peak as a contribution from Q^2 species. Due to the

uncertainty in assignment, this peak will not be included in the following analysis of measured Raman spectra.

Mysen and Cody (2005) suggested a linear relationship between the integrated intensities of Raman peaks and the mole fractions of Q^n species in the $Na_2Si_2O_5$ glasses:

$$X(Q^n) = C_i \cdot \frac{I_i}{\sum I_i},$$

(3-2)

where $I_i / \sum I_i$ is the ratio of the integrated intensity of the selected Raman peak to the sum of Raman intensities I_{950}, I_{1100} and I_{1150} of the respective peaks. C_i is a Raman scattering coefficient for the selected Raman peak. Once the Raman scattering coefficients are calibrated, measured Raman peaks intensities can be used for the calculation of Q^n species abundances in the glasses within the chosen range of water contents.

First, Q^n speciation in the dry $Na_2Si_2O_5$ glass was estimated for the calibration of Raman scattering coefficients. The quench rate (q) in the synthesis of anhydrous glass was in the order of 100 to 10 °C/second. For this range of quench rates the log viscosity at glass transition (η^{Tg}) varies from 9.3 to 10.3 Pa s (log η^{Tg} = log $10^{11.3}$ – log q, Dingwell and Webb, 1990). The viscosity–temperature relationships for dry $Na_2Si_2O_5$ (Richet and Bottinga, 1995) give the glass transition temperatures between 521 °C and 496 °C for this range of viscosities. The average value of 509 °C was taken for the calculation of Q^n species abundances using the temperature dependence of Q^n speciation in dry $Na_2Si_2O_5$ melts reported by Malfait et al. (2008). Obtained Q^n speciation for the dry glass at the glass transition temperature Tg ≈ 509 °C and the scattering coefficients (C_i) derived from the measured Raman peak

intensities are shown in Table 3-4. With the determined Raman scattering coefficients Q^n species abundances were calculated for the range of water contents from 1.3 to 8.0 wt.%. Results of this calculation procedure (Table 3-4) agree reasonably well with the Q^n species concentrations determined by NMR techniques in $Na_2Si_2O_5$ glasses containing 2.0, 3.8 and 7.7 wt.% total water (Xue and Kanzaki, 2004; Mysen and Cody, 2005).

Total w.c. (wt.%)	I_{950} [a]	I_{1100} [a]	I_{1150} [a]	Q^2 (mol.%)	Q^3 (mol.%)	Q^4 (mol.%)	Q^n Sum
"dry"				9.3 (0.9) [b]	81.5 (1.8) [b]	9.3 (0.9) [b]	100.1 (2.2)
	0.195 (0.004)	0.789 (0.003)	0.016 (0.004)				
C_i^c	47.7 (4.7)	103.3 (2.3)	581.3 (155.4)				
1.34 (0.08)	0.194 (0.004)	0.787 (0.004)	0.019 (0.004)	9.2 (0.9)	81.3 (1.9)	11.2 (3.8)	101.7 (4.3)
1.97 (0.10)	0.214 (0.004)	0.773 (0.003)	0.013 (0.003)	10.2 (1.0)	79.8 (1.8)	7.7 (2.7)	97.7 (3.4)
4.04 (0.22)	0.282 (0.015)	0.708 (0.008)	0.010 (0.004)	13.4 (1.5)	73.1 (1.8)	5.9 (2.8)	92.4 (3.7)
6.15 (0.21)	0.317 (0.015)	0.668 (0.009)	0.015 (0.003)	15.1 (1.7)	69.0 (1.8)	8.5 (2.2)	92.6 (3.3)
8.03 (0.25)	0.364 (0.022)	0.620 (0.018)	0.016 (0.018)	17.4 (2.0)	64.0 (2.3)	9.4 (10.7)	90.8 (11.1)

[a] I_{950}, I_{1100} and I_{1150} denote integrated intensities of the respective Raman peaks (errors are calculated based on the fitting uncertainties of peak heights and widths).

[b] Q^n speciation calculated at 509 °C using the temperature dependence reported in (Malfait et al., 2008).

[c] C_i – Raman scattering coefficients of the respective bands found for the dry $Na_2Si_2O_5$ as a ratio Q^n/I_i (errors were estimated based on the uncertainties in the Gaussian peak fitting and those reported in Malfait et al. (2008) for the Q^n species abundances at 800 K). Q^n speciation in hydrous glasses was calculated using obtained Raman scattering coefficients.

Table 3-4. Raman data for the hydrous $Na_2Si_2O_5$ glass thin sections.

3.1.4. Spectroscopic measurements *in situ* at high temperature

High-temperature spectroscopic measurements were performed in HDAC in the pressure range from 0.2 to 1.7 GPa using the synthesized ^{13}C diamond as a pressure sensor. A small piece of ^{13}C diamond aggregate (20-40

μm in size) was loaded into the 400 μm hole of 250 µm thick Ir gasket together with a piece of hydrous $Na_2Si_2O_5$ glass thin section, polished down to 150-200 µm and roughly shaped to fit into the gasket hole. This glass piece served both as a sample and as a pressure medium during experiment. No additional pressure medium was used in order to prevent any escape or uptake of water from/to the sample. Background NIR spectrum of the empty diamond anvil cell was recorded prior to each high-temperature experiment. The opening of 60° at the top and bottom of diamond anvil cell provided an optical access to the sample chamber by IRT-7000 microscope either with the 0.45N.A. Cassegrain optics for NIR spectroscopy or the 0.35N.A. objective for Raman spectroscopy.

At the beginning of each experiment the sample was pressurized by driving the screws along the guide posts of HDAC (the screw head rotation was 70° to 100°), then the sample was heated to 900 °C at a rate of 1 °C/sec. Spectroscopic measurements were carried out at 900 °C, then at 850 °C and 800 °C upon cooling. Temperature was monitored by alumel-chromel thermocouples attached to near the culet surfaces of the upper and lower diamond anvils. Pressure was determined from the Raman shift of ^{13}C diamond pressure sensor using the calibration of Schiferl et al. (1997). The ^{13}C diamond spectra were corrected to the Ne 585 nm line measured simultaneously, which yielded the reproducibility of ±0.5 cm^{-1} for the Raman shift measurements. During experiments, typically, a NIR spectrum of the sample was collected immediately after the HDAC reached desired temperature (pressure), and then Raman spectra of the sample and the ^{13}C diamond pressure sensor were acquired. In several experiments, another NIR spectrum was collected for the melt after the Raman measurements. No

detectable change of the NIR spectra was observed between the two measurements, implying a fast equilibration for the water species at high temperatures.

After measurements the melt was quenched to glass by shutting off the electric power supply and the run product was checked by NIR spectroscopy for the possible loss of water during the experiments. Though the quenching from low pressures was accompanied by the exsolution of bubbles (several micrometers in size), spectra of the quenched products were similar to those of the starting glasses (Figure 3-5). Total water contents calculated for the quenched products using molar absorption coefficients (Yamashita et al., 2008) are all consistent with total water contents of the starting glasses within analytical uncertainty (Table 3-5).
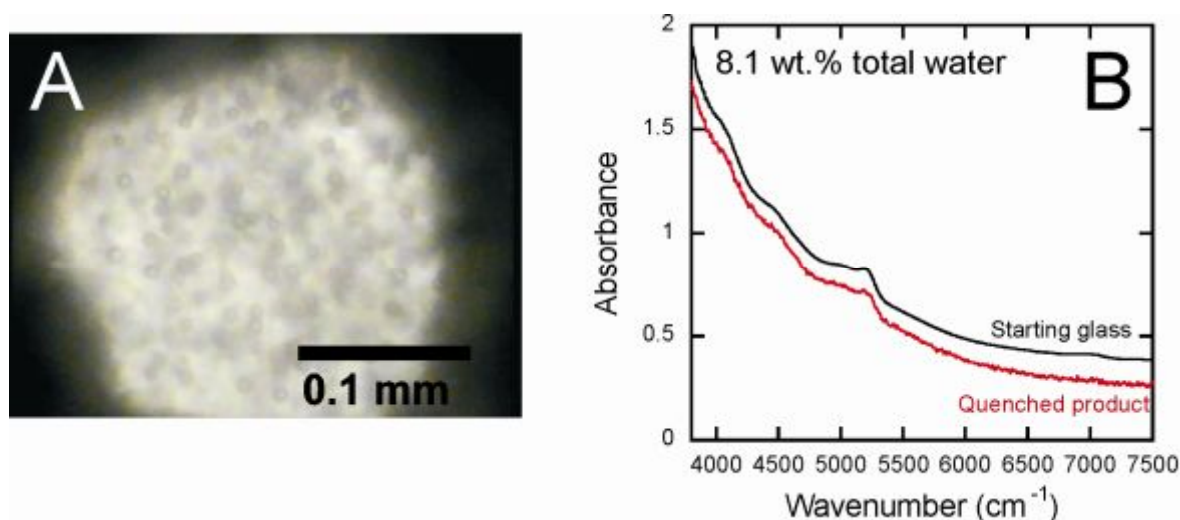

Figure 3-5. A photograph (a) and NIR spectrum (b, indicated by the red color) of the bubble-containing glass quenched from 900 °C and 0.3 GPa (run #15 in Table 3-5). NIR spectrum of the starting glass thin section (b, indicated by the black color) is shown for comparison.

The gasket thickness in the vicinity of sample hole was measured after experiment with a Mitutoyo displacement gauge (Figure 3-6), assuming that deformation of the gasket upon cooling and quenching was negligible and its thickness represents the sample thickness at 900-800 °C.
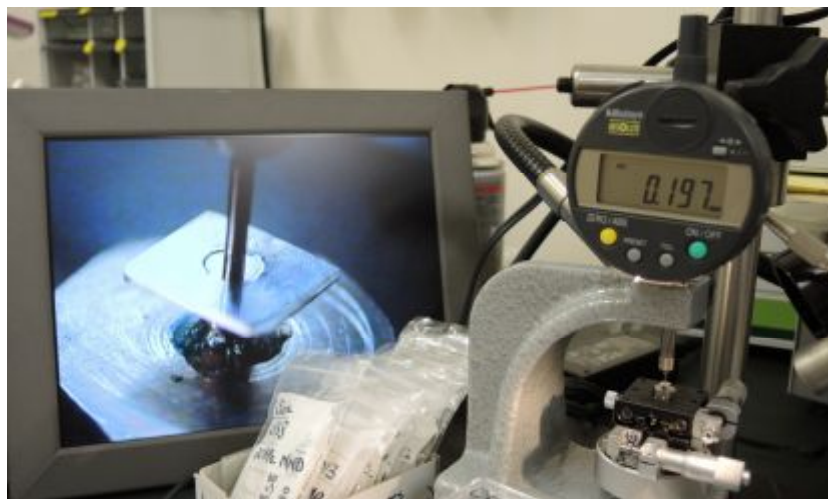

Figure 3-6. Determination of gasket thickness after experiment (run #13) with the Mitutoyo displacement gauge.

3.2. Results and discussion

Photomicrographs of the phases observed during high-temperature experiments in HDAC are shown for the runs with 4.2, 6.2 and 8.1 wt.% total water in Figures 3-6, 3-7, 3-8. At the beginning of these runs, upon heating, a separation of fluid started at 335, 278 and 230 °C respectively, then a transformation of the glass to $Na_2Si_2O_5$ crystals took place at about 570, 415 and 340 °C in each of these runs. A coexistence of crystals, melt and fluid

was observed in the temperature intervals 743-802 °C, 629-706 °C and 575-681 °C respectively. At higher temperatures the crystals were completely melted. Spectroscopic measurements of a melt phase were carried out after complete dissolution of fluid into the melt (Figures 3-7, 3-8, 3-9) at 900 °C. The same phase appearance was observed in other runs, with the change of phase transition temperatures depending on the total water content and experimental pressure. In the runs #9, #12 and #27 (Table 3-5) NIR spectra of the homogeneous melt phase were additionally collected on cooling path at 850 °C and 800 °C (photos of the melt phase at these temperatures are shown for the run #12 in Figure 3-7).
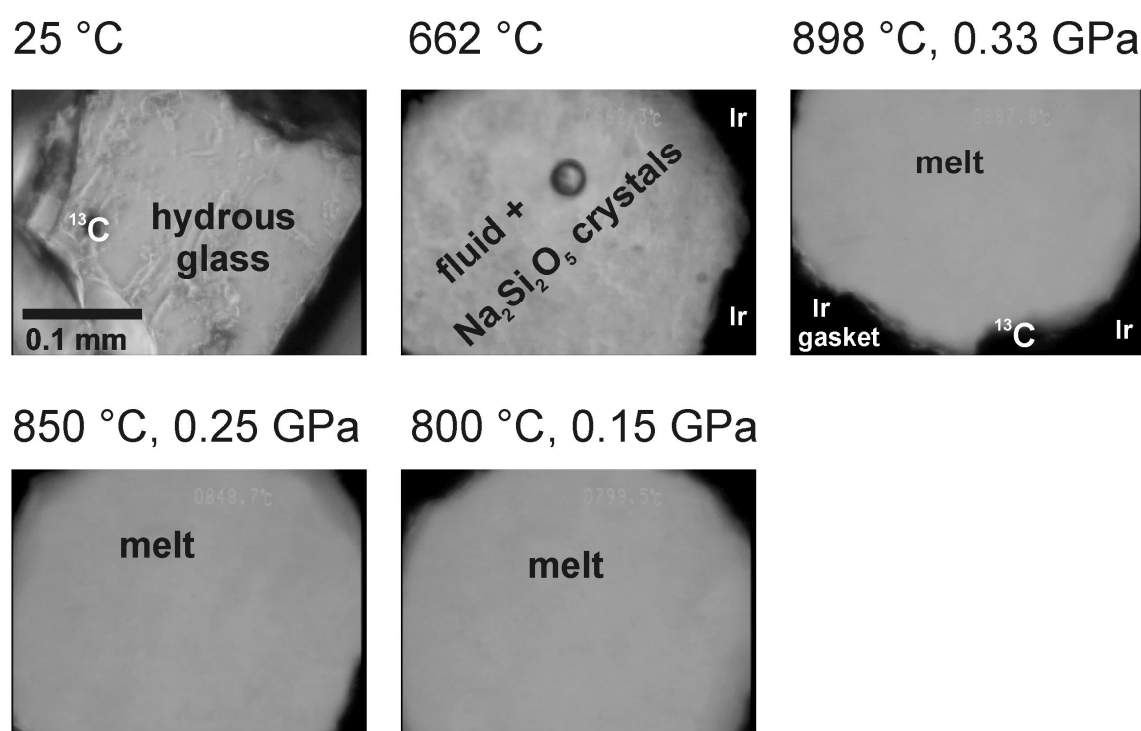

Figure 3-7. Photomicrographs taken in the HDAC experiment with 4.2 wt.% total water (run #12 in Table 3-5). The scale is the same for all the photomicrographs. Pressure was calculated using the Raman shift of ^{13}C diamond pressure sensor.
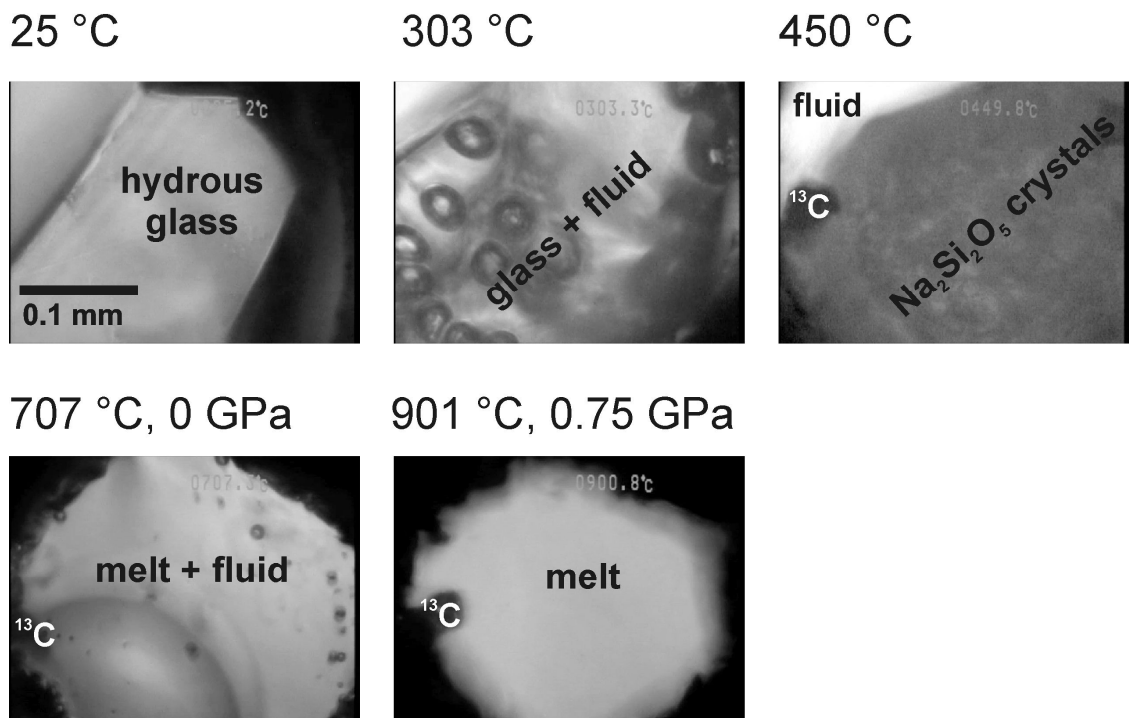
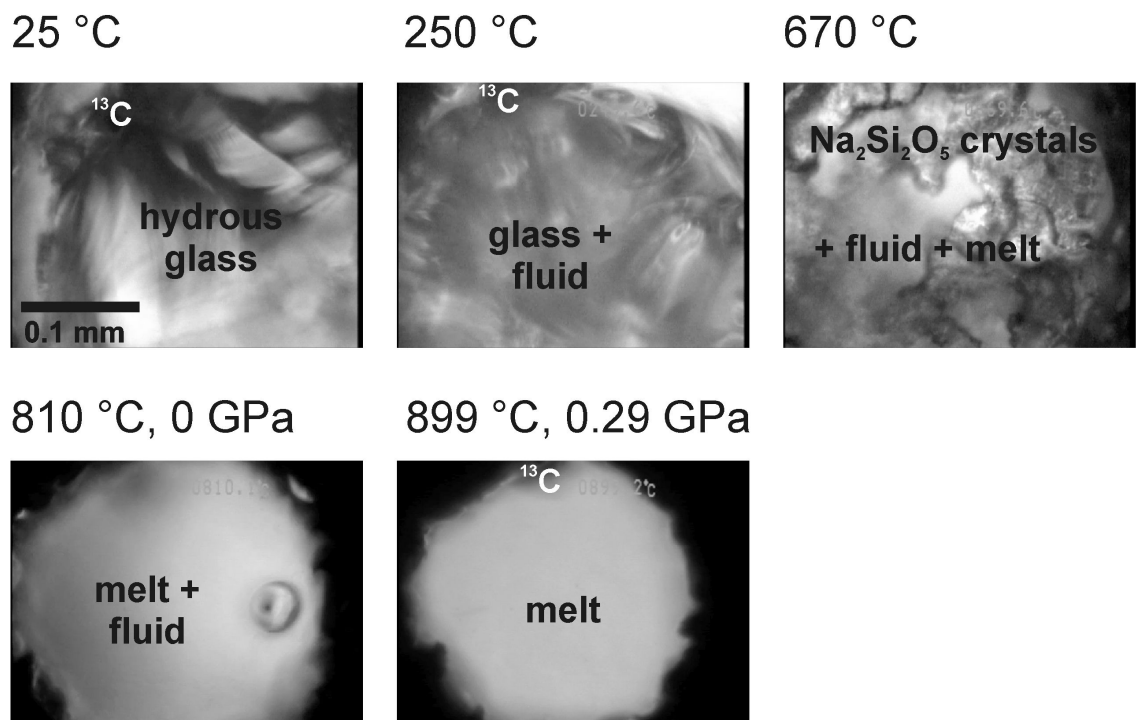**Figure 3-8.** Phases observed in the HDAC experiment with 6.2 wt.% total water (run #20).


**Figure 3-9.** Phases observed in the HDAC experiment with 8.1 wt.% total water (run #14).

3.2.1. NIR spectra of hydrous $Na_2Si_2O_5$ melts

NIR spectra of the homogeneous hydrous melts collected at 900 °C and four pressure intervals (0.2-0.5 GPa (a); 0.8-0.9 GPa (b); 1.1 GPa (c); 1.5-1.7 GPa (d)) are summarized in Figure 3-10, NIR spectra collected at 850 °C and 800 °C are shown in Figure 3-11. The spectra were corrected for the baseline using the same method as described in Section 3.1.2. for the room temperature spectra.

Figure 3-10. Representative NIR absorption spectra of hydrous $Na_2Si_2O_5$ melts collected at 900 °C and four pressure intervals: (a) 0.2-0.5 GPa, (b) 0.8-0.9 GPa, (c) 1.1 and (d) 1.5-1.7 GPa. The baseline is illustrated by the grey curves and the baseline-corrected spectra are shown on right hand side. All spectra are scaled to a thickness of 500 μm.

(a) 900°C, 0.2-0.5GPa

(b) 900°C, 0.8-0.9GPa

(c) 900°C, 1.1GPa

(d) 900°C, 1.5-1.7GPa
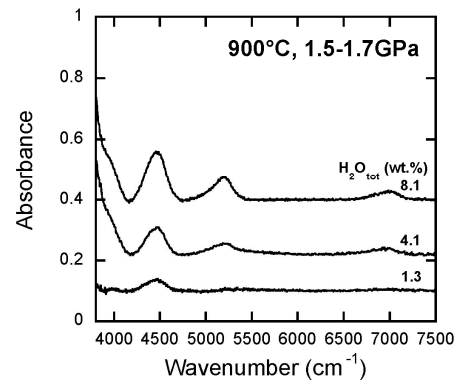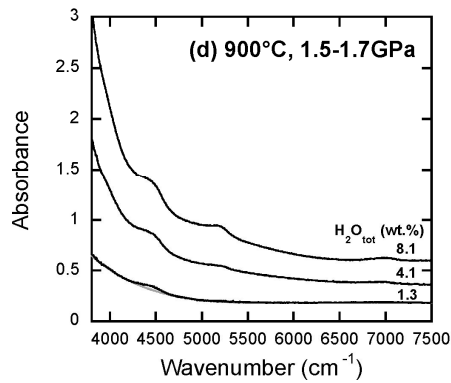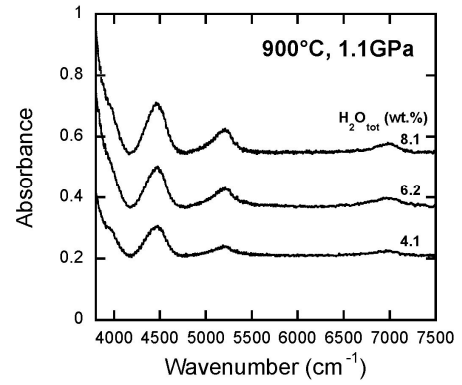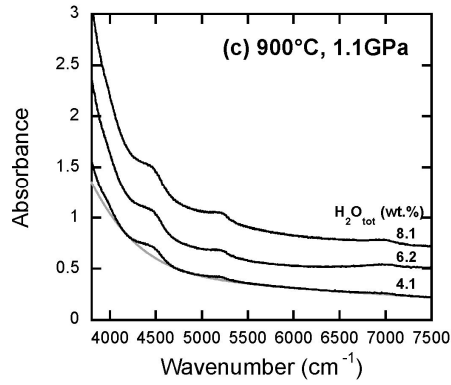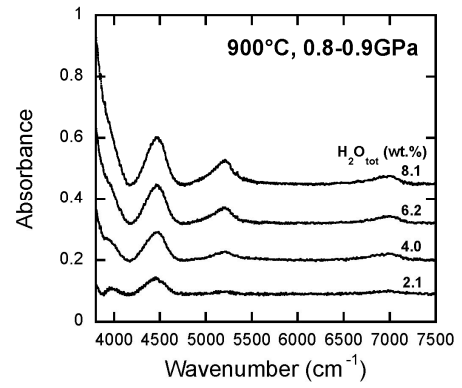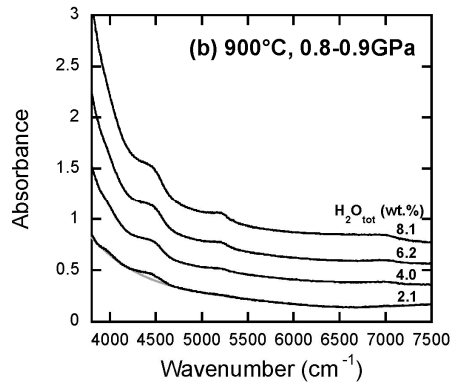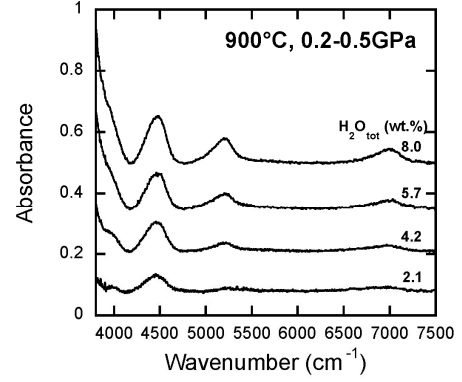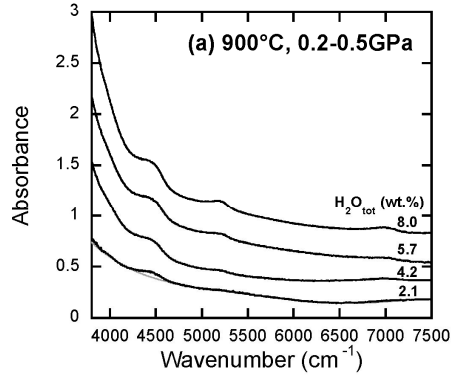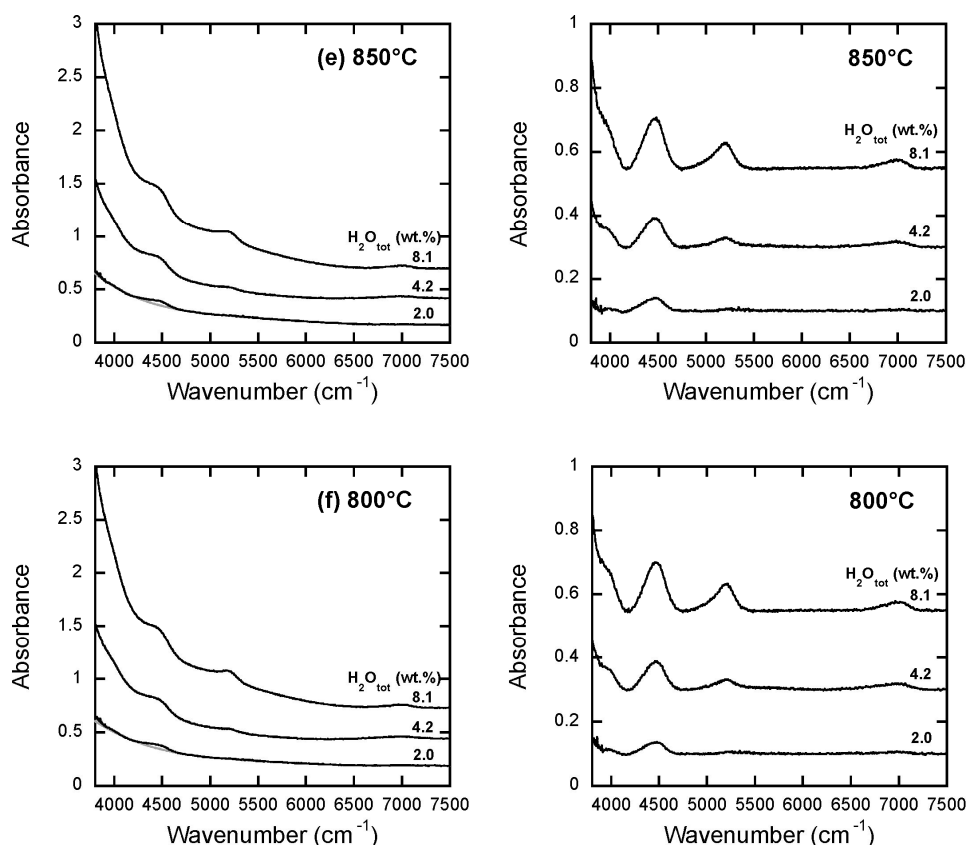
Figure 3-11. NIR absorption spectra of hydrous $Na_2Si_2O_5$ melts collected at 850 °C and 800 °C (scaled to a thickness of 500 μm).

Spectroscopic features changed significantly from the room temperature glasses to the high-temperature melts (Figure 3-12). At 900 °C, intensity of the 4500 cm^{-1} OH band increased by several times at the expense of the 5200 cm^{-1} molecular H_2O band. The 4500 cm^{-1} OH groups band was fitted by a single Gaussian and no significant change of the shape was found upon heating. Change in the shape of the 5200 cm^{-1} molecular H_2O band can be monitored by fitting three Gaussian sub-bands, one centered at about 5100 cm^{-1}, one centered at about 5200 cm^{-1}, and one centered at about 5500 cm^{-1}. In comparison with room temperature spectra, at 900 °C peak height of the 5100

cm^{-1} sub-band decreased to about one third and peak height of the 5500 cm^{-1} sun-band decreased to about a half. As a result of these changes, the overall shape of the 5200 cm^{-1} molecular H_2O band became more symmetrical (Figure 3-12).

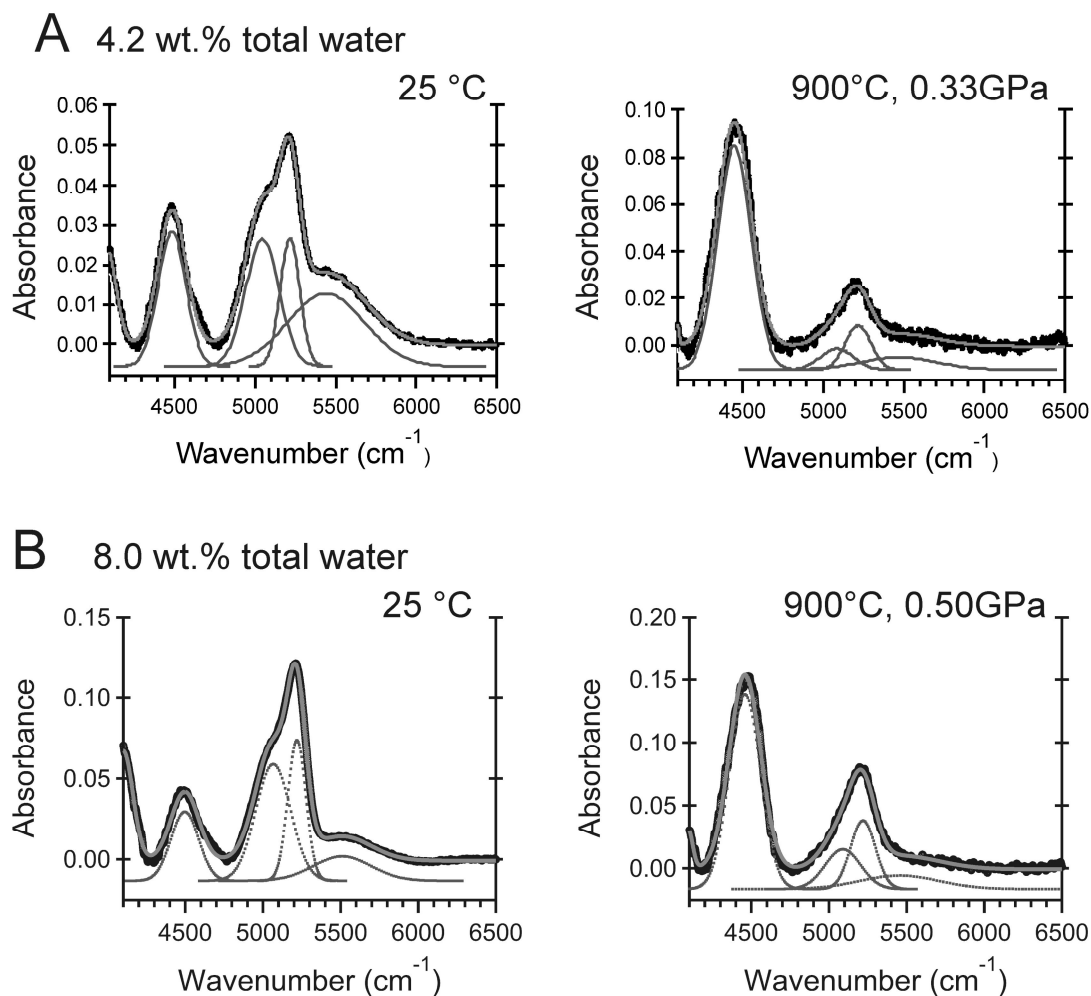**Figure 3-12.** Comparison of NIR absorption spectra between the starting glasses (left hand side) and the melts at 900 °C (right hand side) for the samples containing: (a) 4.2 wt.% total water, (b) 8.0 wt.% total water. The OH group band at ~4500 cm^{-1} is fitted with a single Gaussian peak and the molecular H_2O band at ~5200 cm^{-1} with the three Gaussian sub-components.

Both at room temperature and at 900 °C, peak height of the 5100 cm^{-1} sub-band is proportional to that of the 5200 cm^{-1} sub-band, but the peak height of the 5500 cm^{-1} sub-band is not (Figure 3-13), consistent with the previous band assignment by Yamashita et al. (2008) for hydrous $Na_2Si_2O_5$ glasses. Obviously, the 5500 cm^{-1} sub-band is not attributed to the combination mode of the fundamental stretching and bending of H_2O molecules. Similarly to the procedure for room temperature glasses, this sub-band component was subtracted from the overall intensity of the 5200 cm^{-1} molecular H_2O band in the quantitative analysis of molecular H_2O species. For the water-poor sodium disilicate melts (1.3-2.1 wt.% total water) at 800-900 °C, the 5200 cm^{-1} molecular H_2O band was approximated by a single Gaussian curve, but this approximation does not affect quantitative results since the band intensity at low water content is comparable to the analytical uncertainty (Table 3-5).
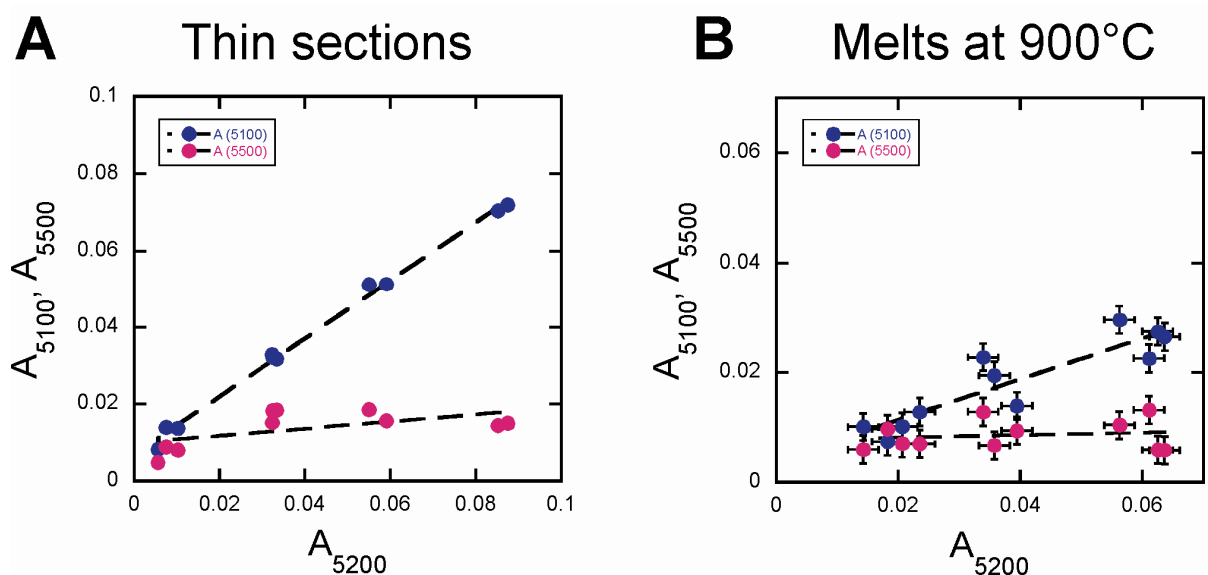
Figure 3-13. Correlation between the NIR peak heights of the sub-bands centered at about

5100 cm^{-1} and 5500 cm^{-1} to the sub-band centered at about 5200 cm^{-1}. (a) Starting glass thin sections at room temperature; (b) melts at 900 °C. The peak heights are normalized to a thickness of 500 μm.

A slight change of NIR spectra was observed upon cooling from 900 °C to 800 °C, with the decrease in peak height of the 4500 cm^{-1} OH groups band and the increase in peak height of the 5200 cm^{-1} molecular H_2O band (Figure 3-14). No systematic change of the 4500 cm^{-1} and 5200 cm^{-1} band intensities with pressure was detected.
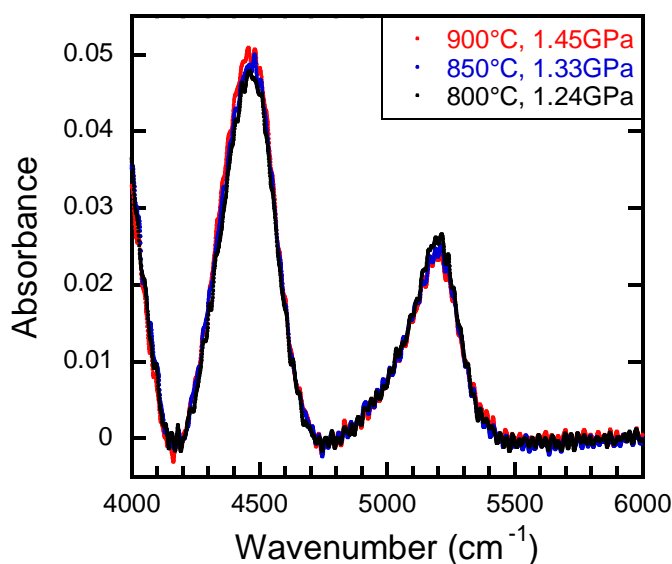
Figure 3-14. The change of 4500 cm^{-1} and 5200 cm^{-1} bands intensities with temperature for the run #27 with 8.1 wt.% total water. NIR spectra are scaled to 0.158 mm gasket thickness.

3.2.2. Calibration of molar absorption coefficients

Concentrations of OH groups and molecular H_2O in the melt at 900 °C, 850 °C and 800 °C were calculated using Beer-Lambert law:

$$C_{\text{OH}} = \frac{1802 \cdot A_{4500}}{d \cdot \rho \cdot \varepsilon_{4500}} \quad , \tag{3-3}$$

$$C_{\text{H}_2\text{O}_\text{m}} = \frac{1802 \cdot A_{5200}}{d \cdot \rho \cdot \varepsilon_{5200}} \quad , \tag{3-4}$$

where C_{OH} and C_{H2Om} denote the concentrations (in wt.%) of water dissolved as OH groups (18.02 molecular mass basis) and molecular H_2O, respectively, A_{4500} and A_{5200} are the absorbances (peak heights) of respective bands, ε_{4500} and ε_{5200} are the corresponding molar absorption coefficients at temperature and pressure of measurement (l mol^{-1} cm^{-1}), d is sample thickness (cm), ρ is its density (g l^{-1}). The model of Ochs and Lange (1997) was applied for the calculation of melts density. The ε_{4500} and ε_{5200} values were calibrated for the each pressure interval using the expression:

$$\left[\frac{1802 \cdot A_{5200}}{d \cdot \rho \cdot C_{\text{H}_2\text{O}_\text{t}}} \right] = \varepsilon_{5200} - \frac{\varepsilon_{5200}}{\varepsilon_{4500}} \left[\frac{1802 \cdot A_{4500}}{d \cdot \rho \cdot C_{\text{H}_2\text{O}_\text{t}}} \right] , \tag{3-5}$$

which is a combination of the equations (3-3) and (3-4) under the assumption that total water content C_{H2Ot} is a sum of OH groups and molecular H_2O species.
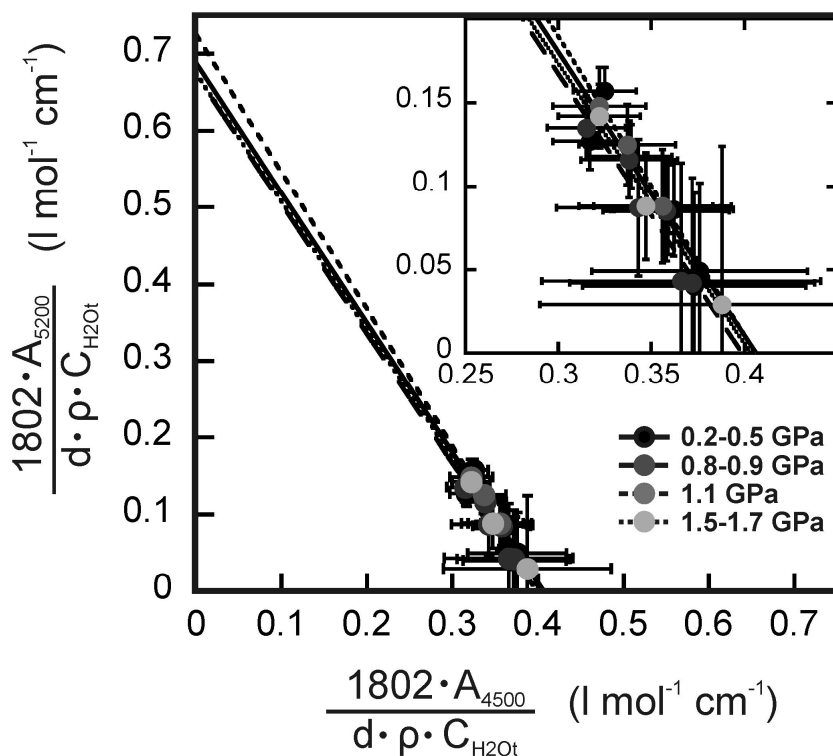
Figure 3-15. Calibration plot for the determination of linear molar absorption coefficients for the 4500 cm^{-1} and 5200 cm^{-1} NIR bands of water species in the sodium disilicate melt at 900 °C and four pressure intervals. Inset gives a closer view. Molar absorption coefficients were found as the intercepts of each isobaric line with the corresponding axis using a linear regression. Error bars indicate propagation of the uncertainties in peak intensity, sample thickness, density and total water content.

It can be seen in the calibration plot that all experimental points at 900 °C fall close to the straight lines (Figure 3-15), and a unique pair of the linear molar absorption coefficients ε_{4500} and ε_{5200} can be found for the each pressure interval (Table 3-5). Basic assumption in this calibration is that the peak heights of the OH groups at 4500 cm^{-1} and the molecular H_2O at 5200 cm^{-1} represent all water species dissolved in the melt. Successful fitting of the linear ε_{4500} and ε_{5200} appears to be a validation of this assumption. [1]H and [29]Si

64

NMR study by Xue and Kanzaki (2004) is also consistent with this assumption, as it has shown that SiOH groups and molecular H_2O are the dominant water species in the quenched sodium disilicate glasses. Previous NIR and low temperature static ^{1}H NMR studies of depolymerized silicate glasses showed that the ε values have weak dependence on total water content, which is presumably attributed to the fractional change of the water subspecies strongly hydrogen-bonded to non-bridging oxygens (Stuke et al., 2006; Yamahista et al., 2008). According to Yamashita et al. (2008), the variations of ε_{4500} and ε_{5200} values in the sodium disilicate glasses at room temperature are $\pm 14\%$ and $\pm 6\%$ respectively in the range of total water contents considered in this study. These variations are comparable to the uncertainties in our calibration itself. Even weaker dependence of molar absorption coefficients on total water content is expected at high temperatures due to the decrease of hydrogen bond strength with temperature (Behrens and Schmidt, 1998). Linear molar absorption coefficients ε_{4500} and ε_{5200} are therefore a suitable choice for the evaluation of water species abundances in sodium disilicate melt at 800-900 °C.
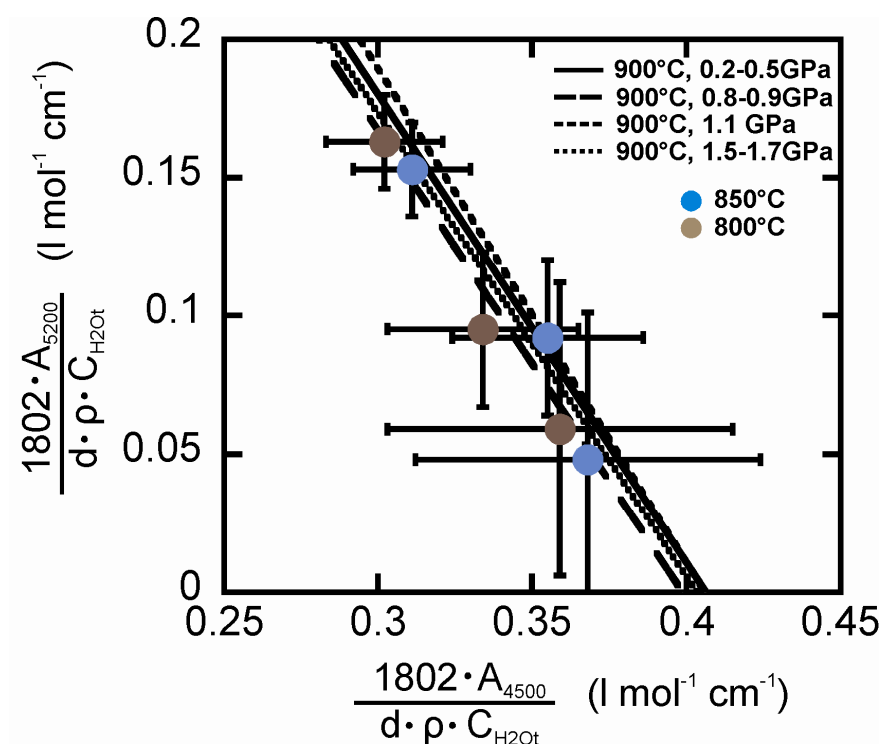
Figure 3-16. Calibration plot for the determination of linear molar absorption coefficients at 850 °C and 800 °C.

Experimental data points of 850 °C and 800 °C fall on the calibration lines plotted for 900 °C (Figure 3-16). Since ε_{4500} and ε_{5200} values for 900 °C are the same between the pressure intervals within the estimated uncertainties (Table 3-5), molar absorption coefficients for 850 °C and 800 °C were calculated as the average values of ε_{4500} and ε_{5200} obtained at 900 °C within the 0.2-1.7 GPa pressure range.

	Total water content[a] (wt.%)	Pressure[b] (GPa)	Density[c] (g l^{-1})	Thickness (cm)	A_{4500}	A_{5200}	ε_{4500} (l mol^{-1}cm^{-1})	ε_{5200} (l mol^{-1}cm^{-1})	C_{OH}[d] (wt.%)	C_{H2Om}[d] (wt.%)	K_1[d]	Water content (wt.%) after experiment
900°C, 0.2-0.5GPa:												
Run #9	1.97 (0.10)	0.18	2256 (11)	0.0192	0.0178	0.0023	0.41 (0.09)	0.69 (0.10)	1.81 (0.48)	0.14 (0.15)	2.01 (2.39)	2.29 (1.12)
Run #10	2.09 (0.12)	0.52	2296 (11)	0.0167	0.0166	0.0018	0.41 (0.09)	0.69 (0.10)	1.90 (0.52)	0.12 (0.17)	2.58 (3.92)	2.31 (0.64)
Run #11	4.12 (0.18)	0.27	2187 (11)	0.019	0.0341	0.0082	0.41 (0.09)	0.69 (0.10)	3.61 (0.86)	0.52 (0.17)	2.29 (1.21)	4.59 (0.98)
Run #12	4.19 (0.16)	0.33	2193 (11)	0.0178	0.0329	0.0078	0.41 (0.09)	0.69 (0.10)	3.70 (0.89)	0.52 (0.18)	2.41 (1.31)	4.36 (0.52)
Run #13	5.69 (0.19)	0.43	2156 (11)	0.0197	0.0455	0.0158	0.41 (0.09)	0.69 (0.10)	4.71 (1.10)	0.97 (0.21)	2.18 (0.99)	5.52 (0.88)
Run #14	8.07 (0.25)	0.29	2056 (10)	0.0163	0.0476	0.0191	0.41 (0.09)	0.69 (0.10)	6.24 (1.45)	1.49 (0.30)	2.65 (1.18)	7.38 (1.04)
Run #15	8.03 (0.25)	0.50	2091 (10)	0.0200	0.0606	0.0293	0.41 (0.09)	0.69 (0.10)	6.37 (1.47)	1.83 (0.31)	2.27 (0.99)	8.12 (0.92)
900°C, 0.8-0.9GPa:												
Run #16	2.09 (0.12)	0.83	2339 (12)	0.0155	0.0154	0.0018	0.40 (0.09)	0.67 (0.10)	1.91 (0.53)	0.13 (0.19)	2.41 (3.56)	2.02 (0.32)
Run #17	2.09 (0.12)	0.86	2343 (12)	0.0176	0.0178	0.0020	0.40 (0.09)	0.67 (0.10)	1.94 (0.52)	0.13 (0.16)	2.49 (3.42)	2.08 (0.30)
Run #18	4.04 (0.22)	0.78	2264 (11)	0.0199	0.0362	0.0086	0.40 (0.09)	0.67 (0.10)	3.62 (0.86)	0.51 (0.17)	2.35 (1.22)	3.86 (0.62)
Run #19	4.14 (0.18)[e]	0.90	2279 (11)	0.0141	0.0253	0.0064	0.40 (0.09)	0.67 (0.10)	3.55 (0.88)	0.54 (0.22)	2.13 (1.30)	4.39 (0.91)
Run #20	6.15 (0.21)	0.75	2190 (11)	0.0178	0.0450	0.0154	0.40 (0.09)	0.67 (0.10)	5.20 (1.21)	1.06 (0.23)	2.48 (1.13)	6.16 (0.79)
Run #21	8.07 (0.25)	0.94	2163 (11)	0.0172	0.0525	0.0225	0.40 (0.09)	0.67 (0.010)	6.36 (1.47)	1.63 (0.30)	2.54 (1.12)	8.24 (0.75)
900°C, 1.1GPa:												
Run #22	4.14 (0.18)[e]	1.08	2307 (12)	0.0170	0.0321	0.0079	0.41 (0.04)	0.72 (0.04)	3.60 (0.45)	0.50 (0.16)	2.37 (0.96)	4.46 (0.49)
Run #23	6.15 (0.21)	1.09	2246 (11)	0.0167	0.0432	0.0160	0.41 (0.04)	0.72 (0.04)	5.06 (0.58)	1.07 (0.18)	2.31 (0.63)	6.39 (0.55)
Run #24	8.07 (0.25)	1.08	2187 (11)	0.0135	0.0426	0.0196	0.41 (0.04)	0.72 (0.04)	6.34 (0.73)	1.66 (0.24)	2.47 (0.65)	7.92 (0.39)
900°C, 1.5-1.7GPa:												
Run #25	1.34 (0.08)	1.49	2458 (12)	0.0172	0.0122	0.0009	0.40 (0.06)	0.68 (0.06)	1.30 (0.33)	0.06 (0.16)	2.37 (6.33)	1.46 (0.28)
Run #26	4.12 (0.18)	1.71	2410 (12)	0.0169	0.0323	0.0082	0.40 (0.06)	0.68 (0.06)	3.57 (0.58)	0.53 (0.17)	2.19 (0.96)	4.31 (0.33)
Run #27	8.07 (0.25)	1.45	2255 (11)	0.0158	0.0513	0.0226	0.40 (0.06)	0.68 (0.06)	6.49 (0.99)	1.68 (0.24)	2.58 (0.78)	8.01 (0.40)

850 °C:												
Run #9	1.97 (0.10)	0.15	2265 (11)	0.0192	0.0175	0.0023	0.405 (0.120)	0.685 (0.132)	1.79 (0.59)	0.14 (0.15)	1.96 (2.44)	2.29 (1.12)
Run #12	4.19 (0.16)	0.25	2196 (11)	0.0178	0.0323	0.0084	0.405 (0.120)	0.685 (0.132)	3.68 (1.13)	0.57 (0.20)	2.18 (1.36)	4.36 (0.52)
Run #27	8.07 (0.25)	1.33	2247 (11)	0.0158	0.0494	0.0243	0.405 (0.120)	0.685 (0.132)	6.19 (1.86)	1.80 (0.39)	2.17 (1.22)	8.01 (0.40)
800 °C:												
Run #9	1.97 (0.10)	0.09	2271 (11)	0.0192	0.0171	0.0028	0.405 (0.059)	0.685 (0.063)	1.74 (0.36)	0.17 (0.15)	1.52 (1.49)	2.29 (1.12)
Run #12	4.19 (0.16)	0.15	2198 (11)	0.0178	0.0304	0.0086	0.405 (0.059)	0.685 (0.063)	3.46 (0.58)	0.58 (0.18)	1.88 (0.80)	4.36 (0.52)
Run #27	8.07 (0.25)	1.24	2246 (11)	0.0158	0.048	0.0259	0.405 (0.059)	0.685 (0.063)	6.02 (0.93)	1.92 (0.26)	1.91 (0.59)	8.01 (0.40)

[a] Total water content was determined by NIR spectroscopy at room temperature.

[b] Pressure calculated based on Raman shift of ^{13}C diamond (Schiferl et al., 1997).

[c] Density calculated with the model of Ochs and Lange (1997).

[d] Concentrations of OH groups and molecular H_2O calculated with Eq. (3-3) and (3-4) respectively; equilibrium constant K_1 calculated with Eq. (3-6).

[e] Total water content of this starting glass was taken as an average value among the glass pieces from the 4 wt.% IHPV synthesis.

Estimated uncertainty for thickness ±0.0002 cm, for peak heights ±0.0025.

Table 3-5. Result of *in situ* NIR measurements of hydrous $Na_2Si_2O_5$ melts at 900 °C, 850°C and 800 °C.

3.2.3. Evaluation of Raman spectra of hydrous Na₂Si₂O₅ melts

Raman spectra of the $Na_2Si_2O_5$ melts recorded at 900 °C and 0-0.5 GPa (a), 0.8-0.9 GPa (b), 1.5-1.7 GPa (c) are shown in Figure 3-17 on left hand side, baseline and temperature-frequency corrected spectra are shown on right hand side.
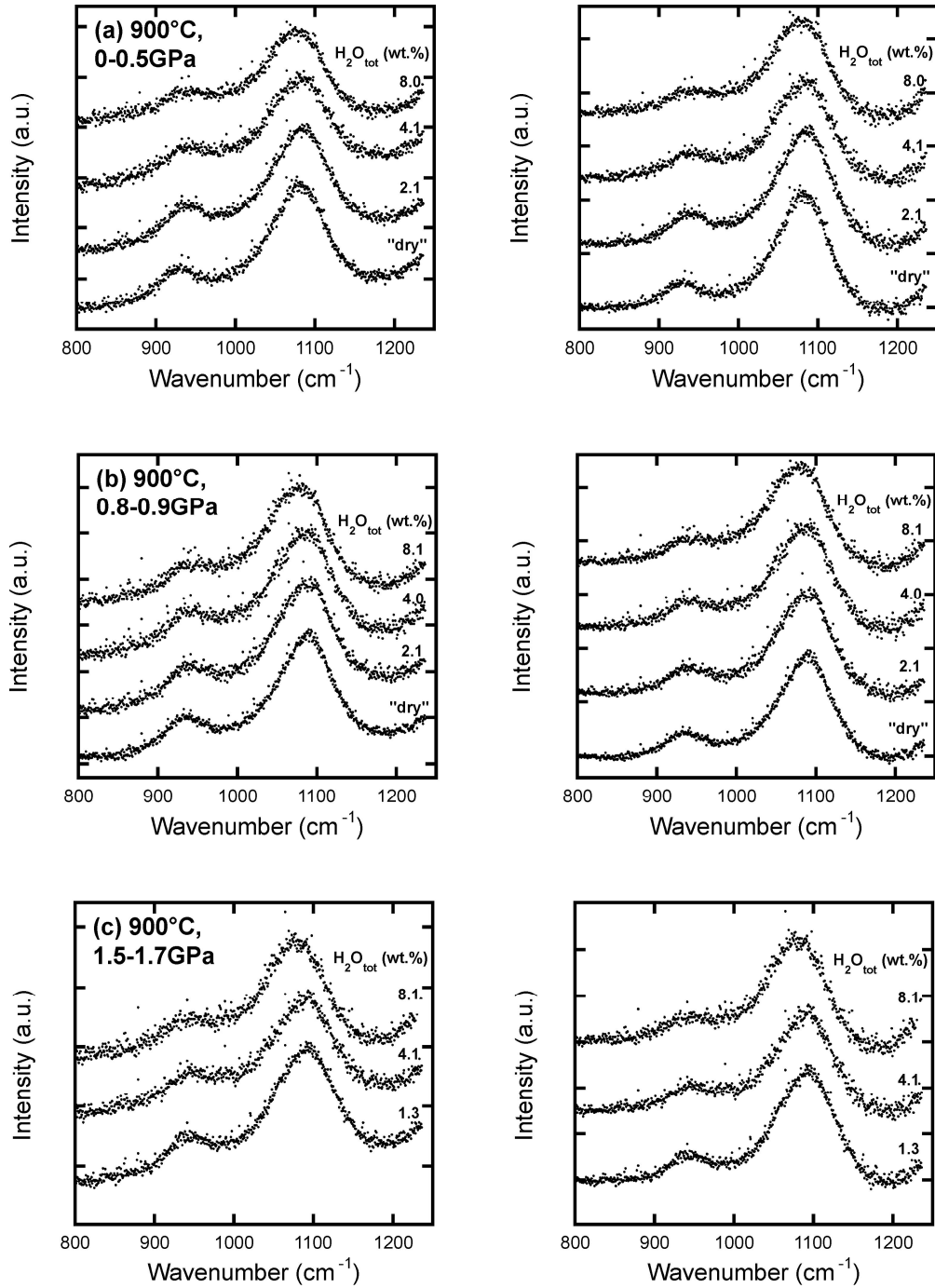
Figure 3-17. Raman spectra of the $Na_2Si_2O_5$ melts collected at 900 °C and three pressure intervals: (a) 0-0.5 GPa, (b) 0.8-0.9 GPa and (c) 1.5-1.7 GPa. All spectra are normalized to the sum of 950 cm^{-1} and 1100 cm^{-1} peaks integrated intensity ($I_{950} + I_{1100}$) of 400.

Intensities of the Raman peaks at 950 cm^{-1} and 1100 cm^{-1} were used for the evaluation of Q^2 and Q^3 species abundances, according to the assignment for the room temperature glasses (see Section 3.1.2.). It was difficult to make a quantitative analysis for the Raman peak at ~1150 cm^{-1}, assigned to the stretching vibrations of Q^4 species, due to the overlapping with the Raman peak from the upper diamond anvil, which extends to ~1150 cm^{-1} at its low frequency end (Figure 3-18). Since the integrated intensity of this peak is expected to be one order of magnitude smaller than the intensities of other Raman peaks arising from the vibrations of Q^n species (see the room temperature data shown in Table 3-4), its contribution to the intensity of Q^3 peak located at ~1100 cm^{-1} was assumed to be negligible.

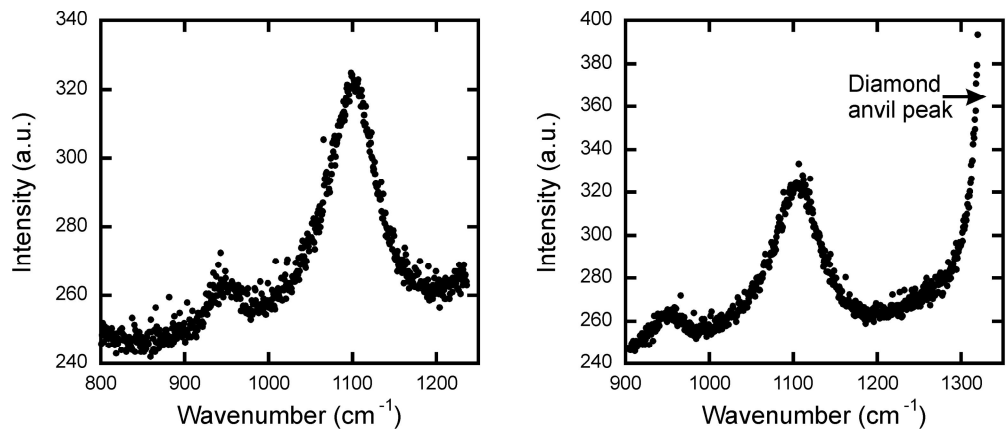**Figure 3-18.** Raman spectra of the dry $Na_2Si_2O_5$ starting glass placed inside HDAC. The spectrum on the right is shifted to the higher wavenumbers and shows a strong peak from the upper diamond anvil, which extends to ~1150 cm^{-1}.

Temperature-frequency corrected Raman spectra collected at 900 °C were fitted with the three Gaussian peaks (Figure 3-19).
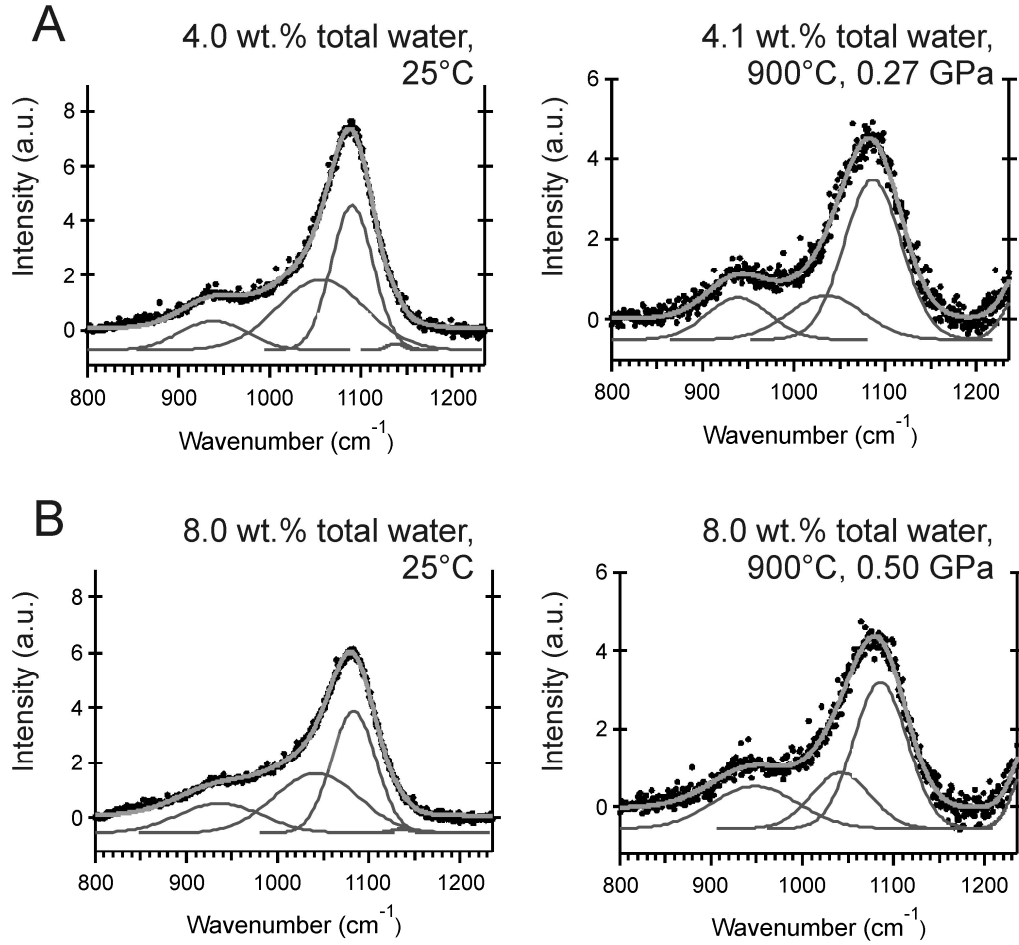

Figure 3-19. Deconvolution for the Raman spectra of room temperature glasses (left hand side, four Gaussian peaks fitting) and of the melts at 900 °C (right hand side, three Gaussian peaks fitting).

Procedure for the determination of Q^2 and Q^3 species abundances at 900 °C was similar to that applied to the room temperature glasses. First, concentrations of Q^2 and Q^3 species in the dry $Na_2Si_2O_5$ melt were calculated at 900 °C using the temperature dependence of Q^n speciation reported in (Malfait et al., 2008). Then, Raman scattering coefficients were determined at 900 °C as

$$C_i = \frac{X(Q^n)}{I_i} \cdot \left(I_{950} + I_{1100} \right), \tag{3-6}$$

where i denotes 950 cm^{-1} or 1100 cm^{-1} Raman peak, $X(Q^n)$ is the concentration of Q^2 or Q^3 species respectively in the dry Na$_2$Si$_2$O$_5$ melt and I is the integrated Raman intensity.

Q^2 and Q^3 speciation in the hydrous melts was calculated by the multiplication of the obtained Raman scattering coefficients and the integrated intensities of the respective Raman peaks in the spectra of hydrous melts. Here again I assume that Raman scattering coefficients do not depend on total water content at least to 8.1 wt.%. Results of the calculation are shown in Table 3-6. Since Q^4 species were not taken into account in this calculation, the sum Q^2+Q^3 is systematically lower than 100%.

	Total w.c. (wt.%)	Pressure (GPa)	I_{950}	I_{1100}	Q^2 (mol.%)	Q^3 (mol.%)	Q^2+Q^3
(*Malfait et al.,2008*)	"dry"	0			13.8 (1.3)	72.3 (2.6)	86.1 (2.9)
Run #28	"dry"	0	0.171 (0.008)	0.829 (0.027)			
		C_i	80.7 (8.5)	87.2 (4.2)			
Run #29	"dry"	0.76	0.170 (0.008)	0.830 (0.009)	13.7 (1.6)	72.4 (3.6)	86.1 (3.9)
Run #25	1.34 (0.08)	1.49	0.176 (0.017)	0.824 (0.082)	14.2 (2.0)	71.8 (8.0)	86.0 (8.2)
Run #10	2.09 (0.12)	0.52	0.192 (0.009)	0.808 (0.017)	15.5 (1.8)	70.5 (3.7)	86.0 (4.1)
Run #17	2.09 (0.12)	0.86	0.196 (0.014)	0.804 (0.023)	15.8 (2.0)	70.1 (3.9)	85.9 (4.4)
Run #11	4.12 (0.18)	0.27	0.220 (0.059)	0.780 (0.169)	17.8 (5.1)	68.0 (15.1)	85.8 (15.9)
Run #18	4.04 (0.22)	0.78	0.235 (0.028)	0.765 (0.090)	18.9 (3.0)	66.7 (8.5)	85.6 (9.0)
Run #26	4.12 (0.18)	1.71	0.231 (0.022)	0.769 (0.032)	18.6 (2.6)	67.1 (4.3)	85.7 (5.0)
Run #15	8.03 (0.25)	0.50	0.313 (0.028)	0.687 (0.129)	25.2 (3.5)	59.9 (11.6)	85.1 (12.1)
Run #21	8.07 (0.25)	0.94	0.308 (0.024)	0.692 (0.133)	24.9 (3.3)	60.3 (12.0)	85.2 (12.4)
Run #27	8.07 (0.25)	1.45	0.319 (0.097)	0.681 (0.235)	25.8 (8.3)	59.4 (20.7)	85.2 (22.3)

Table 3-6. Results of *in situ* Raman measurements and calculation of Q^2, Q^3 species abundances in the Na$_2$Si$_2$O$_5$ melts at 900 °C. Q^n species abundances in the dry Na$_2$Si$_2$O$_5$ melt at 900 °C were estimated from (Malfait et al., 2008).

As it can be seen from Table 3-6 and Figure 3-20, resulting Q^2 and Q^3 species concentrations at a fixed total water content do not depend on pressure. At the same time, a gradual increase of Q^2 species concentration from ~14 to ~25 mol.% and a decrease of Q^3 species concentration from ~72 to ~60 mol.% indicates a melt depolymerization with increasing total water content.
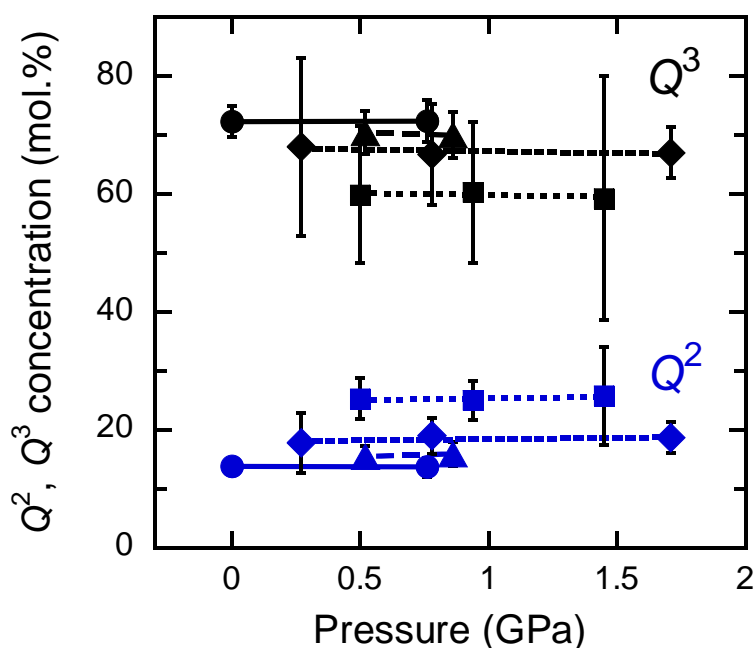

Figure 3-20. Concentrations of Q^2 and Q^3 species (in mol.%) in the $Na_2Si_2O_5$ melts at 900 °C as a function of pressure. Circles: "dry" $Na_2Si_2O_5$; triangulars: 2 wt.% total water; diamonds: 4 wt.%; squares: 8wt.%.

3.2.4. Pressure- and temperature-dependence of water speciation equilibrium

Resulting values of OH groups and molecular H_2O concentrations were used for the calculation of equilibrium constants for the speciation reaction (1-1) as

$$H_2O_m \text{ (melt)} + O \text{ (melt)} = 2OH \text{ (melt)} \tag{1-1}$$
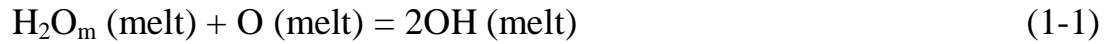
$$K_1 = \frac{(X_{OH})^2}{(X_{H2Om})(X_O)}, \tag{1-3}$$

$$X_O = 1 - X_{OH} - X_{H2Om}, $$

where X_i indicates mole fraction of the corresponding species in the melt on a single-oxygen basis (Stolper, 1982b). Results of the calculation are given in Table 3-5. The variation of equilibrium constant K_1 at the fixed temperature and pressure over the range of water contents studied is rather comparable to the uncertainty of calculation. This implies that hydrous sodium silicate melt can be treated as an ideal mixture of H_2O molecules, oxygens of the silicate melt framework and structurally bound OH groups. Also noteworthy is that K_1 values remain unchanged upon the increase of pressure from 0.2 to 1.7 GPa at 900 °C (Figure 3-21). These data are consistent with the pressure-independence of Q^2 and Q^3 speciation of the melt at a fixed total water content.
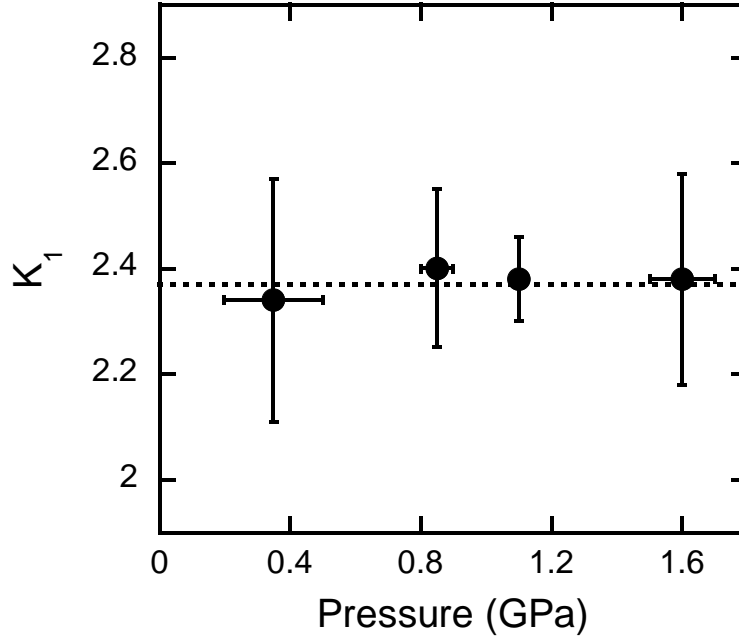
Figure 3-21. Pressure dependence of the equilibrium constant K_1 for the water speciation reaction at 900 °C. Dotted line indicates the average value of $K_1 = 2.37$. X error bars show pressure interval. Y error bars correspond to the standard deviation (1σ) of the data at each pressure interval.

When ideal mixing model is applied, the water speciation equilibrium (1-1) can be written as

$$- RT\ln K_1 = \Delta H^\circ - T\Delta S^\circ + \int_1^P \Delta V^\circ dP , \qquad (3\text{-}7)$$

where ΔH° is the standard enthalpy change, ΔS° is the standard entropy change, ΔV° is the standard volume change, R is the universal gas constant. The standard enthalpy change and standard entropy change are both assumed to be independent of temperature. In this case pressure dependence of the equilibrium (1-1) is expressed as

$$\left(\frac{\partial \ln K_1}{\partial P} \right)_T = -\frac{1}{RT}\Delta V^\circ , \qquad (3\text{-}8)$$

Since no effect of pressure on the equilibrium constants K_1 was observed in the present study (Figure 3-21), the standard volume change (ΔV°) of the water speciation reaction (1-1) is negligibly small in the hydrous sodium disilicate melts. This implies that partial molar volume of "water component" is independent of water speciation in the range of total water contents from 1.3 to 8.1 wt.%. Speciation-independent partial molar volume of water has been reported by previous authors for the more polymerized aluminosilicate melts (e.g., albitic melt: Ochs and Lange, 1997; andesitic melts: Richet and Polian, 1998). Negligible volume change of the water speciation reaction (1-1) is therefore universal over a range of melt compositions.

As the volume change of the water speciation reaction (1-1) is negligibly small below 1.7 GPa, Gibbs free energy of this reaction can be expressed through the standard enthalpy and entropy changes:

$$- RT\ln K_1 \approx \Delta H^\circ - T\Delta S^\circ. \tag{3-9}$$

An increase of temperature from 800 °C to 900 °C results in increase of K_1 from 1.78 to 2.37 (Figure 3-22). These data points can be fitted by a straight line in the $1000/T$–ln K_1 space (Figure 3-23) using the equation (3-9). The intercept ($\Delta S^\circ/R$) and the slope ($-\Delta H^\circ/R$) of the fitted line $\ln K_1 = \Delta S^\circ/R - (\Delta H^\circ/R)(1000/T)$ can be uniquely defined. Multiplication by the universal gas constant R = 8.314 J mol^{-1} K^{-1} gives the standard enthalpy change (ΔH°) of the water speciation equilibrium in the sodium disilicate melt of 30.7±2.4 kJ mol^{-1} and the standard entropy change (ΔS°) of 33.4±2.2 J mol^{-1} K^{-1}.
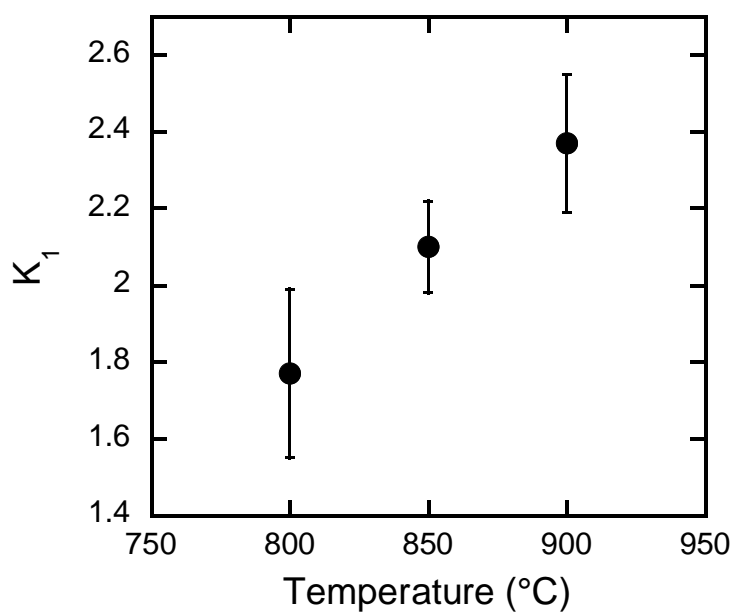
Figure 3-22. Temperature dependence of the equilibrium constant K_1 for the water speciation reaction. Error bars correspond to the standard deviation (1σ) of K_1 at each temperature.
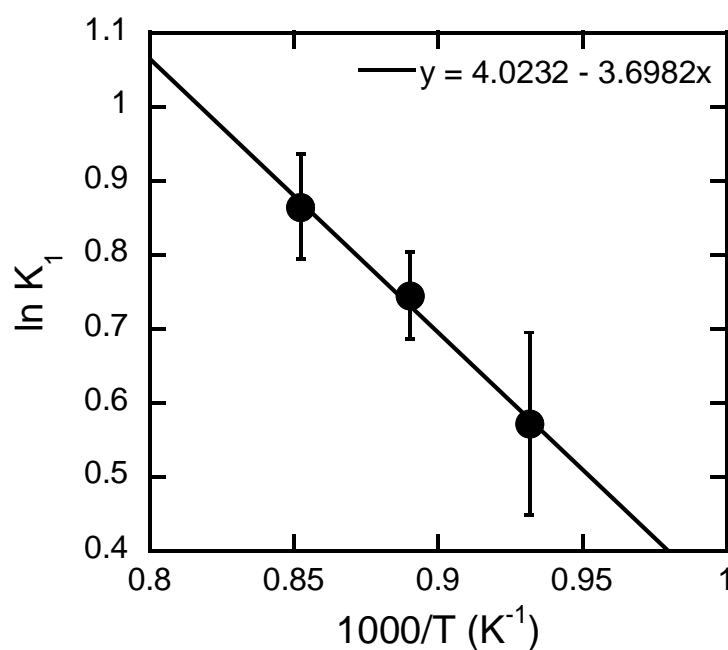

Figure 3-23. A plot for the determination of thermodynamic parameters (standard enthalpy $\Delta H°$ and entropy $\Delta S°$ change) for the water speciation equilibrium (1-1) in sodium disilicate melt. Error bars correspond to the standard deviation (1σ) of K_1 at each temperature.

3.2.5. The effect of composition on water speciation equilibrium

Results of this study are in agreement with the previous *in situ* NIR measurements on more polymerized melts: haplogranitic and rhyolitic melts (Nowak and Behrens, 1995, 2001; Shen and Keppler, 1995; Sowerby and Keppler, 1999), sodium tetra- and hexasilicate melts (Behrens and Yamashita, 2008). Significant increase of OH groups concentration at the expense of H_2O molecular species is a general trend observed for these compositions at high temperature. For the hydrous sodium disilicate melt, twice higher concentration of hydroxyl groups was found at 900 °C than that measured in the room temperature glass at 8.1 wt.% total water (Figure 3-24).
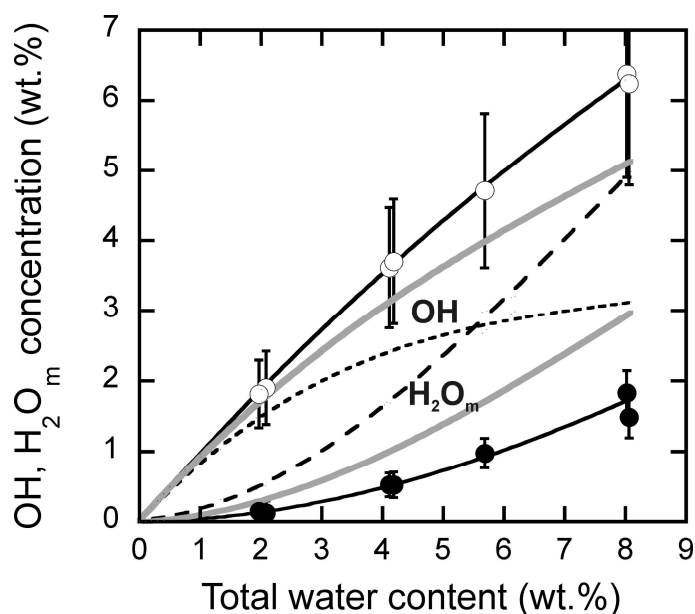
Figure 3-24. Concentrations of water species (open symbols OH groups, filled symbols H_2O molecules) in $Na_2Si_2O_5$ melt at 900 °C and 0.2-0.5 GPa as a function of total water content. Solid black lines calculated based on the average for all pressure intervals value of $K_1 = 2.37$ reproduce well the experimental points. Dotted lines indicate water speciation in the starting glasses. Solid grey lines, calculated at 900 °C based on Nowak and Behrens (2001) data for haplogranitic melt, are shown for comparison.

Equivalence of equilibrium constants K_1 for the reaction between molecular H_2O, oxygens of the silicate melt framework and OH groups in hydrous sodium disilicate melts in the range of water contents from 1.3 to 8.1 wt.% allows to model interaction between these species in terms of ideal mixing. The value of K_1 found in this study at 800 °C is about factor of three higher than the value determined by Nowak and Behrens (2001) for the haplogranitic melt (Figure 3-25). On the other hand, extrapolation of the data obtained by Behrens and Yamashita (2008) for the sodium tetra- and hexasilicate supercooled melts at 200-320 °C gives much higher values of K_1 in these melts in comparison with the sodium disilicate melt at 800-900 °C.
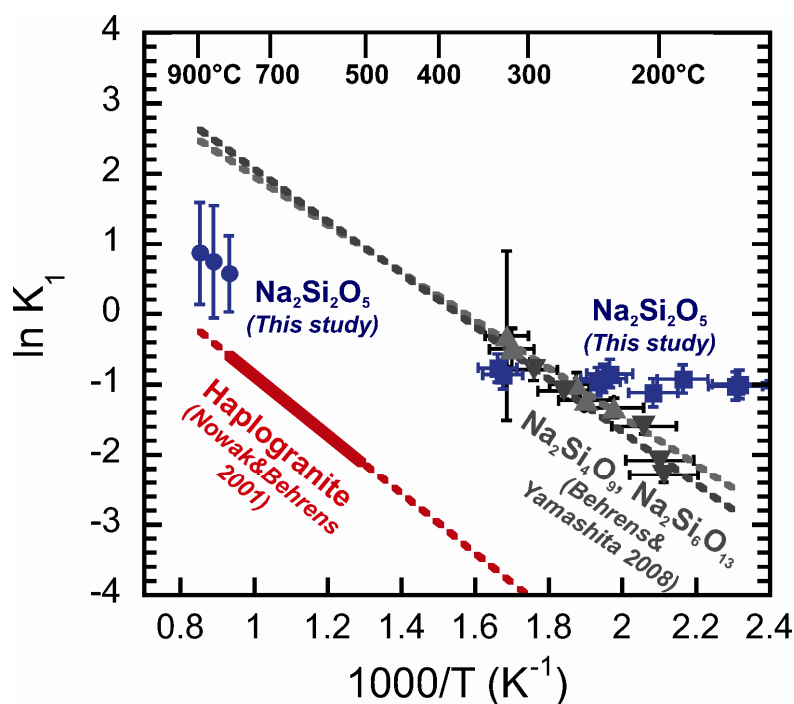
Figure 3-25. Temperature dependence of equilibrium constants K_1 for the water speciation reaction (1-1) based on *in situ* data for haplogranitic melt (solid red line, Nowak and Behrens, 2001), sodium tetra- and hexasilicate supercooled melts (grey triangles up and down, respectively, Behrens and Yamashita, 2008) and sodium disilicate melt (blue filled circles, this study). Dotted lines indicate extrapolation to lower and higher temperatures. Shown for comparison are the points at glass transition temperatures calculated based on NIR measurements of hydrous sodium disilicate glasses (blue squares, this study).

Determined in this study value of $\Delta H°$ (30.7±2.4 kJ mol^{-1}) falls within the narrow range of standard enthalpy change previously reported for the compositions from rhyolite and andesite to sodium hexasilicate and tetrasilicate ($\Delta H°$ = 25-35 kJ mol^{-1}, Behrens and Yamashita, 2008). Determined value of $\Delta S°$ (33.4±2.2 J mol^{-1} K^{-1}) is higher than the value reported for the haplogranitic melt (27.7 J mol^{-1} K^{-1}, Nowak and Behrens, 2001) and much lower than the ones obtained for the sodium tetra- and hexasilicate melts (44.8 and 48.2 J mol^{-1} K^{-1} respectively, calculated from equation (4) in Behrens and Yamashita, 2008).

In order to check whether the compositional dependence of K_1 among the sodium di-, tetra- and hexasilicate melts is ignorable at low temperatures near the glass transition, equilibrium constants K_1 at glass transition were estimated for the hydrous sodium disilicate glasses. Glass transition temperatures of the hydrous sodium disilicate glasses were calculated by the empirical model of Deubener et al. (2003) with the glass transition temperature of 509 °C for the anhydrous composition. Equilibrium constants K_1 at the glass transition temperatures were estimated based on the NIR measurements of water speciation in the glasses (Table 3-3, Calibration B). Calculated with this procedure points overlap with the low-temperature data of Behrens and Yamashita (2008) in the $1000/T$ – ln K_1 space (Figure 3-25), indicating a minor effect of composition on the equilibrium constant K_1 for the sodium di-, tetra- and hexasilicate supercooled melts.

Behrens and Yamashita (2008) have related higher values of K_1 in the sodium silicate melts than those reported for the rhyolite composition with the redistribution of hydrogen bond strengths. Results of the present study support this idea as they show that the difference in equilibrium constants K_1 between the rhyolitic and sodium disilicate melts becomes smaller at 800-900
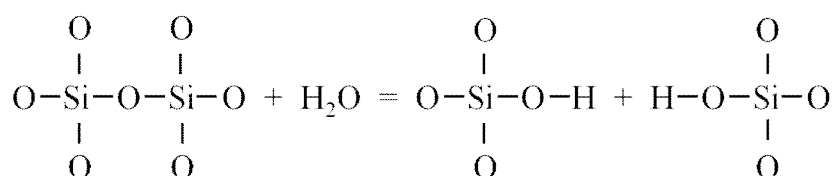
°C than at the temperatures near the glass transition (160-330 °C) (Figure 3-25). Several studies (e.g., Behrens and Schmidt, 1998; Mysen, 2010; Foustoukos and Mysen, 2015) have shown that the strength of hydrogen bonding in silicate melts and glasses decreases upon the increase of temperature. If the value of K_1 is influenced by the contribution from the hydrogen bonding, this contribution should become smaller at high temperatures, and we actually see it from the experimental data. This leads to the conclusion that hydrogen bonding can influence water speciation equilibrium in the depolymerized melts at temperatures near the glass transition, but its energetic contribution becomes less profound at 800-900 °C, resulting in more than ten times smaller difference of equilibrium constants K_1 between the polymerized aluminosilicate melts and depolymerized sodium disilicate melt than it would be expected from low-temperature data.

Experimental results of this study can be applied to explain the compositional dependence of solubility for the water component (water as a sum of the structurally bound OH groups and the H_2O molecules) in silicate and aluminosilicate melts. Water solubility was shown to increase with decreasing silica content and increasing alkali content of the silicate and aluminosilicate melts at the given fugacity of H_2O vapor (McMillan and Holloway, 1987; Carroll and Blank, 1997; Matteo et al., 2004; Schmidt and Behrens, 2008). Stolper (1982b) suggested that compositional dependence of water solubility can be related to the reaction equilibrium between water species in the melt (1-1) rather than to the vapor–melt equilibrium (1-2), but this idea has never been tested experimentally. In the light of the present study, compositional dependence of water solubility, indeed, can be explained by the enhanced formation of structurally bound OH groups in the silica-depleted, alkali-enriched depolymerized melts, since three times higher

equilibrium constant K_1 was obtained for the sodium disilicate melt than for the polymerized rhyolitic melt at 800-900 °C. The difference in equilibrium constants is preserved at pressures at least up to 1 GPa (this study; Sowerby and Keppler, 2000).

3.2.6. Viscosity of hydrous melts as a function of pressure

Viscosity of hydrous melts is directly related to the concentration of structurally bound OH groups through the water speciation reaction (1-1):

$$
\begin{array}{ccccccc}
\text{O} & & \text{O} & & \text{O} & & \text{O} \\
| & & | & & | & & | \\
\text{O}-\text{Si}-\text{O}-\text{Si}-\text{O} & + & \text{H}_2\text{O} & = & \text{O}-\text{Si}-\text{O}-\text{H} & + & \text{H}-\text{O}-\text{Si}-\text{O} \\
| & & | & & | & & | \\
\text{O} & & \text{O} & & \text{O} & & \text{O}
\end{array}
$$

Formation of the structurally bound OH groups requires a breakage of the bridging oxygens between silica tetrahedrons and thus results in the depolymerization of the melt and decrease of its viscosity.

It was shown by Schulze et al. (1996) that the viscosity of haplogranitic melt containing 5.9 wt.% total water does not depend on pressure in the range 0.3-1.0 GPa within the experimental error (Figure 3-26). These data are consistent with the pressure independence of the water speciation equilibrium, and hence, with the pressure-independent concentration of the structurally bound OH groups at a fixed concentration of total water in the well-polymerized melts (e.g., Nowak and Behrens, 2001; Sowerby and Keppler, 1999).
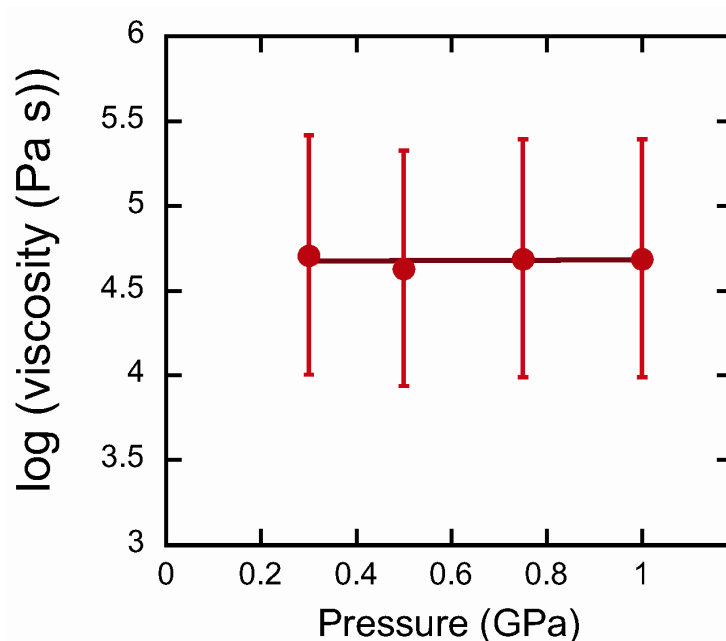
Figure 3-26. Pressure dependence of viscosity for the polymerized haplogranitic melt containing 5.9 wt.% total water at 900 °C (data points are from Schulze et al., 1996).

Measurement of viscosity for the hydrous depolymerized melts has experimental difficulties due to the lower viscosity of the melts and relatively fast subsidence of viscosity markers in the melt (e.g., in falling sphere method). Results of the present study allow to predict the rheological behavior of the hydrous sodium disilicate melts at high pressure. NIR measurements confirmed that the concentration of structurally bound OH groups does not depend on pressure in the range 0.2-1.7 GPa in this system at a fixed concentration of total water (Figure 3-21). At the same time, Raman measurements showed pressure independence of the concentration ratio Q^2 / Q^3, i.e. no detectable change in the connectivity of silica network structure in this pressure range (Figure 3-20). These observations lead to the conclusion that viscosity of the hydrous sodium disilicate melts containing from 1.3 to 8.1 wt.% total water will be independent of pressure up to 1.7 GPa when the total water content remains unchanged. With a pre-requisite of the

melt viscosity purely controlled by the degree of depolymerization, only one viscosity measurement at the easiest pressure condition will be enough for the estimation of melt viscosity over a range of pressure, and this is valid for the range of melt compositions from the fully polymerized rhyolitic to the highly depolymerized sodium disilicate.

Application of these results to the natural basaltic melts needs a special precaution about the presence of water species other than structurally bound OH groups and molecular H_2O. NMR study of water speciation in the alkaline earth silicate glasses by Xue and Kanzaki (2004) has revealed the presence of free hydroxyl water species, which are bonded to the metal cations, but not a part of the silicate network. Though formation of such free hydroxyl groups itself does not cause depolymerization of the melt and change of its viscosity, it can affect the concentration of structurally bound OH groups in the melt at high pressures. Future *in situ* measurements of water speciation in the alkaline earth silicate melts will help to solve this question and estimate the influence of free hydroxyl groups on the rheological properties of the natural depolymerized silicate melts.

CONCLUSIONS

- Though Stolper's model of ideal mixing between the H_2O molecules, oxygens of silicate melt framework and structurally bound OH groups (water speciation reaction) was originally proposed for the fully polymerized silicate melts, results of the present NIR study show that this model can be applied in the first approximation to the depolymerized sodium disilicate melts as well at total water contents below 8.1 wt.%, temperatures 800-900 °C and pressures 0.2-1.7 GPa.

- Water speciation equilibrium formulated in the present NIR study for the sodium disilicate melt in terms of ideal mixing was found to be independent of pressure below 1.7 GPa, in agreement with the previous studies on the more polymerized rhyolitic (Nowak and Behrens, 2001; Sowerby and Keppler, 1999) and aluminosilicate melts (Ochs and Lange, 1997; Richet and Polian, 1998). Pressure-independence of water speciation implies a negligible volume change for the water speciation reaction for a range of melt compositions.

- Raman spectroscopic measurements have not detected any change of Q^n speciation in the hydrous sodium disilicate melts with pressure, indicating a minor effect of pressure on the degree of melt polymerization, which is consistent with the present NIR study. Under the assumption that melt viscosity is purely controlled by the degree of melt polymerization, this observation denotes a pressure-independent viscosity of these melts at a fixed total water content in the pressure range 0.2-1.7 GPa.

- Temperature dependence of equilibrium constant K_1 for the reaction between molecular H_2O, oxygens of silicate melt framework and structurally bound OH groups in the sodium disilicate melt can be expressed as

$\ln K_1 = 4.02 - 3698 / T$ (K). The value of standard enthalpy change for this reaction determined in the present study ($\Delta H^\circ = 30.7 \pm 2.4$ kJ mol^{-1}) falls in the range of ΔH° previously reported for the more polymerized melts (25-35 kJ mol^{-1}). Observed variation of standard entropy change from $\Delta S^\circ = 45$-48 J mol^{-1} K^{-1} for the sodium tetra- and hexasilicate supercooled melts at 200-320 °C to $\Delta S^\circ = 33.4 \pm 2.2$ J mol^{-1} K^{-1} for the sodium disilicate melt at 800-900 °C can be related to the decreasing energetic contribution of the hydrogen bonding at high temperatures. Equilibrium constant K_1 obtained for the sodium disilicate melt at 800-900 °C is only factor of three higher than that reported for the rhyolitic melt by Nowak and Behrens (2001), though a factor of fifteen to nineteen higher K_1 value was expected at this temperature from the previous low-temperature measurements on sodium silicate supercooled melts.

ACKNOWLEDGMENTS

LIST OF TABLES

Table 1-1. Concentrations (in mole %, average values) and temperatures of low-pressure (1 atm) volcanic gases from the subduction zone-related, rift zone-related and ocean island-related volcanoes.

Table 1-2. Variations of water content in the groundmass glasses and melt inclusions from the different geological settings.

Table 2-1. Conditions of the first series of cross-calibration experiments in HDAC: measured temperature (T), observed pressure medium phase, frequency shifts of ^{13}C diamond and ruby ($\Delta v\_^{13}$C and Δv_ruby).

Table 2-2. Conditions of the second series of cross-calibration experiments in HDAC: temperature (T), frequency shifts of ^{13}C diamond and quartz ($\Delta v\_^{13}$C and Δv_Qtz).

Table 3-1. Compositions of the synthesized anhydrous glass (NS2) and of the soda-lime container glass (SRM621) measured by the same procedure as a reference.

Table 3-2. Parameters for the density determination of the six hydrous $Na_2Si_2O_5$ glasses synthesized in the IHPV.

Table 3-3. NIR data for the hydrous $Na_2Si_2O_5$ glass thin sections.

Table 3-4. Raman data for the hydrous $Na_2Si_2O_5$ glass thin sections.

Table 3-5. Result of *in situ* NIR measurements of hydrous $Na_2Si_2O_5$ melts at 900 °C, 850°C and 800 °C.

Table 3-6. Results of *in situ* Raman measurements and calculation of Q^2, Q^3 species abundances in the $Na_2Si_2O_5$ melts at 900 °C.

LIST OF FIGURES

Figure 1-1. Concentrations of water present as molecular H_2O species (filled symbols) and OH groups (open symbols) versus total water content of volcanic rhyolitic and synthetic albite glasses, measured by infrared spectroscopy at room temperature (data points are from Stolper, 1982b).

Figure 1-2. Viscosity of hydrous rhyolitic melt as a function of total water content, calculated at 800 °C using the model of Hess and Dingwell (1996).

Figure 1-3. Temperature dependence of equilibrium constants for the water speciation reaction (1-1) in melts and glasses (modified after Behrens and Yamashita, 2008).

Figure 1-4. Major components and setup of hydrothermal diamond anvil cell (HDAC): (a) general schematic (modified after Smith and Fang, 2009); (b) actual photograph.

Figure 2-1. A whole plan of the Kawai-type high-pressure apparatus (left) and a schematic cross-section of the split-sphere pressure vessel with the furnace assembly (right) (from Ito et al., 1984).

Figure 2-2. Schematic cross sections of the two types of cell assembly used for the synthesis of ^{13}C diamond in the multianvil apparatus. (**a**) MgO capsule contains two chambers filled with ^{13}C powder and a thermocouple junction between these chambers (run 5K1816). (**b**) MgO capsule with one sample chamber at the center and the thermocouple shifted towards the bottom (runs 5K1838, 5K1892).

Figure 2-3. X-ray diffraction profiles of the diamond aggregate synthesized in the runs 5K1838 (left) and 5K1892 (right).

Figure 2-4. FE-SEM images of the run product 5K1838.

Figure 2-5. H_2O phases observed during the first series of cross-calibration experiments in HDAC.

Figure 2-6. The shift of ^{13}C diamond Raman peak (left) and ruby fluorescence lines (right) with pressure and temperature (run #4).

Figure 2-7. The Experimental pressure–temperature paths plotted on the reference phase diagram of H_2O (melting curves from Wagner and Pruss 2002; ice VI–ice VII line from Johari et al. 1974).

Figure 2-8. Comparison between experimental pressure values calculated based on ^{13}C diamond pressure sensor and quartz (black dots), ruby (red dots) pressure references.

Figure 3-1. Photographs of clear transparent hydrous $Na_2Si_2O_5$ glass synthesized in the IHPV (4wt.% total water): (a) glass recovered intact from the Pt capsule after quenching, (b) doubly polished thin section under the optical microscope with transmission light.

Figure 3-2. Representative room temperature NIR spectra of the hydrous $Na_2Si_2O_5$ glass thin sections. The baseline-corrected spectra are shown on right hand side.

Figure 3-3. Examples of the NIR absorption spectra deconvolution for the thin sections containing 4.2 wt.% total water (a) and 8.0 wt.% total water (b).

Figure 3-4. (a) Room temperature Raman spectra of the $Na_2Si_2O_5$ glass thin sections containing different water contents. (b) Raman peaks deconvolution for the dry $Na_2Si_2O_5$ glass.

Figure 3-5. A photograph (a) and NIR spectrum (b) of the bubble-containing glass quenched from 900 °C and 0.3 GPa.

Figure 3-6. Determination of gasket thickness after experiment with the Mitutoyo displacement gauge.

Figure 3-7. Photomicrographs taken in the HDAC experiment with 4.2 wt.% total water (run #12).

Figure 3-8. Phases observed in the HDAC experiment with 6.2 wt.% total water (run #20).

Figure 3-9. Phases observed in the HDAC experiment with 8.1 wt.% total water (run #14).

Figure 3-10. Representative NIR absorption spectra of hydrous $Na_2Si_2O_5$ melts collected at 900 °C and four pressure intervals: (a) 0.2-0.5 GPa, (b) 0.8-0.9 GPa, (c) 1.1 and (d) 1.5-1.7 GPa.

Figure 3-11. NIR absorption spectra of hydrous $Na_2Si_2O_5$ melts collected at 850 °C and 800 °C.

Figure 3-12. Comparison of NIR absorption spectra between the starting glasses (left hand side) and the melts at 900 °C (right hand side) for the samples containing: (a) 4.2 wt.% total water, (b) 8.0 wt.% total water.

Figure 3-13. Correlation between the NIR peak heights of the sub-bands centered at about 5100 cm^{-1} and 5500 cm^{-1} to the sub-band centered at about 5200 cm^{-1}. (a) Starting glass thin sections at room temperature; (b) melts at 900 °C.

Figure 3-14. The change of 4500 cm^{-1} and 5200 cm^{-1} bands intensities with temperature for the run #27 with 8.1 wt.% total water.

Figure 3-15. Calibration plot for the determination of linear molar absorption coefficients for the 4500 cm^{-1} and 5200 cm^{-1} NIR bands of water species in the sodium disilicate melt at 900 °C and four pressure intervals.

Figure 3-16. Calibration plot for the determination of linear molar absorption coefficients at 850 °C and 800 °C.

Figure 3-17. Raman spectra of the $Na_2Si_2O_5$ melts collected at 900 °C and three pressure intervals: (a) 0-0.5 GPa, (b) 0.8-0.9 GPa and (c) 1.5-1.7 GPa.

Figure 3-18. Raman spectra of the dry $Na_2Si_2O_5$ starting glass placed inside HDAC. The spectrum on the right is shifted to the higher wavenumbers and shows a strong peak from the upper diamond anvil.

Figure 3-19. Deconvolution for the Raman spectra of room temperature glasses (left hand side) and of the melts at 900 °C (right hand side).

Figure 3-20. Concentrations of Q^2 and Q^3 species (in mol.%) in the $Na_2Si_2O_5$ melts at 900 °C as a function of pressure.

Figure 3-21. Pressure dependence of the equilibrium constant K_1 for the water speciation reaction at 900 °C.

Figure 3-22. Temperature dependence of the equilibrium constant K_1 for the water speciation reaction.

Figure 3-23. A plot for the determination of thermodynamic parameters (standard enthalpy $\Delta H°$ and entropy $\Delta S°$ change) for the water speciation equilibrium (1-1) in sodium disilicate melt.

Figure 3-24. Concentrations of water species (open symbols OH groups, filled symbols H_2O molecules) in $Na_2Si_2O_5$ melt at 900 °C and 0.2-0.5 GPa as a function of total water content.

Figure 3-25. Temperature dependence of equilibrium constants K_1 for the water speciation reaction (1-1) based on *in situ* data for haplogranitic melt (Nowak and Behrens, 2001), sodium tetra- and hexasilicate supercooled melts (Behrens and Yamashita, 2008) and sodium disilicate melt (this study).

Figure 3-26. Pressure dependence of viscosity for the polymerized haplogranitic melt containing 5.9 wt.% total water at 900 °C (data points are from Schulze et al., 1996).

REFERENCES

Bartholomew R.F., Butler B.L., Hoover H.L., Wu C.K. (1980) Infrared spectra of a water-containing glass. *Journal of American Ceramic Society*, 63, 481–485.

Bassett W.A. (2003) High pressure-temperature aqueous systems in the hydrothermal diamond anvil cell (HDAC). *European Journal of Mineralogy*, 15, 773–780.

Bassett W.A., Shen A.H., Bucknum M., Chou I.M. (1993) A new diamond cell for hydrothermal studies to 2.5 GPa and from –190 °C to 1200 °C. *Reviews of Scientific Instruments*, 64, 2340–2345.

Bassett W.A., Wu T.-C., Chou I.-M., Haselton T., Frantz J.D., Mysen B.O., Huang W.-L., Sharma S.K., Schiferl D. (1996) The hydrothermal diamond anvil cell (DAC) and its applications. Pp. 261–272 in: *Mineral Spectroscopy: A Tribute to Roger G. Burns* (M.D. Dyar, C. McCammon and M.W. Schaefer, editors). The Geochemical Society, Special Publication No. 5.

Behrens H., Nowak M. (2003) Quantification of H_2O speciation in silicate glasses and melts by IR spectroscopy – in situ versus quench techniques. *Phase Transitions: A Multinational Journal*, 76, 45–61.

Behrens H., Schmidt M.O. (1998) Infrared spectroscopy of hydrous silicic glasses at temperature up to 600 °C and implications for the incorporation and dynamics of water in glasses. *Neues Jahrbuch fur Mineralogie*, 172, 203–226.

Behrens H., Yamashita S. (2008) Water speciation in hydrous sodium tetrasilicate and hexasilicate melts: constraint from high temperature NIR spectroscopy. *Chemical Geology*, 256, 306–315.

Belviso S., Nguyen B.C., Allard P. (1986) Estimate of carbonyl sulfide (OCS) volcanic source strength deduced from OCS/CO_2 ratios in volcanic gases. *Geophysical Research Letters*, 13, 133–136.

Botcharnikov R.E., Behrens H., Holtz F. (2006) Solubility and speciation of C–O–H fluids in andesitic melt at T=1100–1300 °C and P=200 and 500 MPa. *Chemical Geology*, 229, 125–143.

Brawer S.A., White W.B. (1975) Raman spectroscopic investigation of the structure of silicate glasses. I. The binary silicate glasses. *Journal of Chemical Physics*, 63, 2421–2432.

Burnham C.W. (1975) Water and magmas: a mixing model. *Geochimica et Cosmochimica Acta*, 39, 1077–1084.

Carroll M.R., Blank J.G. (1997) The solubility of H_2O in phonolitic melts. *American Mineralogist*, 82, 549–556.

Chertkova N., Yamashita S., Ito E., Shimojuku A. (2014) High-pressure synthesis and application of a ^{13}C diamond pressure sensor for experiments in a hydrothermal diamond anvil cell. *Mineralogical Magazine*, 78, 1677–1685.

Cody G.D., Mysen B.O., Lee S.K. (2005) Structure vs. composition: A solid-state ^{1}H and ^{29}Si NMR study of quenched glasses along the Na_2O-SiO_2-H_2O join. *Geochimica et Cosmochimica Acta*, 69, 2373–2384.

Datchi F., Canny B. (2004) Raman spectrum of cubic boron nitride at high pressure and temperature. *Physical Review*, 69, 144106.

Datchi F., Dewaele A., Loubeyre P., Letoullec R., Godec Y. Le, Canny B. (2007) Optical pressure sensors for high-pressure-high-temperature studies in a diamond anvil cell. *High Pressure Research*, 27, 447–463.

Deubener J., Muller R., Behrens H., Heide G. (2003) Water and the glass transition temperature of silicate melts. *Journal of Non-Crystalline Solids*, 330**,** 268–273.

Dingwell D.B., Webb S. (1990) Relaxation in silicate melts. *European Journal of Mineralogy*, 2, 427–449.

Dixon J.E., Clague D.A. (2001) Volatiles in basaltic glasses from Loihi seamount, Hawaii: evidence for a relatively dry plume component. *Journal of Petrology*, 42, 627–654.

Dixon J.E., Clague D.A., Stolper E.M. (1991) Degassing history of water, sulfur, and carbon in submarine lavas from Kilauea volcano, Hawaii. *Journal of Geology*, 99, 371–394.

Dixon J.E., Stolper E., Delaney J.R. (1988) Infrared spectroscopic measurements of CO_2 and H_2O in Juan de Fuca Ridge basaltic glasses. *Earth and Planetary Science Letters*, 90, 87–104.

Ernsberger F.M., 1977. Molecular water in glass. *Journal of American Ceramic Society*, 60, 91–92.

Fukumi K., Hayakawa J., Komiyama T. (1990) Intensity of Raman band in silicate glasses. *Journal of Non-Crystalline Solids*, 119**,** 297–302.

Furukawa T., Fox K.E., White W.B. (1981) Raman spectroscopic investigation of the structure of silicate glasses. III. Raman intensities and structural units in sodium silicate glasses. *Journal of Chemical Physics,*153**,** 3226–3237.

Foustoukos D., Mysen B.O. (2015) The structure of water-saturated carbonate melts. *American Mineralogist,* 100, 1–340.

Garcia M.O., Liu N.W.K., Muenow D.W. (1979) Volatiles in submarine volcanic rocks from the Mariana Island arc and trough. *Geochimica et Cosmochimica Acta*, 43, 305–312.

Gerlach T.M. (1979) Evaluation and restoration of the 1970 volcanic gas analyses from Mount Etna, Sicily. *Journal of Volcanology and Geothermal Research*, 6, 165–178.

Gerlach T.M. (1980) Evaluation of volcanic gas analyses from Surtsey Volcano, Iceland, 1964-1967. *Journal of Volcanology and Geothermal Research*, 8, 191–198.

Gerlach T.M. (1993) Oxygen buffering of Kilauea volcanic gases and the oxygen fugacity of Kilauea basalt. *Geochimica et Cosmochimica Acta*, 57, 795–814.

Gerlach T.M., Casadevall T.J. (1986) Evaluation of gas data from high-temperature fumaroles at Mount St. Helens, 1980-1982. *Journal of Volcanology and Geothermal Research*, 28, 107–140.

Giggenbach W.F., LeGuern F. (1976) The chemistry of magmatic gases from Erta' Ale, Ethiopia. *Geochimica et Cosmochimica Acta*, 40, 25–30.

Giggenbach W.F., Martini M., Corazza E. (1986) The effects of hydrothermal processes on the chemistry of some recent volcanic gas discharges. *Periodico di Mineralogia*, 55, 15–28.

Halmer M.M., Schmincke H.-U., Graf H.-F. (2002) The annual volcanic gas input into the atmosphere, in particular into the stratosphere: a global data set for the past 100 years. *Journal of Volcanology and Geothermal Research*, 115, 511–528.

Hauri E. (2002) SIMS analysis of volatiles in silicate glasses, 2: isotopes andabundances in Hawaiian melt inclusions. *Chemical Geology*, 183, 115–141.

Hauri E.H., Gaetani G.A., Green T.H. (2006) Partitioning of water during melting of the Earth's upper mantle at H_2O-undersaturated conditions. *Earth and Planetary Science Letters*, 248, 715–734.

Hess K-U., Dingwell D.B. (1996) Viscosities of hydrous leucogranitic melts: A non-Arrhenian model. *American Mineralogist*, 81, 1297–1300.

Hess N.J., Exarhos G.J. (1989) Temperature and pressure dependence of laser induced fluorescence in Sm:YAG—a new pressure calibrant. *High Pressure Research*, 2, 57–64.

Holtz F., Johannes W., Tamic N., Behrens H. (2001) Maximum and minimum water contents of granitic melts generated in the crust: a reevaluation and implications. *Lithos*, 56, 1–14.

Ihinger P.D., Zhang Y., Stolper E.M. (1999) The speciation of dissolved water in rhyolitic melt. *Geochimica et Cosmochimica Acta*, 63, 3567–3578.

Ito E., Yamada H. (1982) Stability relations of silicate spinels, ilmenites and perovskites. Pp. 405–419 in: *High-Pressure Research in Geophysics* (S. Akimoto and M.H. Manghnani, editors). D Reidel, Dordrecht.

Ito E., Takahashi E., Matsui Y. (1984) The mineralogy and chemistry of the lower mantle: an implication of the ultrahigh-pressure phase relations in the system MgO-FeO-SiO_2. *Earth and Planetary Science Letters*, 67, 238–248.

Irifune T., Kurio A., Sakamoto S., Inoue T., Sumiya, H. (2003) Materials: ultrahard polycrystalline diamond from graphite. *Nature*, 421, 599–600.

Irifune T., Kurio A., Sakamoto S., Inoue T., Sumiya H., Funakoshi K. (2004) Formation of pure polycrystalline diamond by direct conversion of graphite at high pressure and high temperature. *Physics of Earth and Planetary Interiors*, 143, 593–600.

Johari G.P., Lavergne A., Whalley E. (1974) Dielectric properties of ice VII and VIII and the phase boundary between ice VI and VII. *Journal of Chemical Physics*, 61, 4292–4300.

Kelley K.A., Plank T., Newman S., Stolper E.M., Grove T.L., Parman S., Hauri E.H. (2010) Mantle melting as a function of water content beneath the Mariana arc. *Journal of Petrology*, 0, 1–28.

Lacam A., Chateau C. (1989) High-pressure measurements at moderate temperatures in a diamond anvil cell with a new optical sensor: $SrB_4O_7:Sm^{2+}$. *Journal of Applied Physics*, 66, 366–372.

LeGuern F., Gerlach T.M., Nohl A. (1982) Field gas chromatograph analyses of gases from a glowing dome at Merapi volcano, Java, Indonesia, 1977, 1978, 1979. *Journal of Volcanology and Geothermal Research*, 14, 223–245.

Levin E.M., Robbins C.R., McMurdie H.F. (1964) In: Phase diagrams for ceramists, Margie K. Reser, eds., p 181. The American Ceramic Society, Columbus, Ohio, U.S.A.

Liu Y., Behrens H., Zhang Y. (2004) The speciation of dissolved H_2O in dacitic melt. *American Mineralogist*, 89, 277–284.

Long D.A. (1977) Raman Spectroscopy. McGraw-Hill.

Malfait W.J., Zakaznova-Herzog V.P., Halter W.E. (2008) Quantitative Raman spectroscopy: speciation of Na-silicate glasses and melts. *American Mineralogist*, 93, 1505–1518.

Matteo V.D., Carrol M.R., Behrens H., Vetere F., Brooker R.A. (2004) Water solubility in trachytic melts. *Chemical Geology*, 213, 187–196.

McMillan P. F. and Holloway J. R. (1987) Water solubility in aluminosilicate melts. *Contributions to Mineralogy and Petrology*, 97**,** 320–332.

McMillan P.F., Wolf G.H., Poe B.T. (1992) Vibrational spectroscopy of silicate liquids and glasses. *Chemical Geology*, 96, 351–366.

Mysen B.O. (2010) Speciation and mixing behavior of silica-saturated aqueous fluid at high temperature and pressure. *American Mineralogist,* 95, 1807–1816.

Mysen B.O., Cody G.D. (2005) Solution mechanisms of H_2O in depolymerized peralkaline melts. *Geochimica et Cosmochimica Acta*, 69, 5557–5566.

Mysen B.O., Frantz J.D. (1993) Structure and properties of alkali silicate melts at magmatic temperatures. *European Journal of Mineralogy*, 5, 393–407.

Mysen B.O., Richet P. (2005) Silicate glasses and melts: Properties and structure. Elsevier B.V., Amsterdam.

Mysen B.O., Yamashita S. (2010) Speciation of reduced C–O–H volatiles in coexisting fluids and silicate melts determined in-situ to ~1.4 GPa and 800 °C. *Geochimica et Cosmochimica Acta*, 74, 4577–4588.

Namba Y., Heidarpour E., Nakayama M. (1992) Size effects appearing in the Raman spectra of polycrystalline diamonds. *Journal of Applied Physics*, 72, 1748–1751.

Neuville D.R., Ligny D., Henderson G.S. (2014) Advances in Raman spectroscopy applied to Earth and Material sciences. In: Spectroscopic methods in Mineralogy and Materials sciences, G.S. Henderson, D.R. Neuville and R.T. Downs, eds., *Reviews in Mineralogy and Geochemistry*, 78, pp 509–541, Mineralogical Society of America, Washington, D.C.

Newman S., Stolper E. (2000) H_2O and CO_2 in magmas from the Mariana arc and back arc systems. *Geochemistry Geophysics Geosystems*, 1, 1–24.

Newman S., Stolper E.M., Epstein S. (1986) Measurement of water in rhyolitic glasses: calibration of an infrared spectroscopic technique. *American Mineralogist,* 71, 1527–1541.

Ni H., Keppler H., Behrens H. (2011) Electrical conductivity of hydrous basaltic melts: implications for partial melting in the upper mantle. *Contributions to Mineralogy and Petrology*, 162, 637–650.

Nowak M., Behrens H. (1995) The speciation of water in haplogranitic glasses and melts determined by in situ near-infrared spectroscopy. *Geochimica et Cosmochimica Acta*, 59, 3445–3450.

Nowak M., Behrens H. (2001) Water in rhyolitic magmas: getting a grip on a slippery problem. *Earth and Planetary Science Letters*, 184, 515–522.

Ochs F.A., Lange R.A. (1997) The partial molar volume, thermal expansivity, and compressibility of H_2O in $NaAlSi_3O_8$ liquid: new measurements and an internally consistent model. *Contributions to Mineralogy and Petrology*, 129, 155–165.

Ochs F.A., Lange R.A. (1999) The density of hydrous magmatic liquids. *Science*, 283, 1314–1317.

Ohfuji H., Okimoto S., Kunimoto T., Isobe F., Sumiya H., Komatsu K., Irifune T. (2012) Influence of graphite crystallinity on the microtexture of nano-polycrystalline diamond by direct conversion. *Physics and Chemistry of Minerals*, 39, 543–552.

Ohlhorst S., Behrens H., Holtz F., Schmidt B.C. (2000) Water speciation in aluminosilicate glasses and melts. Pp. 193–196 in: *Applied Mineralogy in Research, Economy, Technology and Culture* (D. Rammlmair, J. Mederer, T.H. Oberthür, R.B. Heimannund and H. Pentinghaus, editors). Proc. 6th Int. Conf. Appl. Mineral., vol. 1. Balkema, Rotterdam.

Persikov E.S. (1991) The viscosity of magmatic liquids: experiment, generalized patterns; a model for calculation and prediction; application. *Advances in Physical Geochemistry*, 9, 1–40.

Piermarini G.J., Block S., Barnett J.D. (1973) Hydrostatic limits in liquids and solids to 100 kbar. *Journal of Applied Physics*, 44, 5377–5382.

Qiu W., Velisavljevic N., Baker P.A., Vohra Y.K. (2004) Isotopically pure ^{13}C layer as a stress sensor in a diamond anvil cell. *Applied Physics Letters*, 84, 5308–5310.

Ragan D.D., Gustavsen R., Schiferl D. (1992) Calibration of the ruby R_1 and R_2 fluorescence shifts as a function of temperature from 0 to 600 K. *Journal of Applied Physics*, 72, 5539–5544.

Richet P., Bottinga Y. (1995) Rheology and configurational entropy of silicate melts. In: Structure, Dynamics and Properties of Silicate Melts, J.F. Stebbins, P.F. McMillan and D.B. Dingwell, eds., *Reviews in Mineralogy and Geochemistry*, 32, pp 67–93, Mineralogical Society of America, Washington, D.C.

Richet P., Polian A. (1998) Water as a dense icelike component in silicate glasses. *Science*, 281, 396–398.

Schiferl D., Nicol M., Zaug J.M., Sharma S.K., Cooney T.F., Wang S.-Y., Anthony T.P., Fleischer J.F. (1997) The diamond ^{13}C/^{12}C isotope Raman pressure sensor system for high-temperature/pressure diamond-anvil cells with reactive samples. *Journal of Applied Physics*, 82, 3256–3265.

Schmidt B.C., Behrens H. (2008) Water solubility in phonolite melts: influence of melt composition and temperature. *Chemical Geology*, 256, 259–268.

Schmidt Ch., Ziemann M.A. (2000) In-situ Raman spectroscopy of quartz: a pressure sensor for hydrothermal diamond-anvil cell experiments at elevated temperatures. *American Mineralogist*, 85, 1725–1734.

Schulze F., Behrens H., Holtz F., Roux J., Johannes W. (1996) The influence of H_2O on the viscosity of a haplogranitic melt. *American Mineralogist*, 81, 1155–1165.

Shen A., Keppler H. (1995) Infrared spectroscopy of hydrous silicate melts to 1000 °C and 10 kbar: Direct observation of H_2O speciation in a diamond anvil cell. *American Mineralogist*, 80, 1335–1338.

Silver L.A., Stolper E. (1985) A thermodynamic model for hydrous silicate melts. *Journal of Geology*, 93, 161–178.

Smith R.L. and Fang Z. (2009) Techniques, applications and future prospects of diamond anvil cells for studying supercritical water systems. *Journal of Supercritical Fluids*, 47, 431–446.

Sobolev A.V., Chaussidon M. (1996) H_2O concentrations in primary melts from supra-subduction zones and mid-ocean ridges: implications for H_2O storage and recycling in the mantle. *Earth and Planetary Science Letters*, 137, 45–55.

Sowerby J.R., Keppler H. (1999) Water speciation in rhyolitic melt determined by in-situ infrared spectroscopy. *American Mineralogist*, 84, 1843–1849.

Sowerby J.R., Keppler H. (2000) Errata for: Water speciation in rhyolitic melt determined by in-situ infrared spectroscopy. *American Mineralogist*, 84, 1843–1849.

Stolper E. (1982a) Water in silicate glasses: an infrared spectroscopic study. *Contributions to Mineralogy and Petrology*, 81, 1–17.

Stolper E. (1982b) The speciation of water in silicate melts. *Geochimica et Cosmochimica Acta*, 46, 2609–2620.

Stuke A., Behrens H., Schmidt B.C., Dupree R. (2006) H_2O speciation in foat glass and soda lime silica glass. *Chemical Geology*, 229, 64–77.

Symonds R.B., Rose W.I., Bluth G.J. and Gerlach T.M. (1994) Volcanic-gas studies: methods, results, and applications. In: Volatiles in Magmas, M.R. Carroll and J.R. Holloway, eds., *Reviews in Mineralogy and Geochemistry,* 30, pp 1–66, Mineralogical Society of America, Washington, D.C.

Taran Y.A., Rozhkov A.M., Serafimova E.K., Esikov A.D. (1991) Chemical and isotopic composition of magmatic gases from the 1988 eruption of Klyuchevskoy volcano, Kamchatka. *Journal of Volcanology and Geothermal Research*, 46, 255–263.

Wagner W., Pruss A. (2002) The IAPWS formulation 1995 for the thermodynamic properties of ordinary water substance for general scientific use. *Journal of Physical and Chemical Reference Data*, 31, 387–535.

Wallace P.J. (2005) Volatiles in subduction zone magmas: concentrations and fluxes based on melt inclusion and volcanic gas data. *Journal of Volcanology and Geothermal Research*, 140, 217–240.

Wallace P.J., Anderson A.T., Davis A.M. (1995) Quantification of pre-eruptive exsolved gas contents in silicic magmas. Nature, 377, 612–616.

Wu C.K. (1980) Nature of incorporated water in hydrated silicate glasses. *Journal of American Ceramic Society*, 63, 453–457.

Xue X., Kanzaki M. (2004) Dissolution mechanisms of water in depolymerized silicate melts: constraints from ^1H and ^{29}Si NMR

spectroscopy and ab initio calculations. *Geochimica et Cosmochimica Acta*, 68, 5027–5057.

Yamashita S. (1999) Experimental study of the effect of temperature on water solubility in natural rhyolite melt to 100 MPa. *Journal of Petrology*, 40, 1497–1507.

Yamashita S., Behrens H., Schmidt B.C., Dupree R. (2008) Water speciation in sodium silicate glasses based on NIR and NMR spectroscopy. *Chemical Geology*, 256, 231–241.

Zha C.S., Mao H.K., Hemley R.J. (2000) Elasticity of MgO and a primary pressure scale to 55 GPa. *PNAS*, 97, 13494–13499.

Zotov N., Keppler H. (1998) The influence of water on the structure of hydrous sodium tetrasilicate glasses. *American Mineralogist*, 83, 823–834.